Design, fabrication and characterisation of III-V nanowire random lasers

Mohammad Rashidi Shahgoli

Australian National University

A thesis submitted for the degree of Doctor of Philosophy of
The Australian National University

Declaration

This thesis contains no material which has been accepted for the award of any other degree or diploma in any university. To the best of the author's knowledge, it contains no material previously published or written by another person, except where due reference is made in the text.

Mohammad Rashidi Shahgoli

October 2021

Acknowledgements

This thesis would not have been possible without the contribution of many people and the continuous support of my family members and supervisors.

I thank my principal supervisor, Prof. Hoe Tan, for always providing me with timely and constructive feedback and guidance on the direction of my research. I appreciate his readiness to help and sharing of input throughout my PhD. I express my sincere gratitude to Prof. Chennupati Jagadish for allowing me to pursue this PhD in his group. Prof. Jagadish and Prof Hoe Tan are inspiring scientists and admirable people, and I am honoured to have done my PhD under their supervision. I would like to also thank Dr Sudha Mokkapati for defining this interesting project prior to her leaving the group.

I also wish to thank my colleagues Dr Tuomas Haggren for providing the VLS grown NWs, and Dr Zhicheng Su and Dr Zyuian Li for training me to do the optical characterization measurements. I also wish to extend my gratitude to the Australian National Fabrication Facility, and staff of ACT Node, Drs. Kaushal Vora, Li Li, Mark Lockrey, Olivier Lem, and Mykhaylo Lysevych for training me in different tools and their technical support.

I also warmly acknowledge numerous support extended by my friends and all group members at different points of my academic life at ANU, but also remained very good friends.

I also acknowledge the Australian Research Council (ARC) for its financial support. This project was funded by ARC as a discovery project (DP170102530).

Last but not least, I wish to respectfully acknowledge the support of my family, who provided me encouragement and care, enabling me to pursue my PhD with peace of mind and without feeling stress. I am very grateful to my father, my mother and my brother.

Abstract

Disorder is generally considered an undesired element in lasing action. However, disorder plays a significant and critical role in random lasers (RLs), whose feedback mechanism is based on random scattering events. Even though some unique properties in RLs such as large-angle emission, lasing from different surfaces, large area manufacturability, and wavelength tunability can be advantageous in specific applications, the applicability of RLs has been limited due to the chaotic fluctuations and instability of the lasing modes. The instability issue of RLs has resulted in fluctuating sources whose properties could not be controlled. Therefore, even though RLs, unlike other lasers based on traditional Fabry-Pérot cavities, are much simpler and cost-effective sources to fabricate, because of the chaotic fluctuations and instability of the lasing modes, controlling their lasing properties is challenging.

In this dissertation, using random arrays of III-V nanowires as the disordered medium, it is shown that mode localisation could reduce the spatial overlap between the various lasing modes, thus preventing mode competition and improving stability, leading to laser sources with high-quality factors and very low thresholds. We present the experimental evidence of strong light localisation in multi-mode random nanowire lasers, which are temporally stable, leading to controllable emission. We further demonstrate that by changing the design parameters of the nanowire array, such as filling factor, dimensions of the nanowires, degree of randomness, and array size, the properties of the lasing modes, including the number of modes, lasing wavelengths, and lasing threshold can be controlled.

To localise and decouple the lasing modes, the disorder in the medium should support modes that have a resonant type of feedback where there is a chance for the scattered light to create cavities or closed loops. If the scattering efficiency is not strong enough, the modes are coupled which are not conducive to supporting closed-loop paths. In these types of RLs, the feedback mechanism becomes non-resonant (non-coherent) without creating any cavities. In other words, light just gets amplified, and the emission becomes amplified spontaneous emission without any coherency. We show that by aligning the nanowires, the modes' scattering efficiency and quality factor can be increased, thereby favouring the resonant feedback lasing. Besides, practical methods for managing the type of feedback mechanism are also shown and discussed. Switching between resonant and non-resonant lasing modes opens up new opportunities to use these lasers in many applications.

In this thesis, different issues of RLs such as lasing mode instability, challenges of controlling the RLs emission properties and feedback mechanisms were investigated and addressed. The

practical methods introduced to solve these challenges could open up the realisation of broadband nanoscale lasers for the next-generation photonic devices, with all the advantages offered by RLs.

Publications

Journal Articles

- M. Rashidi, H. H. Tan, and S. Mokkapati, "Stable, multi-mode lasing in the strong localization regime from InP random nanowire arrays at low temperature," Optica, vol. 8, no. 9, pp. 1160-1166, 2021/09/20 2021.

- M. Rashidi, Z. Li, C. Jagadish, S. Mokkapati, and H. H. Tan, "Controlling the lasing modes in random lasers operating in the Anderson localization regime," Optics Express, vol. 29, no. 21, pp. 33548-33557, 2021/10/11 2021.

- M. Rashidi, T. Haggren, Z. Su, C. Jagadish, S. Mokkapati, and H. H. Tan, "Managing Resonant and Nonresonant Lasing Modes in GaAs Nanowire Random Lasers," Nano Letters, vol. 21, no. 9, pp. 3901-3907, 2021/05/12 2021.

Conference Papers and Proceedings

- M. Rashidi, T. Haggren, Z. Su, C. Jagadish, S. Mokkapati, and H. H. Tan. Controlling the type of lasing modes in disordered media based on GaAs-AlGaAs nanowires. IEEE Photonics Conference (IPC), 2021.

- M. Rashidi, H. H. Tan, and S. Mokkapati, “Anderson localization of light in InP nanowires for stable, multimode lasing,” 27th International Semiconductor Laser Conference – ISLC20201

List of Abbreviations

a.u.	arbitrary units
AlGaAs	aluminium gallium arsenide
ASE	amplified spontaneous emission
CCD	charge-coupled device
FDTD	Finite-difference time-domain
F-P	Fabry-Pérot
GaAs	gallium arsenide
InP	indium phosphide
L-L	light in - light out
MOVPE	metal-organic vapour phase epitaxy
NA	numerical aperture
NW	nanowire
PL	photoluminescence
PML	perfectly matched layer
RL	random laser
SAE	selective-area epitaxy
SA-MOVPE	selective-area metal-organic vapour phase epitaxy
SEM	scanning electron microscopy
Si	silicon
SiO_2	silicon dioxide
STEM	scanning transmission electron microscopy
TCSPC	time-correlated single-photon counting
TEM	transmission electron microscopy
TRPL	time-resolved photoluminescence
UV	ultraviolet
VLS	vapour-liquid-solid
WGM	whispering gallery mode

Table of Contents

List of Tables

List of Figures

Chapter 1: Introduction and background

1.1 Motivation

Light Amplification by Stimulated Emission of Radiation (Lasers) are devices that produce light with properties very different than those of other light sources, e.g., incandescent bulbs or light-emitting diodes (LEDs). For example, laser light can travel large distances as a narrow beam without diverging (collimation property), and the light can also be focused to a very tight spot. Besides, in lasers, the electric fields at different locations across the beam profile have a strong correlation, and fixed phase relationship (spatial coherency property), and also these phase relationships are maintained over a long enough time (temporal coherency property). Finally, laser light can have a very narrow spectrum of singular colour (monochromatic property) emission.

Due to these unique characteristics, laser technology has found important uses in industry (cutting and welding materials, semiconducting chip manufacturing, etc.), information technology (optical communication over optical fibres or free-space), data storage (optical disk drives), medicine (DNA sequencing instruments, surgery, hair removal products, and skin treatments), defence (laser guidance, defensive countermeasures, etc.) and security (law enforcement devices), and have become an integral part of modern life.

Usually, lasers have three basic components [1, 2]: (I) lasing material or gain/active medium, (II) external energy source, and (III) optical resonator. The active medium is excited by the external energy source (pump source) in lasers to produce the population inversion. In the gain medium, spontaneous and stimulated emission of photons takes place. If the photon mainly generated by the stimulated emission balances the loss mechanisms, the system could have optical gain leading to light amplification. The optical resonator (or laser cavity), allows the laser radiation to circulate and pass the gain medium which compensates for the optical losses and builds up the light intensity in the beam. Besides, the resonator fulfils two functions: it restricts the direction of propagation and also selects the emission wavelength.

In lasers with conventional cavities such as Fabry–Pérot, the cavity consists of two mirrors separated by a distance, L. One mirror can be fully reflective, and the other partially reflective. Both the mirrors are set up on the optic axis, parallel to each other. The active medium is used in the optical cavity between these mirrors. This arrangement only filters those photons that came along the axis and are reflected by the mirrors back into the medium, where it may be

amplified by stimulated emission. In these systems, designing and fabricating proper mirrors, especially for some range of wavelengths and smaller dimensions, is challenging. Unlike these traditional lasers with cavities supporting Fabry-Pérot (FP) modes that need a precise fabrication, random lasers' cavities do not require mirrors.

A random laser (RL) is a non-conventional laser whose feedback mechanism relies on multiple scattering induced by random scatterers rather than defined optical cavities [3]. Unlike conventional lasers with well-defined cavities, these lasers could be formed in much simpler structures/platforms, thus reducing cost and fabrication complexity. Furthermore, RLs' very broad angular emission and large-area manufacturability properties can be used efficiently for display applications [4, 5]. Additionally, due to their low spatial coherence and bright illumination, RLs can be utilised for speckle-free laser imaging [6] and laser sources formed on flexible substrates [7, 8].

Due to the simple structure and unique properties of RLs, they have become an exciting research field. However, their practical application is hindered because of the following problems. First, because of the chaotic fluctuations and instability of the lasing modes, the emission spectrum changes rapidly and is not stable in both intensity and emission wavelength. Secondly, because of this instability, controlling and engineering the emission spectra are challenging. This has impeded the application of these sources where tunable sources or sources emitting at particular wavelengths are required. Finally, as the disordered media cannot provide an optical cavity (in RLs with non-resonant feedback), the emitted light is practically Amplified Spontaneous Emission and non-coherent. Because of these issues, the practical applications of RLs are somewhat limited.

In this thesis, the issues related to mode instability, non-tunability, and incoherent nature of the beam are investigated for a RL system made of InP nanowires. After a short review of the development of the RLs and theoretical background (this chapter) as well as the numerical and experimental techniques (second chapter) used in this thesis, Chapter 3 presents the design, modelling, and experimental results of InP random nanowire arrays to generate highly localised modes which have stable multi-mode lasing. In Chapter 4, the tunability and further control of the laser properties of these random nanowire lasers are investigated. In Chapter 5 methods for switching between resonant and non-resonant lasing modes in GaAs-AlGaAs, random nanowire arrays are presented and discussed. Finally, a summary of the key findings from this dissertation is presented in Chapter 6, together with some suggestions for future work.

1.2 History and background of random lasers

As opposed to the reflective feedback by the mirrors of a conventional laser, the feedback mechanism of a RL is based on multiple random scattering resulting from fluctuation of the dielectric constant in disordered materials [3, 9]. This alternative feedback mechanism has important application to lasers where an efficient reflective element is not readily available, e.g., in UV and x-ray lasers. This unconventional feedback mechanism in RLs leads to properties interesting from both fundamental aspects and practical applications, such as imaging [6], sensing [10], and medical diagnostics [11]. For example, RLs represent a new class of light sources with high photon degeneracy/spectral radiance and low spatial coherence, which make these sources ideal for full-field imaging purposes [6]. Besides, because of shape flexibility and substrate compatibility, low cost, and small size, RLs could be used in machine vision to verify manufactured parts, document encoding and material labelling, high-speed multicolour displays, photodynamic therapy, tumour detection, and photonic integrated circuits [12].

The story of RLs started with a group led by laser pioneer and Nobel laureate N. G. Basov in 1966 [13]. The first RL was introduced just by replacing one mirror of the FP cavity with a scattering surface. The feedback of this laser was used simply to return part of the energy, or photons, to the gain medium. Unlike conventional FP cavities in which light returns to its origin and the type of feedback is the field or amplitude feedback, here, there are no standing waves, and the feedback type is energy or intensity feedback. Thus, the feedback is phase insensitive (i.e. incoherent) and frequency independent (i.e. non-resonant). In 1968, Letokhov took one step further and proposed self-generation of light in an active medium filled with scatterers [14]. He solved the diffusion equation for the photon energy density $W(r, t)$ in the presence of a uniform and linear gain for the diffusive regime where the photon transport mean free path, l_t, is much smaller than the dimension of scattering medium, L, but much longer than the optical wavelength, λ ($L > l_t > \lambda$). He found out that if the generation length, L_{gen}, is smaller than the mean path length L_{pat} ($L_{pat} > L_{gen}$), on average, every photon will generate another photon before escaping the scattering medium. This triggers a 'chain reaction' leading to the photon number increasing with time. Nearly 20 years after Letokhov's pioneering work in this area, intense stimulated radiation was observed in $Na_5La_{1-x}Nd_x(MoO_4)_4$ powder under resonant pumping at low temperature (77 K) [15]. They observed when the pumping intensity exceeded a threshold, the Nd^{3+} emission spectrum was narrowed to a single line, and the emission pulse duration was shortened by approximately four orders of magnitude. They observed similar phenomena in a wide variety of other laser crystal powders [16]. To explain this phenomenon, three reasons were proposed. First, diffusion of light was the explanation behind the intense

stimulated emission. In other words, the photons spontaneously emitted by neodymium or titanium ions are multiply scattered and bounced by particles before leaving the scattering medium. So, the chance of hitting the doped ions has increased, leading to stimulated emission [17]. The other explanation was attributed to the total internal reflection of the light inside the particle. That is to say, since the particles were much bigger than the light wavelength, the particles were acting as coupled microcavities supporting lasing modes [18]. Finally, because stimulated emission was weak at low doping levels of active ions, the burst of intense radiation was said to result from synchronized spontaneous emission, namely superradiance and superfluorescence [19, 20].

To clarify the case, in 1994, Lawandy et al. separated the scattering (titanium dioxide microparticles) and gain media (Rhodamine 640 perchlorate dye) in a liquid (methanol) solution [21]. Besides, the particles had a mean diameter of 250 nm, which was much smaller than the wavelength of the light and too small to trap the light. Interestingly, they observed the same emission spectrum narrowing above the pumping threshold. Besides, the system showed a lasing behaviour with non-resonant feedback, and the emission spectrum was highest at the peak of the gain spectrum. So, the origin of lasing was attributed to light diffusion. The discovery of Lawandy et al. has triggered many experimental [22-24] and theoretical [25-27] studies of RLs with non-resonant feedback.

In 1998, Cao et al. introduced another type of RL in disordered semiconductor powders and polycrystalline films with resonant and coherent feedback [28]. In this work, ZnO nanoparticles with an average diameter of 100 nm were deposited onto an ITO-coated substrate. A coherent backscattering experiment was conducted, and l_t was obtained around the probe beam wavelength (λ=410 nm), indicating the system is a very strong scattering medium. Due to this strong scattering, recurrent light scattering events arose, i.e., after multiple scattering, the light was returned to the starting point where the scattering was started. So, constructive interference can happen in those frequencies, and the system can show lasing behaviour at certain frequencies. Unlike the non-resonant, or incoherent, feedback RLs, these lasers showed very narrow discrete spectral peaks (the linewidth of these peaks was less than 2 Å) at particular frequencies. The frequencies of these peaks were depended on the position of the sample. In other words, by changing the illuminated light spot, the resonant frequencies could be changed, indicating the feedback is “field” or “amplitude” type and not “intensity” or “energy” type. It has been seen that by increasing the density of scattered particles in an amplifying medium, the system emission might change from amplified spontaneous emission to lasing with coherent feedback [29]. In these coherent RLs, the dependence of the lasing threshold and the number of lasing modes on the relevant length scales such as l_t, the gain

length, l_g, and L have been studied [30]. The spatial profiles of lasing modes were mapped by using the spectrally resolved speckle technique [31]. It was found that the decay lengths of modes are independent of the pumping rate and the excitation area. Besides, it was observed that as the random system moves toward the localisation threshold (kl_t = 1), the size of the lasing modes can be as small as a few microns and can approach that of the optical wavelength. In these micro-RLs, the scattering is so strong that it provides coherent feedback and confines the light in micrometre-sized volumes [32]. Other than making up random media with discrete scatterers and strong short-range disorder, it is possible to form a different type of laser cavity [33-35]. In weakly disordered media such as a conjugated polymer or organic dye-doped gel films, the thickness variation can change the area refractive index and create regions with a relatively higher refractive index to trap light by total internal reflection. The cavities are formed by smooth long-range inhomogeneity, and the size of these cavities is quite large (on the order of hundreds of micrometres).

1.3 Theoretical background

1.3.1 Different light scattering mechanisms

In various situations, light can be scattered, i.e., sent into other directions, usually in random directions. There are two main scattering processes [36]: (I) elastic scattering and (II) inelastic scattering. Elastic scattering means that the wavelength of the scattered light is not changed, apart from a possible Doppler shift due to the movement (Figure 1-1). That implies that the inner energy of the scattering particles is not changed; there is no electronic excitation or de-excitation involved. In other words, here, there is not a permanent exchange of energy between the light and the scattering particle. This restriction of energy exchange does not prohibit a change in direction, but according to Planck's law, it does prohibit a change in frequency.

On the other hand, in the case of inelastic scattering, the inner energy of the scattering particles changes. In the inelastic process, permanent energy exchange happens, and the energy content of the matter after the interaction is either higher or lower than that in the original state. Due to the conservation of total energy, the energy of the emitted radiation is changed as well, resulting in a change of frequency. Raman, Brillouin, and Compton scatterings are examples of inelastic scattering processes.

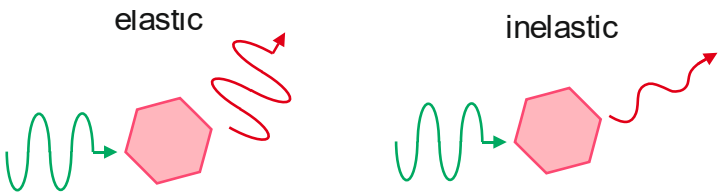

Figure 1-1: Elastic and inelastic scattering processes.

In RLs, where the scattering is mainly because of the randomly oriented particles, elastic scattering mostly happens. Depending on the size of the scatterers relative to the wavelength of the light, two scattering processes mainly occur in the disordered media: Rayleigh scattering and Mie scattering.

Rayleigh scattering: This scattering happens for very tiny particles when the size of the particles is much smaller than the wavelength of the incident electromagnetic radiation (about a tenth of the wavelength). As shown in equation (1.1), the scattering intensity depends very strongly on the particle's wavelength and size.

$$I = I_0 \frac{8\pi^4 N_s \alpha^2}{\lambda^4 R^2}(1+\cos^2\theta) \tag{1.1}$$

In equation (1.1), α is the polarizability, N_s is the number of scatterers, θ is the scattering angle, n is the refractive index, and R is the distance from the scatterer. In this type of scattering, the scattering is almost isotropic (Figure 1-2), and the anisotropy factor is almost zero.

Mie scattering: When the particle size is larger than the incident wavelength, Mie scattering becomes predominant. This scattering, unlike the Rayleigh scattering, is wavelength-independent. The anisotropy factor in Mie scattering is non-zero, and as the scattering particle gets bigger, the anisotropy factor increases.

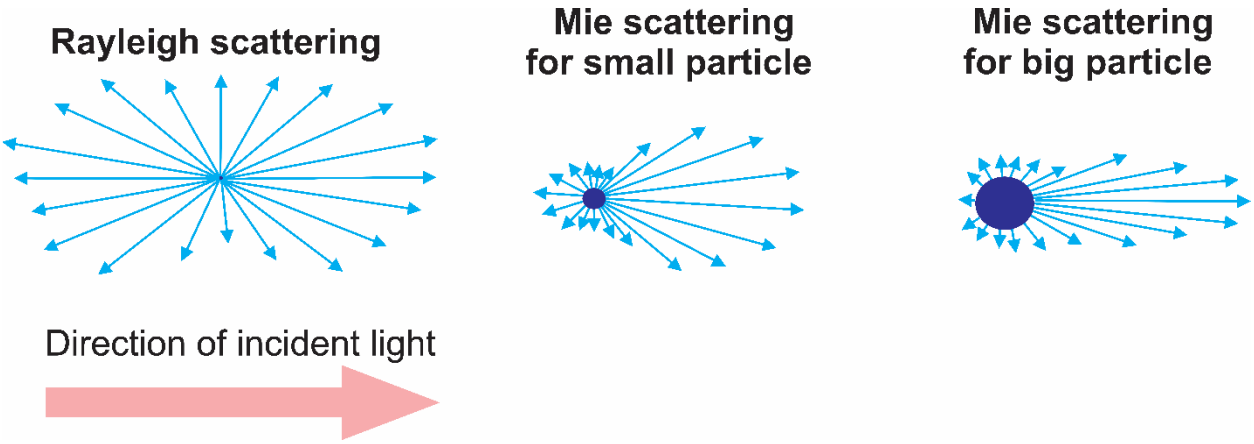

Figure 1-2: Light scattering pattern in Rayleigh and Mie scatterings for small and big particles.

1.3.2 Characteristic length scales for random lasers [9]

Correlation radius, R_c: In disordered media, the dielectric constant, ε, is a function of space and fluctuates randomly in space. The autocorrelation of the dielectric constant (i.e., $K(\Delta r) \equiv \langle \varepsilon(r)\varepsilon(r+\Delta r) \rangle$, where <…> represents the ensemble average) decays exponentially within the random media. The decay length of this exponential function [37] is called the correlation radius, R_c, which quantifies the range of the disorder. When $R_c >> \lambda$, light is scattered through long-range disorder, and if R is less than or comparable to the wavelength, the light is deflected by the short-range disorder.

Scattering mean free path, l_s, and transport mean free path, l_t: The transport mean free path is defined as the average distance a wave travels before its direction of propagation is randomised. This length scale is related to the scattering mean free path, l_s, defined as the average distance that light travels between two successive scattering events, through

$$l_t = \frac{l_s}{1-g}, \tag{1.2}$$

where $g \equiv \langle \cos\theta \rangle$ is the anisotropy factor, and θ is the scattering angle. The anisotropy factor, g, is also known as the asymmetry factor or scattering phase function asymmetry. It has a value from -1 (total backscattering), 0 (isotropic scattering) to 1 (total forward scattering) and is defined as:

$$\begin{aligned} g &= \frac{1}{k^2 C_{sca}} \int_0^{2\pi} \int_0^{\pi} F(\theta,\phi) \cos\theta \sin\theta \, d\theta \, d\phi \\ &= \frac{\int_0^{2\pi} \int_0^{\pi} F(\theta,\phi) \cos\theta \sin\theta \, d\theta \, d\phi}{\int_0^{2\pi} \int_0^{\pi} F(\theta,\phi) \sin\theta \, d\theta \, d\phi} \end{aligned} \tag{1.3}$$

In the above equation, $F(\theta, \phi)$ is the angular scattering function which can be obtained through

$$F(\theta,\phi) = \frac{I(\theta,\phi) k^2 r^2}{I_0} \tag{1.4}$$

where I_0 is the intensity of incident light at λ, and $I(\theta,\phi)$ is the intensity of light scattered into a direction defined by θ and ϕ.

Scattering efficiency, Q_s, is defined as the ratio of the scattering cross-section to the averaged projected area (shadow) of the particle [38]. Mathematically, it is defined as:

$$Q_s = \frac{\sigma_s}{A_p}, \tag{1.5}$$

where σ_s is the scattering cross-section and A_P is the shadow of the particle. The scattering cross-section is obtained by integration of the differential scattering cross-section ($d\sigma_s$). The differential scattering cross-section is the probability that a photon impinging on the sample is scattered into a unit solid angle in the given direction [39], that is, the number of particles scattered into a unit solid angle in a given direction per second divided by the flux of the incident beam.

The scattering cross-section is an important length scale in RLs. It can be used to calculate the scattering mean free path through

$$\frac{1}{l_s} = s_s N_s, \tag{1.6}$$

and using equations (1.6) and (1.2), it is possible to calculate the transport mean free path.

Gain length, l_g, and amplification length, l_{amp}: The amplification of light by stimulated emission in disordered media is described by the gain length, l_g, and the amplification length, l_{amp}. The first length scale is defined as the path length over which the intensity of the light, I_0, is amplified by a factor e (Figure 1-3), and the latter length scale is defined as the root mean square distance between the beginning and ending points for different paths of length l_g. In a homogeneous medium, where there isn't any light scattering, light travels in a straight line, so $l_{amp} = l_g$. However, for diffusive samples, $l_{amp} = (D\tau_{amp})^{1/2} = (D\, l_g/v)^{1/2}$, where D and v are the diffusion coefficient and the speed of light, respectively. In 3D diffusive systems, $D = vl_t/3$, leading $l_{amp} = (l_t l_g/3)^{1/2}$.

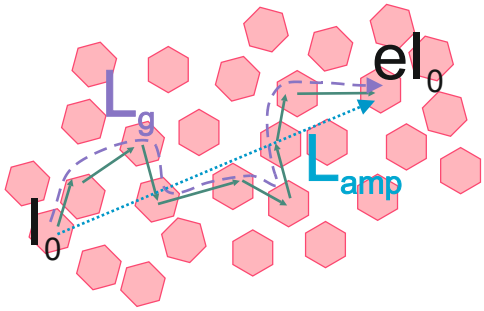

Figure 1-3: Gain length, l_g, and the amplification length, l_{amp}, in diffusive systems

Dimensionality, *d*, and size, *L*: The transport of light in disordered media depends on the system dimensionality, d, and size, L, where for $d > 1$, L refers to its smallest dimension. In passive diffusive random media, the average trapping time of photons is $\tau_d = L^2/D$. In an active

random medium, the gain volume is generally smaller than the volume of the entire random media because usually, only part of the disordered medium is pumped. The gain volume is quantified by its dimension L_g, and $L >> L_g$.

1.3.3 Classification of random lasers based on feedback mechanisms

1.3.3.1 Non-resonant (incoherent) random lasers

Unlike conventional lasers where scattering uncouples the photons from the lasing mode, in RLs, multiple scattering increases the path length or dwell time of light in the active (gain) medium, thus enhancing light amplification by stimulated emission. Considering the phenomenon of diffusive motion for the photons, Letokhov, in 1968 [40], theoretically predicted lasing action in these media. It took around 26 years for the first experimental observation of random lasing using laser dye solutions with TiO_2 particles as the scatterers [41]. In these random media, scattering events only increase the path length of light but not in the formation of closed-loop cavities, the lasing behaviour is referred to as RLs with non-resonant or incoherent feedback [3].

In non-resonant feedback lasers, scattering only returns part of the photons to the gain media but not to the original position; thus, any spatial resonance is absent. Here, a large number of low-Q resonances spectrally overlap and form a continuous spectrum. As a result, the spectrum from such systems does not contain discrete components at specific resonant frequencies and is solely determined by the gain curve of the active medium (Figure 1-4). Thus, this process is essentially the amplification of spontaneous emission whereby lasing occurs at the frequency where the gain is maximum, and the emitted light is not coherent. However, because the modes are coupled, the photon loss rate is lower and usually occurs at lower pumping thresholds. Due to the relationship between optical gain and cavity loss, as the volume of the resonator is reduced, the gain volume is also reduced. This may lead to an increase in lasing threshold and even in some cases unattainable lasing [42]. Thus, in non-resonant lasers where the threshold is relatively low, small volume lasing could be achieved much more easily.

1.3.3.2 Resonant (coherent) random lasers

Later on, in the late 90s, it was shown experimentally that scattering not only could increase the dwell time of the light, but could also increase the probability for the light to create a closed-loop path and allow its return back to its origin, thus forming a scattering-based cavity (Figure 1-4) [43]. These recurrent scattering events could result in minimal leakage for the resonant

wavelengths owing to the destructive interference of light leaking out of the cavity. As such, under certain conditions lasing action in a RL can be of a resonant nature with coherent feedback.

In the resonant feedback RLs, scattered light is trapped in a closed loop where the interference effect occurs. Unlike the broad spectrum of non-resonant lasers, here, some resonant peaks appear in the spectrum. Because of the nature of the feedback, the emitted light is more coherent and can lase at different (resonant) wavelengths. This is an advantage of resonant feedback RLs since it enables the tuning of the lasing wavelength. The main characteristic of the resonant feedback lasers is the sharp laser peaks in the spectral emission, which is the fundamental difference between the features of a RL with coherent feedback and that with incoherent feedback.

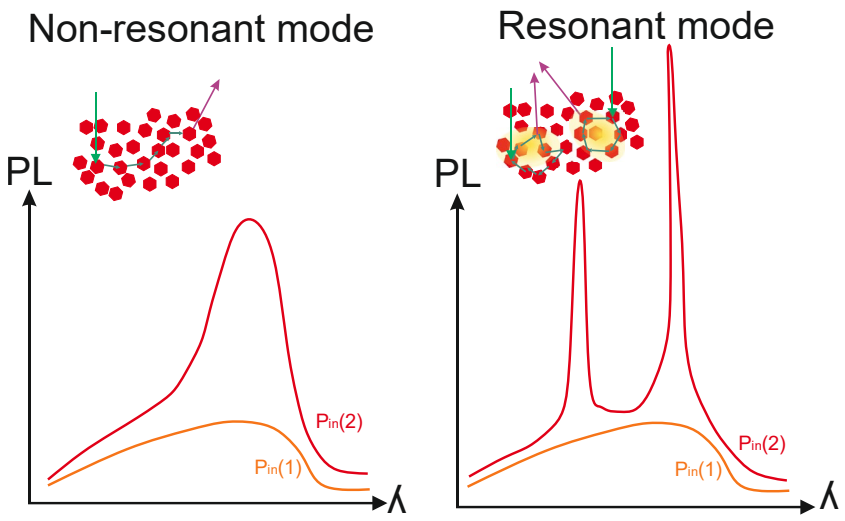

Figure 1-4: Resonant mode vs non-resonant mode ($P_{in}(2) > P_{in}(1)$).

1.3.4 Different regimes in random lasers

Three regimes for light transport have been identified for random media: (I) ballistic, (II) diffusive, and (III) Anderson localisation regimes. These regimes are defined in terms of l_t, λ, or the wavevector, $k=2\pi/\lambda$, and the size of the system contributing to scattering, L.

Ballistic ($L \simeq l_t$): Ballistic regime is where photons travel through a scattering (turbid) medium in a straight line. The ballistic light is the fraction of light that does not experience scattering and preserves the characteristics (polarisation, coherency, and directionality) of the incident light [44]. In the ballistic regime, if any photon experiences scattering, the transport regime will no longer be ballistic. So, in this regime, the scattering mean free path is the most important parameter [45].

Diffusive ($L >> l_t >> \lambda$): In the diffusive regime, unlike the ballistic regime, the propagation of the light is affected by multiple scattering, and photons experience multiple scattering before being detected. Since multiple scattering happens in this regime, the scattering mean free path, which quantifies the distance between successive scattering events, becomes less important. On the other hand, the scattering angle becomes more significant. Therefore in this regime, the transport mean free path is the length scale describing these systems.

Localisation regime ($k \cdot l_t \approx 1$): The idea of localising a wave in a random structure was first proposed by Anderson for localising electrons [46], but due to the nature of these Fermion particles, it was not practical. So, the idea of Anderson localisation was extended to the photons resorting to the wave nature of photons [47]. However, the first experimental work to show the Anderson localisation took place about 20 years after the idea of shifting from electrons to electromagnetic waves [48].

It is shown that, in strong scattering media, where l_t is small enough, the scattering path can create closed loops leading to spatial localisation of light. From a mathematical viewpoint, Anderson localisation means that the eigenmodes of the wave equation decay exponentially from their centre, and the size of these modes is 2ξ, where ξ is the localisation or decay length [49]. As mentioned, to achieve localisation in RLs, l_t should be small enough. A large index contrast between scatterers and background medium would lead to bigger σ_s according to the Mie theory [39], which according to equations (1.2) and (1.6), would lead to smaller l_t. So, a high refractive index contrast is necessary for the disordered media to lase in the Anderson localisation regime.

1.3.5 Different lasing parameters in random lasers

1.3.5.1 Quality factor and mode volume

Two characteristic parameters, which figure prominently in the physics and device applications of cavities, quantify the ability of the cavity to boost light-matter interactions, i.e. the quality factor Q and the mode volume V [42, 50]. Q governs the enhancement due to temporal confinement, and V is an important notion, that determines the enhancement due to spatial confinement and is directly related to the mode normalisation, which prefigures how much a mode is excited by an external source. Cavities with high Q-values and small mode volumes provide enhanced light-matter interaction and are of fundamental and technological interest.

Quality factor: Quality (Q) factor, Q, of an optical cavity is a quantity that measures how well the cavity can store energy. It is proportional to the ratio of the energy stored by the standing wave and the energy loss per cycle and can be calculated through [51]

$$Q = 2\pi \frac{E_{stored}}{E_{loss\ per\ cycle}} = \frac{\nu_0}{\delta\nu} = 2\pi\nu_0\tau_p, \tag{1.8}$$

where ν_0 , τ_p and $\delta\nu$ are the resonator frequency, photon lifetime and resonance linewidth, respectively. The Q factor also has a relation with threshold gain, g_{th}. Assuming a small spontaneous emission factor, β_{sp}, these two parameters are related through

$$\Gamma g_{th} = \frac{2\pi\nu_0}{v_g Q}, \tag{1.8}$$

where Γ and v_g are the confinement factor and group velocity, respectively. So, according to the above equation, cavities with high Q factors are required [52] to fabricate low threshold lasers.

Effective mode volume: It is customary to define the effective mode volume for normal modes, V_{eff}, as [53, 54]

$$V_{eff} = \int \frac{\varepsilon(r)\left|E(r)\right|^2}{\varepsilon(r_c)\left|E(r_c)\right|^2} dr = \frac{\int \varepsilon(r)\left|E(r)\right|^2 dr}{\max(\varepsilon(r)\left|E(r)\right|^2)} \tag{1.9}$$

where r_c is the position where the field is maximum, $\epsilon_r(r)$ is the relative permittivity, and $E(r)$ is the electric field of the mode. It is no exaggeration to say that this equation has been the workhorse for cavity physics for decades, but it turns out to be incorrect for any cavity with dissipation and hence a finite Q value. The problem with this equation, especially when applied to leaky cavities, is that the mode diverges in space. In the case of modes with high Q factors, the leakage is much smaller, and the divergence as a function of integration volume is relatively slow. It has been shown for high Q factor cavities, calculating the mode volume by introducing a cut-off has provided values with good agreement with experimental results [55].

1.3.5.2 Gain, modal gain, and confinement factor

Gain: Optical gain of a material is the most important requirement for the realisation of semiconductor lasers because it describes the optical amplification in the semiconductor

material. Optical gain in semiconductors occurs because of stimulated emission of the photons created by the recombination of electrons and holes. In other words, optical gain in semiconductors is caused by photon-induced transitions of electrons from the conduction band to the valence band. While in other laser materials like gas lasers or solid-state lasers, the processes associated with optical gain are rather simple, in semiconductors, this is a complex many-body problem of interacting photons, electrons, and holes. To calculate the optical gain, using Fermi's golden rule and the k-selection rules, equation (1.10) can be derived for a bulk material [56].

$$g(\hbar\omega) = \frac{\pi q^2}{n_r c \varepsilon_0 m_0^2 \omega} \left\langle \left| \bar{e}.P_{CV} \right|_b^2 \right\rangle \int \rho_r(E) \left[f_c(E) - f_v(E) \right] L(E_g + E - \hbar\omega) dE, \tag{1.10}$$

where $f_{v(c)}(E)$ is the Fermi-Dirac distributions for valence (conduction) band, k_B, $\hbar$, and q are the Boltzmann, reduced Planck constants, and elementary charge, respectively, $\rho_r(E)$ is the three-dimensional joint density of states, c is the speed of light in free space, n_r is the refractive index of the material, ε_0 is the permittivity of the free space, m_0 is free electron mass, E_g is the material bandgap, $L(E_g+E-\hbar\omega)$ is the lineshape broadening function, E is related to the electron-hole recombination energy (E_{21}) by $E=E_{21}-E_g$, and $\left\langle \left| \bar{e}.P_{CV} \right|_b^2 \right\rangle$ is the average of the momentum matrix element of the bulk semiconductor.

Three-dimensional joint density of states, $\rho_r(E)$: The 3D joint density can be calculated through

$$\rho_r(E) = \frac{1}{2\pi^2} \left(\frac{2m_r^*}{\hbar^2} \right)^{\frac{3}{2}} \sqrt{E} \quad , \quad \frac{1}{m_r^*} = \frac{1}{m_e^*} + \frac{1}{m_h^*}, \tag{1.11}$$

where m_r^* is the reduced mass dependent on the electron (m_e^*) and hole (m_h^*) effective mass. The density-of-state effective mass of the valence band is used for the hole effective mass [57].

Fermi-Dirac distributions: Fermi-Dirac distributions relates the carrier density to the optical gain and can be calculated using the following relations.

$$f_v(E)=\frac{1}{1+\exp\{\frac{-(m_r/m_h^*)E-F_v}{k_BT}\}} \quad , \quad f_v(E)=\frac{1}{1+\exp\{\frac{E_g+(m_r/m_e^*)E-F_c}{k_BT}\}}$$
$$F_c=E_c+KT\ln(\frac{N}{N_c}), \quad N_c=2\left[\frac{2\pi m_e^* KT}{h^2}\right]^{3/2} \tag{1.12}$$
$$F_v=E_v-KT\ln(\frac{P}{N_v}), \quad N_v=2\left[\frac{2\pi m_h^* KT}{h^2}\right]^{3/2}$$

In equations (1.12), N_c (N_v) is the effective density of states in the conduction (valence) band, F_c and F_v are the quasi-Fermi levels, which are dependent on the level of doping concentration and carrier injection, N is the carrier density in the conduction band, P is the carrier density in the valence band (for an un-doped material, charge neutrality requires $P = N$) and T represents temperature. To calculate the quasi-Fermi levels, an approximate formula for the Fermi-Dirac integral is used [56, 58].

Momentum matrix element of InP and the Lorentzian function: In practice, an energy parameter, E_p, for the matrix element of a semiconductor is defined as [56]:

$$<\left|\bar{e}.p_{cv}\right|^2>=\frac{m_0}{6}E_P, \quad E_P=\frac{2m_0}{\hbar^2}P^2 \tag{1.13}$$

where E_P is taken from experimental data. The lineshape broadening function can be approximated by a Lorentzian lineshape function through

$$L(E_g+E-\hbar\omega)=\frac{1}{\pi}\frac{\hbar/\tau_{in}}{(\hbar/\tau_{in})^2+(E_g+E-\hbar\omega)^2}, \tag{1.14}$$

or

$$L(E_g+E-\hbar\omega)=\frac{1}{\pi\gamma}\mathrm{sech}(\frac{E_g+E-\hbar\omega}{\gamma}), \tag{1.15}$$

where γ is the FWHM and τ_{in} is the intraband relaxation time [59], which is the time constant associated with the exponential decay of the electron. The temperature and the γ parameter in the previous equations could be obtained by fitting the spontaneous emission spectrum. The theoretical spontaneous emission spectrum for a semiconductor, based on the band-to-band recombination model, is given by

$$r_{sp}(\hbar\omega) = \frac{2n_r q^2 \omega}{hc^3 \varepsilon_0 m_0^2} \left\langle \left| \hat{e}.P_{CV} \right|_b^2 \right\rangle \int \rho_r \left(E\right) f_c(E)(1 - f_v(E))\, L(E_g + E - \hbar\omega) dE, \tag{1.16}$$

where *h* is the Planck constant.

Modal gain: In a laser cavity, the mode volume may not completely overlap with the gain region. Hence, only the mode's overlap with the gain region will contribute to gain in the cavity. The modal gain, <*g*>, is thus defined as the net gain of an optical mode. Since the stimulated emission rate is proportional to the square of the electric field, the electric field pattern of the mode of interest can act as a weighting function through equation (9) to calculate the net effect of $g(x,y,z)$

$$\left\langle g \right\rangle = \frac{\int E^*(x.y.z) g(x,y,z) E(x,y,z) dV}{\int \left| E(x,y,z) \right|^2 dV} \quad , \tag{1.17}.$$

where *V* is the volume of the medium.

For lasing to occur, the modal gain should be positive, i.e. the effective gain of the mode can overcome the cavity losses.

Confinement factor: In semiconductor lasers, because the cavity volume occupied by photons, V_p, is usually larger than the active region volume occupied by electrons, V, the photon density generation rate will be $[V/V_p]R_{st,}$ not just R_{st}, where R_{st} is the net stimulated recombination rate. This electron-photon overlap factor, V/Vp, is generally referred to as the confinement factor, Γ. To calculate the confinement factor, Γ, after calculating the modal gain, equation (1.18) below is used

$$\Gamma = \frac{\left\langle g \right\rangle}{\frac{1}{V} \int g(x,y,z) dv} \tag{1.18}.$$

Chapter 2: Numerical and experimental techniques

In this chapter, the numerical and experimental techniques used to conduct the projects are presented. The numerical methods were used to design the random media to satisfy the modes' localisation and achieve high-quality factor modes. Besides, these numerical methods also allow a deeper understanding of the fundamental mechanism happening in the disordered media. Different experimental techniques were used to fabricate and characterize the structural and optical properties of the random nanowire (NW) arrays.

2.1 Electromagnetic modelling

To design and understand the random media behaviour, the essential part is to understand the interaction of light with the system. As the light enters the random media, it interacts with the optical and material properties of the system. Light is an electromagnetic field that has both electric and magnetic fields, which are related to each other by Maxwell's equations. So, solving Maxwell's equations will give the light components as a function of position and wavelength. Calculating these fields in the random media will help better understand the electromagnetic field's interaction with the material.

Analytical methods can be used to solve the Maxwell equations. However, analytically calculating these coupled equations is not straightforward in complex media, such as disordered systems. Therefore, numerical methods such as the finite element and Finite-Difference Time-Domain (FDTD) methods are usually used to solve Maxwell's equations and calculate the electromagnetic field. Obtaining the electromagnetic field would lead to the calculation of different system parameters, including carrier generation, modal gain, material gain, and lasing mode parameters, including Q factor, wavelength resonance, and mode volume.

In this thesis, Lumerical FDTD Solutions was used to solve Maxwell's curl equations in three dimensions. In the next section, this method is described in more detail.

2.1.1 Finite Difference Time Domain (FDTD) solver

To solve Maxwell's equations in complex geometries (such as disordered media) [49, 60], the Finite-Difference Time-Domain (FDTD) [61, 62] method is used. As this method solves Maxwell's coupled equations in both time and space domains, it can provide a deep and unique insight into different problems in optics and photonics. Using Fourier transforms, it is possible

to obtain the frequency solution; therefore, different useful quantities such as lasing modes, cavity properties, and complex Poynting vector could be calculated.

The FDTD solves the coupled Maxwell's equations (equation (2.1)) in non-magnetic materials:

$$\begin{aligned} &\frac{\partial \vec{D}}{\partial t} = \nabla \times \vec{H}, \\ &\vec{D}(\omega) = \varepsilon_0 \varepsilon_r(\omega)\vec{E}(\omega), \\ &\frac{\partial \vec{H}}{\partial t} = -\frac{1}{\mu_0}\nabla \times \vec{E} \end{aligned} \tag{2.1}$$

In the above equation, H, E, and D are the magnetic, electric, and displacement fields, respectively, while ε_0 and μ_0 are the permittivity and permeability in free space and $\varepsilon_r(\omega)$ is the complex relative dielectric constant and depends on the dispersive refractive index through $\varepsilon_r(\omega)=n^2(\omega)$.

In 3D structures, Maxwell equations have three field components for the electric and magnetic fields: E_x, E_y, E_z and H_x, H_y, and H_z. Assuming the structure to be infinite in the z dimension, the fields would be independent of z, which means

$$\begin{aligned} &\varepsilon_r(\omega, x, y, z) \to \varepsilon_r(\omega, x, y), \\ &\frac{\partial \vec{E}}{\partial z} = \frac{\partial \vec{H}}{\partial z} = 0 \end{aligned} \tag{2.2}$$

Under this condition, the Maxwell equations will split into two sets of equations, with each of these two sets having three components in the transverse plane (x-y plane). In one set termed as transverse electric (TE) modes, there is no electric field in the direction of propagation. These are sometimes called H modes because there is only a magnetic field along the direction of propagation. However, in the other set termed as transverse magnetic (TM) modes, which are also called E modes, there is only an electric field along the direction of propagation. Considering these two waveguide modes, the two sets of Maxwell equations will have the following components for each of the modes: TE: E_x, E_y, H_z, and TM: H_x, H_y, E_z.

For example, in the TM case, Maxwell's equations (equation (2.1)) reduce to:

$$\frac{\partial D_z}{\partial t} = \frac{\partial H_y}{\partial x} - \frac{\partial H_x}{\partial y},$$
$$D_z(\omega) = \varepsilon_0 \varepsilon_r(\omega) \vec{E}_z(\omega), \tag{2.3}$$
$$\frac{\partial H_x}{\partial t} = -\frac{1}{\mu_0}\frac{\partial E_z}{\partial y},$$
$$\frac{\partial H_y}{\partial t} = \frac{1}{\mu_0}\frac{\partial E_z}{\partial x}.$$

The FDTD method grids the structure and solves these equations on these grids, which are discretized in spatial and temporal domains. As shown in Figure 2-1, each field component is obtained at slightly different positions inside the grid cell (Yee cell [63]), and then these values are interpolated to the origin of each grid.

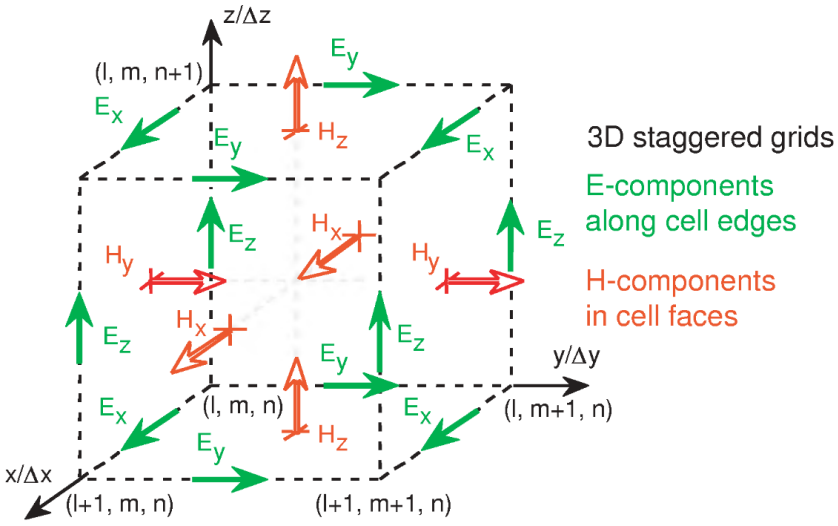

Figure 2-1: 3D Yee cell showing the positions of different field components on the grid. The image is taken from [64].

2.2 Nanowire synthesis and growth

2.2.1 Epitaxial growth

In the semiconductor industry, epitaxial growth is commonly used to grow semiconductor films on semiconductor substrates/wafers. The term epitaxy comes from the Greek roots epi, meaning "above", and taxis, meaning "an ordered manner". Unlike amorphous growth or multi-crystalline growth, in epitaxial growth, the new crystalline layers are formed with one or more well-defined orientations with respect to the crystalline substrate. The relative orientation(s) of the epitaxial layer (or the deposited crystalline film) to the crystalline substrate is defined in terms of the orientation of the crystal lattice of each material. For epitaxial growth, the new layer must be crystalline, and each crystallographic domain of the overlayer must have a well-defined orientation relative to the substrate crystal structure. For semiconductor technology,

single domain epitaxy (in which the overlayer crystal has one well-defined orientation with respect to the substrate crystal) is preferred. In epitaxial growth, the grown material can have the same chemical composition of the substrate (homo-epitaxy [65]; for example, growth of InP on InP substrates) or can have a different chemical composition (hetero-epitaxy; for example, growth of GaAs on silicon substrates) [66].

There are two main epitaxial growth techniques: (i) Metalorganic vapour phase epitaxy (MOVPE) and (ii) molecular beam epitaxy (MBE). In MOVPE, also known as organometallic vapour phase epitaxy (OMVPE) or metalorganic chemical vapour deposition (MOCVD), the growth of the crystalline layers is by chemical reaction and not a physical deposition, unlike MBE. Here, the deposition usually occurs in gas-phase reactions at reduced pressures (10 to 760 Torr). In MOVPE, the gaseous form of the materials to be grown are mixed, and the chemical reactions of these gases on the surface of the substrate lead to the epitaxial growth of the layer.

To grow III-V semiconductors, the metalorganic precursors, usually in liquid or solid forms, and group V-hydrides, usually in gaseous form, are typically used as group III and V sources. To mix the precursors, usually, H_2 carrier gas is bubbled through the metalorganic source. It picks up some of the metallic vapour, and this vapour is carried to the reaction chamber and mixed with group V-hydrides. Then, the reaction happens between these two precursors on the surface of the substrate, and crystalline growth occurs. During growth, the pressure and total flow rate of the gases into the reactor are usually kept constant and are not changed from the optimized value to achieve uniform growth. Usually, other growth parameters, such as temperature, the molar flow rate of each reactant gas, and their ratio (V/III ratio), are changed to control the layer's growth rate, composition, and doping level.

2.2.2 Different III-V nanowires growth mechanisms

III-V nanowires can be synthesized mainly by two methods: (i) top-down and (ii) bottom-up approaches. In the top-down method, like carving a statue from a block of marble, the bulk of the material after patterning is removed through an etching process to create the NWs. In this method, the etching process may introduce surface defects and deteriorate the optical and electrical properties of the NW, hindering their application for light sources such as lasers. In the bottom-up method, using chemical synthesis, molecules are assembled one by one and scaled up to produce structures orders of magnitude bigger than the initial molecule. The bottom-up method itself can be separated into two main categories: (i) with catalyst and (ii) catalyst-free processes. The former uses nanoparticle catalysts and gas-phase precursors and

includes the common vapour-liquid-solid (VLS) [67] and vapour-solid-solid (VSS) [68] techniques. In the latter, NWs are grown without the help of catalysts and consist of selective-area epitaxy (SAE) [69] and oxide-assisted growth (OAG) [70].

VLS is a much easier method than SAE to grow NWs. However, it could have the following problems:

- Catalyst atoms may be directly incorporated into the NWs, especially in Si [71], thereby affecting the structural, electrical and optical properties of the NWs

- Growing larger diameter NWs and removing the catalyst contamination [72] add complexity to the growth

- NWs grown with the VLS method usually face tapering issues [73].

On the other hand, the SAE-grown NWs can mitigate these problems, but preparing the SAE substrate is a more time-consuming and less cost-effective procedure. Besides, patterning holes or openings with very small sizes is challenging and hence growing very thin NWs is difficult with this technique. Furthermore, it is more challenging to obtain ultra-sharp axial heterostructures using SAE [74].

In this thesis, to grow the InP NWs used in chapters 3 and 4, the substrates were prepared for the SAE method, and the core-shell GaAs-AlGaAs NWs used in chapter 5 were grown by the VLS method. In both cases, an MOVPE reactor was used to grow the NWs.

2.2.2.1 Vapour-liquid-solid growth of nanowires

In the VLS method, metal nanoparticles such as gold nanoparticles (Au-NPs) are usually used to grow the NWs. This method is commonly used to grow III-V semiconductor nanowires. As shown in Figure 2-2, the first step of the process includes placing the catalyst on the growth substrate, whether by randomly dispersing them or by defining their position using lithographic techniques. Then the substrate with nanoparticles is placed in the MOVPE reactor. After the source materials are introduced in the vapour phase and the growth temperature is ramped up, the metallic Au-NP first forms a liquid eutectic. Then once supersaturation is achieved, the precursor precipitates at the particle interface and substrate, forming a solid NW. The diameter of the NP controls the diameter of the NW. A shell layer could also be grown to increase the diameter or/and passivate the NW or to form a heterostructure by changing the growth conditions.

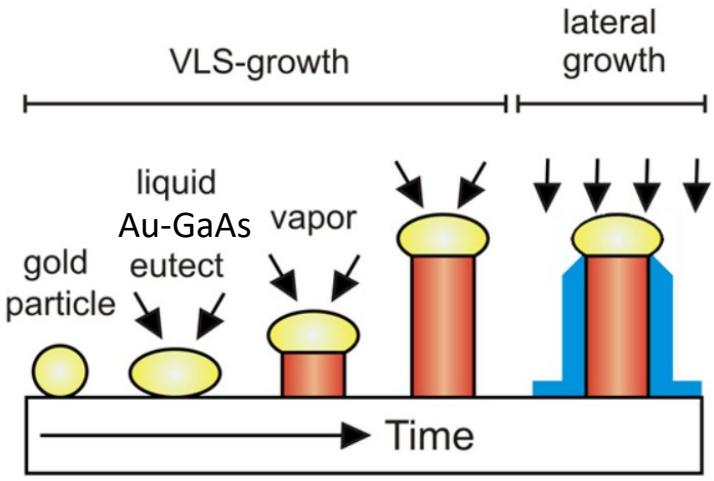

Figure 2-2: Schematic showing epitaxial VLS growth of GaAs nanowires using Au-NP catalyst, including lateral growth to achieve a core-shell structure. The figure has been taken from [75].

2.2.2.2 Selective-Area Epitaxy of nanowires

In the SAE method, a patterned mask is used to define areas where the NWs are grown. Usually, an oxide layer is first deposited on the desired substrate, then using lithographic and etching techniques, some holes/openings are transferred to the oxide mask. Then the patterned substrate is placed at the MOVPE chamber. The openings on the mask exposed the underlying substrate, which acts as the growth seeds for the NWs. The diameter of the NW, in this case, is determined by the diameter of the holes/openings.

Figure 2-3 shows the schematic of the SAE method used to grow the NWs used in Chapters 3 and 4. A 30 nm-thick SiO_x layer is first deposited on the substrate using plasma-enhanced chemical vapour deposition (PECVD). Then, using a spin coater, an electron resist layer (diluted ZEP) of 70-80 nm thick is deposited on the sample, followed by electron beam lithography (EBL) to write the desired pattern on the resist. After writing, a developer (AR 600 546 (n-Amyl Acetate)) is used to remove the exposed regions of the resist. Then using reactive-ion etching (RIE), the pattern is transferred to the oxide mask. The residual electron resist layer is then removed by Di-Methyl Acetate. Finally, after removing the native oxide layer on the exposed regions of the substrate within the etched holes through trim etching (using phosphoric acid solution), the sample is immediately loaded into the MOVPE reactor for growth.

Prior to growth, an annealing step with PH_3 is used to desorb any impurities on the patterned substrate. Growth of the NWs can then proceed using the appropriate growth conditions.

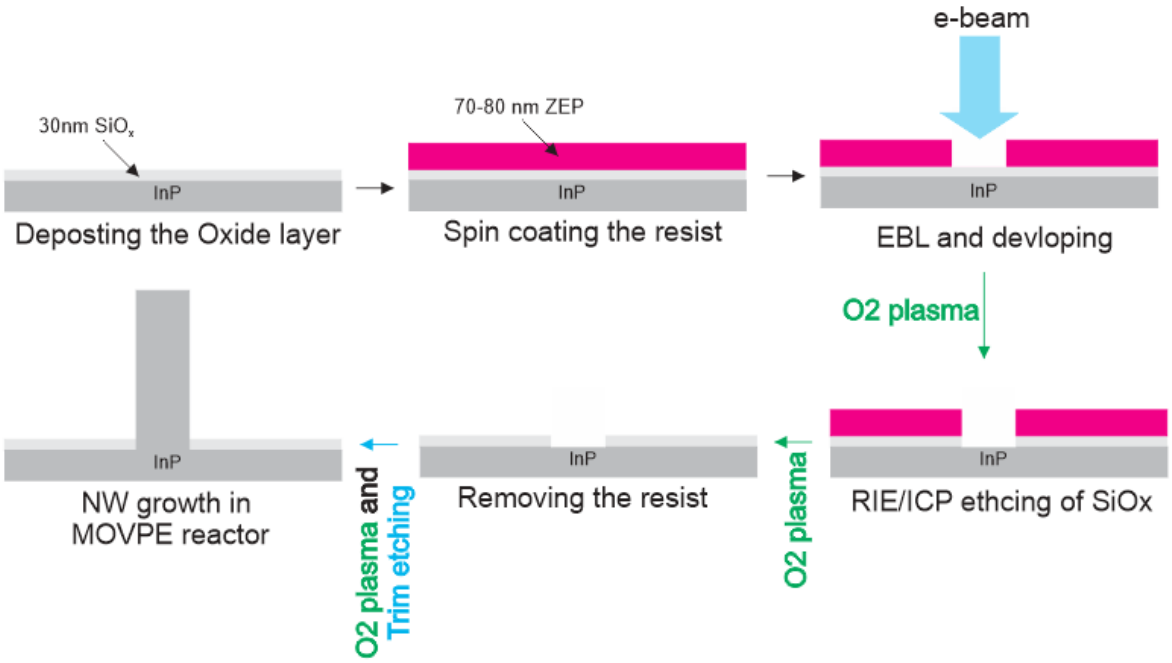

Figure 2-3: Schematic showing SAE growth of InP NWs.

2.3 Patterning substrate for Selective-Area Epitaxy

Randomly positioned holes were created on the SiOx layer using EBL and RIE to prepare the sample for the SAE growth. Considering the unavoidable lateral growth of the NWs and the filling factor of the system, the hole's diameter was chosen in a way to reduce the possibility of NWs merging after the growth. Besides, considering the fabrication process and limitations, the randomness of the NW position distribution was chosen so that the NWs do not overlap greatly. It is first assumed the system has a square photonic lattice, and to create a random system, the NW positions can deviate randomly from their periodic positions (Figure 2-4). The value of this deviation from the centre of the NW, σ_c, is between 0 and 50 nm.

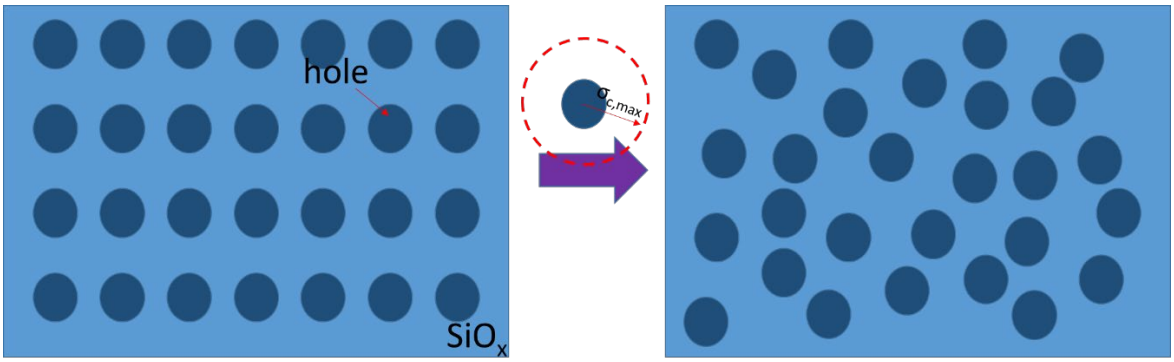

Figure 2-4: Defining randomness of hole patterns on SiOx layer for the SAE growth.

2.4 Characterization of the random nanowire arrays

Semiconductor characterisation is generally initiated immediately after the synthesis of a crystal. We can distinguish three types of characterisation techniques: structural, optical, and electrical. The following sections briefly explain the methods used in this thesis to characterise the disordered NW arrays.

2.4.1 Structural characterisation

To characterise the size and morphology of the NWs, electron microscopy techniques are used.

2.4.2 Scanning Electron Microscopy

A scanning electron microscope (SEM) (Figure 2-5) is a kind of electron microscope that uses a focused electron beam to raster scan the surface of the specimen. The electrons interact with atoms at various depths within the sample, producing various signals that contain information about the surface topography and composition of the sample. Different kinds of signals are produced, including secondary electrons (SEs), reflected or back-scattered electrons (BSEs), characteristic X-rays and light (cathodoluminescence, CL), absorbed current (specimen current), and transmitted electrons. The most common signals used to take images are the first two signals: SEs and BSEs. SEs have very low energies on the order of 50 eV, so they can only escape from the top few nanometers of the sample surface. Hence, by detecting SEs, a high-resolution image of the sample surface can be generated, which can be used for characterizing the size and morphology of the sample. The intensity of SE emitted from the surface of the sample depends on the shape and topography of the sample surface.

BSEs are the reflected beam electrons from the specimen by elastic scattering. The energy of the BSE is higher than the SE, so they come from deeper locations within the sample and have lower resolution. The intensity of BSE depends on the elemental composition (atomic number) rather than the surface morphology. So the image formed by detecting BSE highlights the different elemental compositions of the sample.

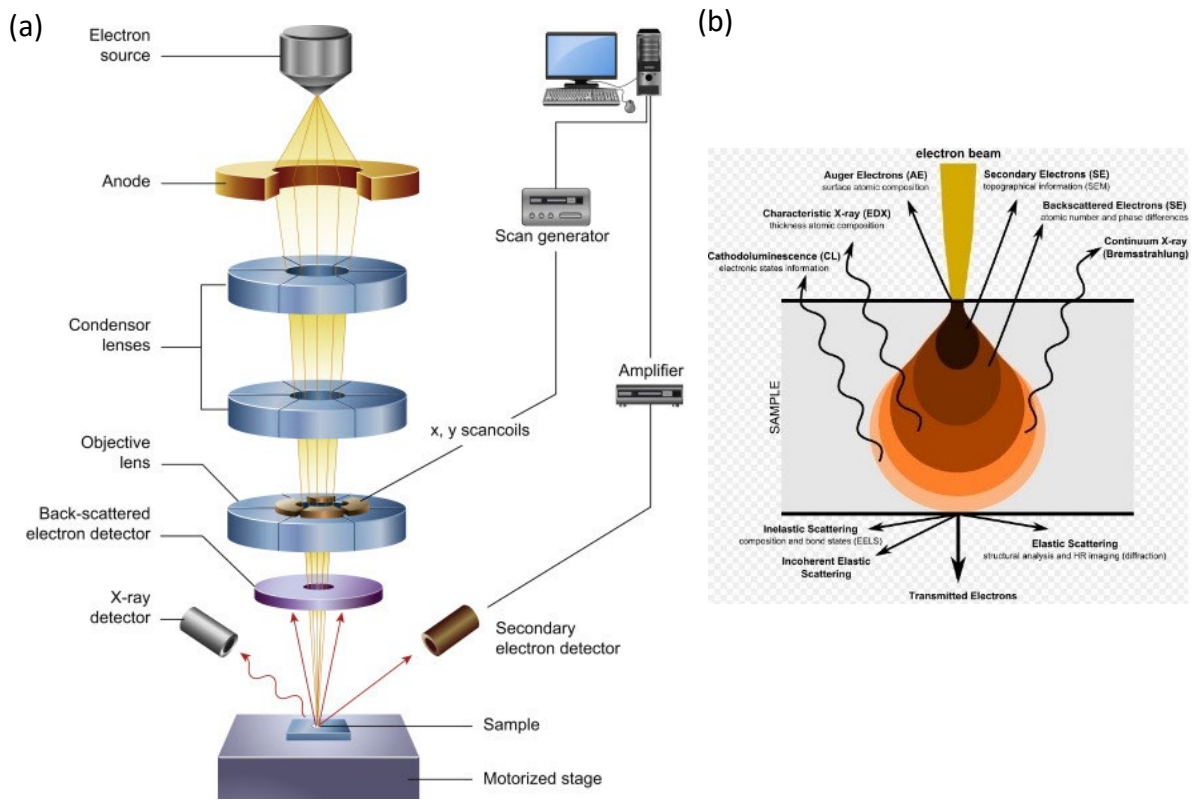

Figure 2-5: (a) Basic components of an SEM, (b) The electron–matter interactions and the various signals generated at different depths. The figures have been taken from [76] and https://www.azom.com/.

2.4.3 Transmission Electron Microscopy

SEM could only give images from the sample's surface; however, photos from the specimen's internal structure could not be obtained by SEM. Besides, the resolution of a typical SEM is 10 nm and could not be used to obtain higher resolution images. So, to get morphological pictures from the interior part of the samples, transmission electron microscopy (TEM) is usually used.

In the conventional TEM (CTEM), the sample is illuminated with an electron beam within a high vacuum chamber. Two types of scattering can occur when electrons hit the specimen: elastic scattering, which produces the diffraction patterns, and inelastic scattering, which gives rise to a spatial variation in the intensity of the transmitted beam. The transmitted electrons are collected using a phosphorescent screen or a camera. The regions where the electrons pass the sample are lighter than regions where the electrons have been reflected [77].

Unlike CTEM, where the electrons pass the whole sample, in another type of TEM known as scanning transmission electron microscope (STEM), the electron beam is focused on a very

fine spot (~ 0.5-2 Angstrom) and then keeping the beam parallel to the optical axis the beam is scanned across the sample.

The raster image created in STEM makes it suitable for analytical techniques such as Z-contrast annular dark-field imaging and spectroscopic mapping by energy-dispersive X-ray (EDX) spectroscopy or electron energy loss spectroscopy (EELS). In STEM, these signals can be obtained simultaneously while taking images allowing direct correlation with the spectroscopic data.

In this project, the SEM was used to see the NWs dimension, including the diameter and length and the system's filling factor. However, STEM was primarily used in GaAs-AlGaAs core-shell NWs to determine the thickness and composition of the core and shell.

2.5 Optical characterisation

Optical measurements are exciting because they are almost always non-contact, with minimal sample preparation, the setups are commercially available and usually automated, and the technique is highly sensitive.

Optical measurements could fall into three main categories [78]:

1- photometric measurements: amplitude of the reflected or transmitted light is measured,
2- interference measurements: phase of the reflected or transmitted light is measured,
3- polarisation measurements: ellipticity of reflected light is measured.

The main optical techniques are summarised in Figure 2-6. In these techniques, it can be observed that light is either reflected, absorbed, emitted, or transmitted.

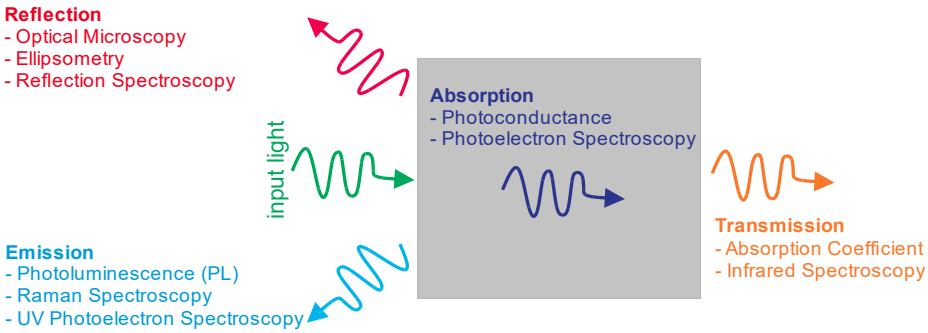

Figure 2-6: Schematic showing the various optical processes and the associated characterisation techniques.

2.5.1 Micro-photoluminescence spectroscopy

Photoluminescence (PL) spectroscopy is a contactless method used for probing the optoelectronic properties of materials [79]. In this spectroscopy technique, light is focused onto the sample, and then through the “photoexcitation” process, the incident photons are absorbed. As a result of the excess energy caused by photo-excitation, electrons jump to allowed excited states. When these electrons move back to their equilibrium states, the excess energy is released through light emission with energy equal to the energy difference between the equilibrium and excited states. This emitted light is then focused and collected by a photon detector through a spectrometer. Different useful parameters could be extracted out through photoluminescence spectroscopy, including bandgap determination, recombination mechanisms [80, 81], material quality and impurity levels, and defect detection [81].

In micro-PL, the PL measurements are conducted on areas typically smaller than one micrometre. Micro-PL can be useful for exciting small objects such as nanocrystals or a micro-region of a bulk structure. For example, in the case of exciting NWs, it can be used to understand whether the broad emission from an ensemble of NWs is due to intrinsic emission or due to inhomogeneous broadening. Or it can be used for exciting different regions of NWs to estimate the type and level of doping [82].

Micro-PL is basically a PL spectroscopy setup combined with an optical microscope. So, the spatial resolution, R, in micro-PL is similar to that of an optical microscope and depends on the objective lens's numerical aperture, NA, according to the Rayleigh criterion R=0.61λ/NA. For a ×60/0.7 NA objective lens, the spatial resolution is around 0.35 – 0.6 μm for wavelengths in the visible range (400 – 700 nm). The micro-PL setup used in this study is shown in Figure 2-7(a), and the schematic diagram of different components of this micro-PL setup used in this study is shown in Figure 2-7(b). A frequency-doubled solid-state laser (femtoTRAIN IC-Yb-2,000, λ = 522 nm, repetition rate 20.8 MHz, pulse width 300 fs) with a Gaussian profile beam shape (FWHM~5 um) was used to pump the NW arrays. The NWs were excited through an aberration-corrected 60×/0.70 numerical aperture, long working distance objective lens (Nikon CFI Plan Fluor), and the resulting emission was collected through the same lens. Most of the experiments carried out in this study were conducted in cryogenic conditions using Janis cryostat connected to liquid He.

The luminescence from the sample (the dashed yellow line in Figure 2-7(b)) was collected by the lens and guided to the spectrometer Acton 2750i. The spectrometer was connected to a CCD camera used to obtain the PL spectrum and spatial near field emission profile of the RL.

To get the PL spectrum, a grating in the spectrometer was used to spread the collected light into a spectrum, which was then collected by the CCD camera. However, for obtaining the emission profile, a mirror was used to direct the collected light to the CCD camera without losing the spatial information of the emitted light from the sample.

(a)

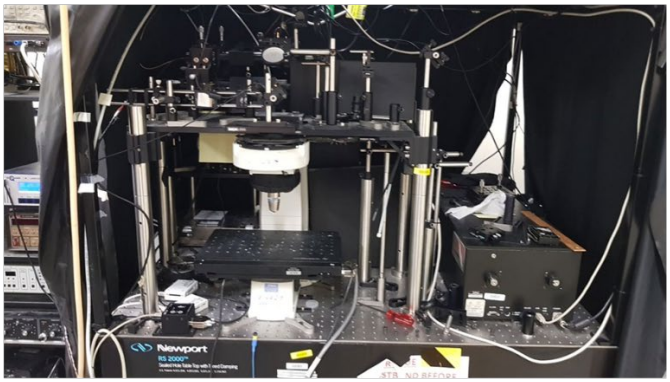

(b)

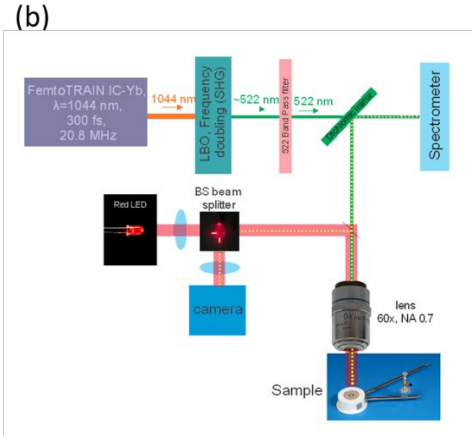

Figure 2-7: (a) Photograph of the micro-PL setup used in this study. (b) Schematic diagram of different components of the micro-PL system.

Chapter 3: Random lasing in Anderson localisation regime

3.1 Introduction

Trying to trap light to increase the interaction of photons with the material is one of the main challenges in many photonic devices, including lasers, photodetectors and solar cells [83]. For this purpose, many different methods such as applying metallic nanoparticles (NPs) to excite localised surface plasmon (LSP) [84], introducing textured surface, and using metal back contact to convert light to surface plasmon polaritons (SPPs) have been employed [85].

One of the other novel ways that seem to help trap light is using disordered media where the random scattering of light would increase the light path and allow the light to get scattered within the material. Anderson first proposed the idea of localising waves in disordered media for localising fermions, such as electrons [46]. Before Anderson's theory, electrons were treated as point-like particles and considering Brownian motion for the electrons, scientists were modelling crystal disorders as perturbations that scatter electrons randomly. However, by resorting to the wave nature of the electron, Anderson found that in disordered media under a broad range of conditions, the wavefunction could show an exponential behaviour, and the electron could be localised. However, due to the temporal variations in the potential (lattice and disorder), temporal fluctuations induced by phonons, the Fermion nature of electrons leading to the interaction of particles such as spin-exchange and Coulomb interaction, scientists were not able to demonstrate Anderson localisation in practice for Fermions. So, resorting to the wave nature necessity of particles in Anderson localisation, the idea of practical localisation by disordered media shifted to other systems such as acoustic waves [86], cold atoms [87] and photons [47]. De Raedt et al., around 30 years ago, theoretically shown the possibility of transverse (optical system that is uniform in one ('longitudinal') direction but contains disorder in the two directions) localisation of light [47]. However, it took around 20 years to experimentally observe transverse Anderson localisation of light in practice [48, 88]. After this, numerous research conducted in this field mainly focused on passive systems, such as fibre optics [89, 90] and disordered dielectric multilayer [91], with only a few reports on using Anderson localisation in the active media such as lasers, solar cells, and photodetectors. For example, Aeschlimann et al. [92] demonstrated the possibility of enhancing the efficiency of the solar cells using the Anderson localisation concept. On the other hand, Liu et al. [93] used Anderson localisation to create cavities in state-of-the-art photonic crystal quantum well waveguides to demonstrate random lasing behaviour.

3.1.1 Anderson localisation in random lasers

As discussed in the previous chapters, RLs could occur due to multiple scattering events within a gain medium, which provides the equivalent feedback mechanism. The unique features of RLs such as angular free emission, tunability of lasing direction, low spatial coherence with high photon degeneracy large area lasing, lasing from flexible substrates, facile fabrication methods and lower cost, make them of great interest for various applications such as in speckle-free laser imaging and display technologies. On the other hand, unlike lasers with conventional cavities, the modes in RLs are coupled and interact with each other due to the mirrorless cavities. This mode coupling would lead to unstable lasing modes, destabilising the lasing behaviour leading to sources whose emission spectra change with time. One way to overcome this issue is to localise the lasing modes, which are spectrally and spatially less coupled. This localisation of the modes could lead to stable multi-mode lasing in RLs.

Localised and delocalised regimes in random lasers: The two essential conditions for random lasing are: (i) multiple scattering of light, (ii) gain overcoming loss. The first condition can occur if the size of the disordered medium, L, is bigger than the transport mean free path, l_t (i.e., $l_t < L$). Depending on the scattering strength, i.e. the relative magnitude of l_t and the light wavelength (λ), random lasing can be divided into two main categories [93]:

(i) Anderson-localised RLs: According to the Ioffe-Regel criterion, ($kl_t \approx 1$, where $k = 2\pi/\lambda$ is the wavenumber) [9], when l_t is smaller than λ (strong scattering regime, $l_t < \lambda < L$) closed paths (resonant modes) could lead to strong interference where the modes are spatially localised and spectrally decoupled due to the small linewidth of the lasing peaks. In the localisation regime, the linewidths of the modes are less than the mode spacing; thus, the modes do not overlap and are uncoupled, apart from the indirect coupling that occurs via the optical gain. So, in this regime, different resonant modes supported in the system could be spatially non-interactive, leading to stable and multi-mode lasing. In this regime, light can be well confined inside the disordered media, leading to behaviour similar to conventional multimode lasers.

(ii) Diffusive (or delocalised) random lasers: Most RLs generally operate in the delocalised regime. In this regime, due to weak scattering, the transport mean free path remains larger than the resonance wavelength (weak scattering regime, $\lambda < l_t < L$), the optical modes are broad and overlap spectrally and spatially, leading to the formation of extended optical modes that cover the entire random medium (Figure 3-1).

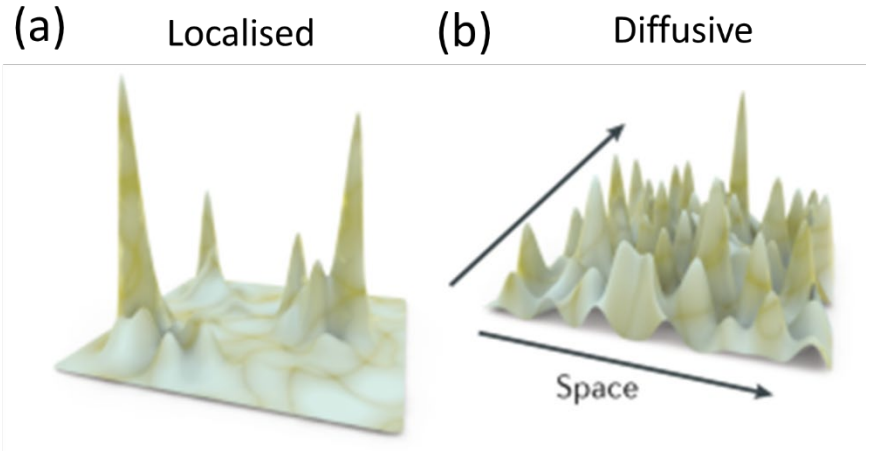

Figure 3-1: Spatial mode profile of the modes of RLs in the localised regime (a) and diffusive regime (b). The figure has been taken from [93].

In most RLs operating in the diffusive regime, no sharp peaks are observed often due to temporal and/or spatial averaging. Instead, an overall linewidth narrowing around a broad lasing peak is observed. However, there are cases where sharp peaks have also been observed in diffusive RLs owing to different reasons, such as the interaction of the lasing modes through the spatial hole-burning or the strong amplification of certain optical paths [93-97]; however, still, the resonance wavelength is generally larger than the transport mean free path.

3.1.2 Strong localisation regime from InP random nanowire arrays

As mentioned, to achieve Anderson localisation in disordered media, the transport mean free path should be smaller than the wavelength of the light. As discussed in chapter 1, in order to decrease l_t, the scattering efficiency of the disordered media should be increased. For this purpose, the scatterers' refractive index contrast relative to the background material's refractive index should increase. It has been shown that high refractive index contrast is essential for strong light scattering and localisation of high quality (Q) factor cavities in the disordered media [49]. Although having high refractive index scatterers is essential to achieve strong scattering and high Q factor cavities, it is insufficient for lasing. For lasing to occur, the gain must also be present, and this can be achieved by incorporating scatterers with gain [98] or adding a separate medium as gain [29].

Most compound semiconductors have a high refractive index compared to air, and due to their direct bandgaps, are excellent candidates as a lasing gain media. In this regard, different semiconductor nanostructures with bandgaps in the UV and visible regions such as ZnO [99],

AlGaN [100], and SnO_2 nanowires (NWs) [101], GaN nanocolumns [102], and ZnS nanospheres [103] have been used in RLs.

Considering the potential of the compound semiconductors, here, InP with a bandgap in the near-infrared region (E_g=1.42 eV at room temperature) acting both as a gain material and the scatterers is used. The high refractive index contrast of InP and free space ($\Delta n \simeq 2.46$) can lead to disordered media with a high scattering efficiency. The disordered media is a random array of InP NWs grown by the SA-MOVPE method and are vertically aligned (Figure 3-2). Using numerical simulations, the array has been designed to support localised and high Q factor modes. We show that our designed InP random nanowire arrays could provide that gain required for lasing and strongly confine light in 3D. The lateral localisation (perpendicular to the NW axial direction) is due to the random scattering, whilst vertical localisation (along the NW axial direction) is provided by the refractive index contrast created by carrier generation at the tip of the NW due to external optical pumping.

This 3D localisation increases the overlap between the gain media and the mode, resulting in a relatively high modal gain and confinement factors, Γ (higher than 0.6). Due to the high scattering efficiency of the designed system, the modes are spatially localised with relatively small localisation lengths, ξ, of 200-500 nm. This localisation has led to stable multi-mode lasing, both spatially and temporally.

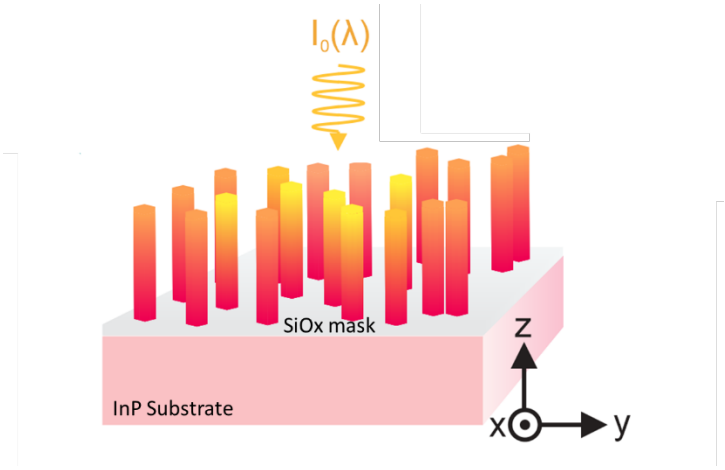

Figure 3-2: Schematic of the InP vertical random nanowires. The nanowires are illuminated from the top by a pulsed laser with an intensity of $I_0(\lambda)$.

3.2 Design of the disordered medium

3.2.1 Localisation regime in a random nanowire array

According to the Ioffe-Regel criterion, the transport mean free path of the light should be smaller than the wavelength of the light. For this purpose, the scattering efficiency of the system should be big enough to make the transport mean free path small (equations (1.2)-(1.6)). In this regard, the geometrical parameters of the disordered medium, such as the diameter, length and density of the NWs (filling-factor of the system), are designed so that the Ioffe-Regel criterion is achieved for the wavelength of interest.

To calculate l_t, the first step is to calculate the anisotropy factor, g, which according to equation (1.3), depends on the angular scattering function, F(θ, ϕ). To calculate F(θ, ϕ), the forward and backward scattering intensity fields are obtained. Since NW is not a completely symmetrical object like nano-sphere and has two geometrical parameters - length and diameter, the fields are calculated for an incident source with two directions: (i) axial direction (z-direction Figure 3-2) and (ii) radial direction (y-direction Figure 3-2). For each source, two polarisations are used (for the z-direction source, the two polarisations are in the x and y directions, and for the y-direction source, polarisations are in the z and x directions.) So, for each system with a particular diameter and length, 2 (polarisation) × 2 (direction) = 4 different source setups are used.

The average forward and backward scattering intensity fields are plotted for a NW with a diameter of 140 nm and length 4 μm in Figure 3-3. It can be seen that when the source is in the y-direction, the backward and forward fields are similar; however, when the source is along the z-direction, the two fields become different. This is because of the smaller size of the NW in the xy direction relative to the NW size in the zx (or zy) direction. That is to say, in the z-direction (L=4 μm), the NW is much bigger than the wavelength of the light (λ_{source}=850 nm), leading to Mie scattering (anisotropic scattering), but in the y (or x-direction), the NW diameter is much smaller than the excitation wavelength leading to Rayleigh (isotropic scattering). After calculating the far-field intensities, equations (1.3) and (1.4) are used to calculate the anisotropy factor, g, for each direction. In the case of the source in the z-direction, the anisotropy value is around 0.22; however, for the source in the y-direction because of isotropic scattering, the g value is 0. After calculating the g value for each direction, equations (1.2) and (1.6) are used to calculate the transport mean free path.

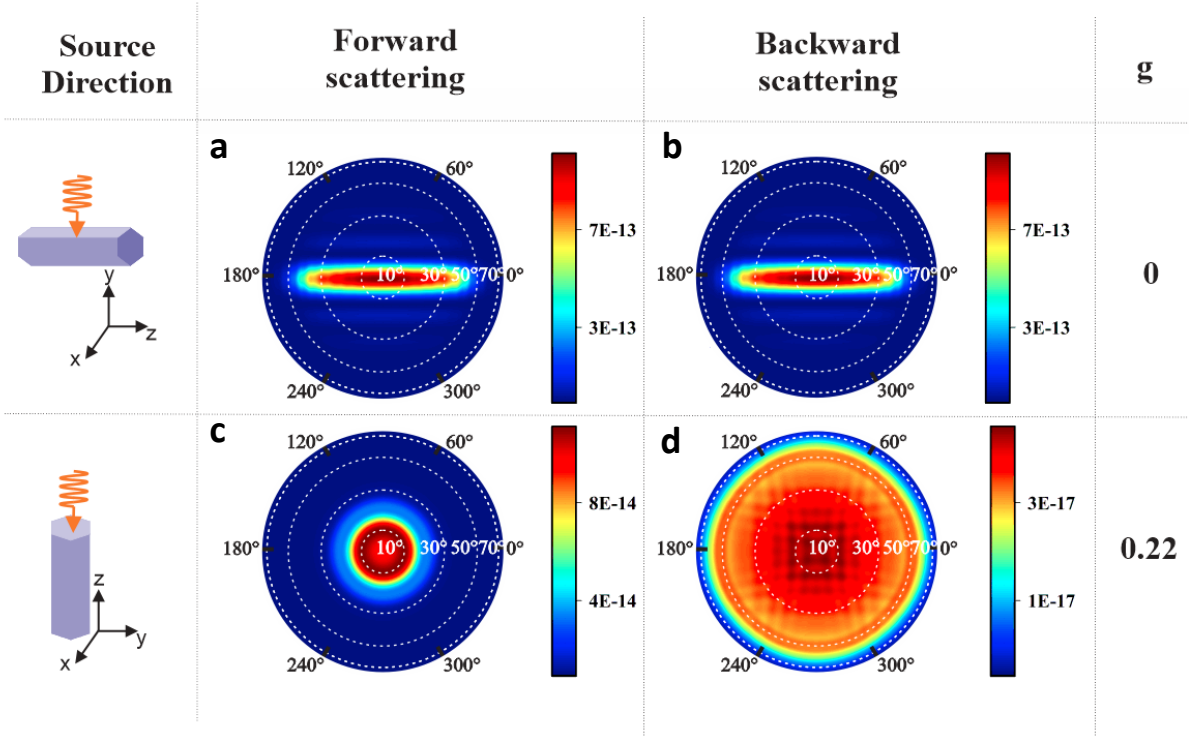

Figure 3-3: The average far-field electric field intensities of the forward and backward scatterings for a nanowire with d=140 nm and L=4 μm under excitation from two different directions. (a) Forward scattering and (b) backward scattering when the light is perpendicular to the NW axial direction, (c) forward scattering, and (d) backward scattering when the light is parallel to the NW axial direction. The dashed circles with the corresponding number indicate the azimuthal angle, θ. The polar angle, φ, is shown by the black numbers around the circle. The asymmetry factor, g, for each source direction is also calculated and displayed in the right-hand column.

In Figure 3-4, the scattering efficiency, Q_s, and transport mean free path, l_t, for NWs with different diameters and densities (or filling factors) are plotted. It can be seen (Figure 3-4(a) and Figure 3-4(b)) the scattering efficiency for incident light in the z-direction is generally larger than excitation in the y-direction.

Additionally, in Figure 3-4(d)-(f), the product of the wavevector and transport mean free path (kl_t) for systems with different filling factors (FFs) and diameter of NW are shown. It can be seen that generally, l_t is much bigger for incident light in the z-direction (Figure 3-4(e)) than excitation in the y-direction (Figure 3-4(d)). This is because of two reasons: i) the value of scattering cross-section is generally smaller in this case even though Q_s is bigger because of the smaller shadow, A_p, of the particle in this setup (equation 1.5), ii) as shown in Figure 3-3, the scattering is less isotropic in this case, leading to a bigger value for g (equation 1.2). In Figure 3-4(c) and Figure 3-4(f), the average Q_s and kl_t values, where different source directions are taken into account are, plotted. As indicated by the red line in Figure 3-4(f), for λ_{source}=850

nm, the Ioffe-Regel criterion would be achieved for specific parameters, for example, when the NW diameter is around 140 nm and the array filling factor is around 0.3. We can also see if the NWs are too big or too small, this criterion could not be satisfied. As the diameter gets bigger, the scattering cross-section also increases, and at the same time, the anisotropy factor rises too. The increase of the scattering cross-section decreases the transport mean free path, and the rise of the anisotropy factor increases this length scale. Therefore, the localisation regime can only be satisfied at intermediate NW diameters.

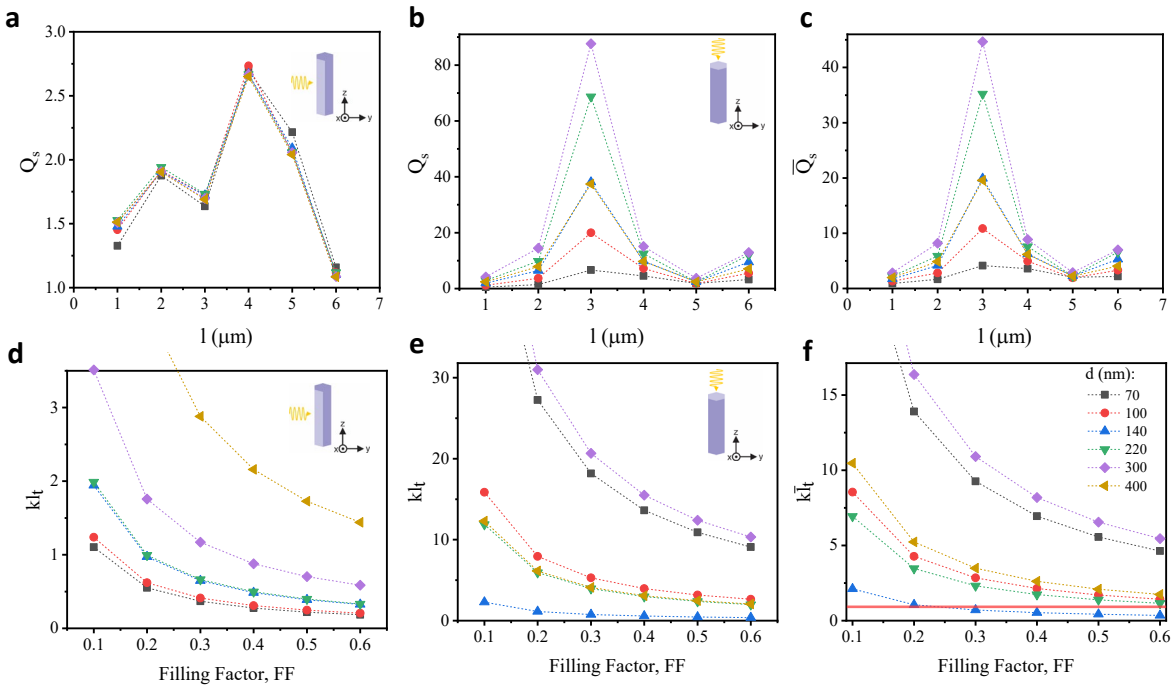

Figure 3-4: Calculated Qs as a function of NW length when the incident light direction is in the y-direction (a) and z-direction (b), and the average value of the two directions (c). Calculated kl_t as a function of filling factor when the incident light is in the y-direction (d) and z-direction (e), and the average value of the two directions (f). The red line indicates the Ioffe-Regel criterion is satisfied, assuming the NW length L=4 μm and λ_{source}=850 nm.

3.2.2 Quality factor analysis to determine the optimum filling factor and diameter

In RLs, two mechanisms contribute to the optical loss process: (i) internal absorption of the cavity, which can be taken into account via the imaginary part of the passive cavity index of refraction, (ii) out-coupling loss. In the first loss mechanism, energy is lost, usually as heat, in the laser cavity; however, in the second mechanism, light is uncoupled from the cavity to the non-active region, usually due to the cavity's low Q factor.

Specifically, in RLs, the primary loss mechanism is usually out-coupling loss, where the light leaves the active medium before the gain balances the loss. So, as discussed in chapter 1,

getting low threshold lasers with high Q factor cavities is essential. It is known that the formation of cavities with high *Q* values is related to the geometrical parameters of the system. For example, it has been shown that the size [100], *FF* [104, 105], density [29], and also the position [106] of the NWs can influence the scattering mean free path and hence the strength of light localisation and *Q* in RLs. For example, arrays with a low density of NWs would not support random lasing, and the scattering mean free path has to be optimised. In this section, the NW array's geometrical parameters are optimised to obtain cavities with high Q factors. For this purpose, a detailed 2D simulation is first performed to identify the possibility of getting cavities with high Q factors in systems with different average NW diameters (d_{av}) and FF.

3.2.2.1 Lateral confinement

For the simulation, Lumerical FDTD Solutions is used to solve Maxwell's curl equations. Considering the hexagonal xy cross-section of the grown NWs, randomly positioned hexagonal InP NWs are used. The random position of the NWs and different distances between the NWs would lead to around 15% variation in the diameters of the NWs. So, in the simulation, a uniform distribution between $0.85d_{av}$ and $1.15d_{av}$ is chosen for the NW diameters (Figure 3-5(a)).

As discussed in chapter 1, to introduce the randomness in the position of the NWs without the possibility of merging, a maximum deviation from the centre, $\sigma_{c,max}$, of 50 nm was chosen (so the deviation from the centre of the NW, σ_c, is between 0 and 50 nm) (Figure 3-5(b)).

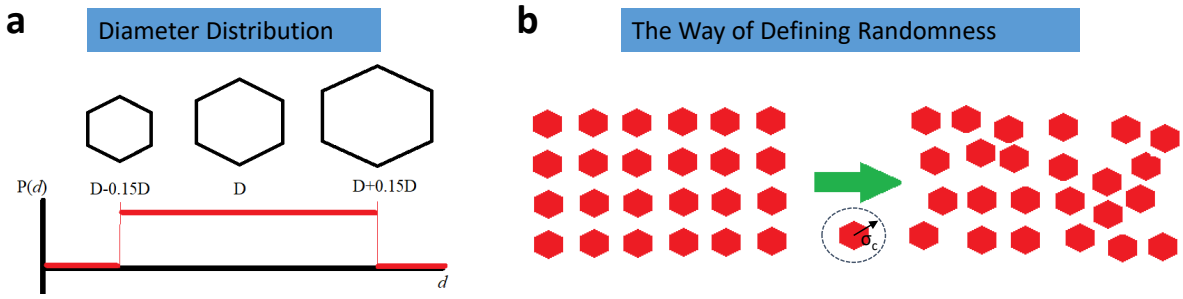

Figure 3-5: Definition of the random system. (a) Diameter distribution of our system assuming 15% variation in the diameter of the NWs. (b) The way of defining randomness by deviating randomly the positions of a periodic photonic crystal structure.

In the simulation setup, it is assumed the lateral size of the random media is 3 μm with perfectly matched layer (PML) boundary conditions. The effect of the lateral size of the disordered medium has been analyzed in chapter 4. It has been shown, considering the modes' sizes, 3 μm lateral size is big enough to support the modes. That is to say, the size of the simulation

area is chosen to be big enough so the system can support high Q factor cavities. If the area of the array is smaller than a certain value, leakage of the electromagnetic field would be too high, and the system would not be able to support high Q factor cavities. In the simulation, an electrical dipole source whose electric field is perpendicular to the page is used. Magnetic dipole source is also investigated but does not result in any cavity with high enough Q factors in the system. A refractive index of n= 3.456 for the InP NWs is chosen without the imaginary part, i.e. the NWs are assumed to be passive without any gain. It has been demonstrated in a passive medium with strong scattering, modes with high Q factors would be similar to the lasing modes in an active medium [49].

To optimise the average diameter of the NWs and the array FF, for each system with a particular d_{av} and FF, 10 cases with the same d_{av} and *FF* but with different positions of NWs are investigated. In this way, a statistical approach is carried out to investigate the random systems. In the inset of Figure 3-6(a), the schematic of a case with d_{av} =130 nm and FF=0.3 is shown. The red hexagons are the cross-section of the NWs where they are surrounded by air (light green region). Figure 3-6(b) is the spectrum of the cavities supported in this system, whilst the inset shows the magnified spectral region highlighted by the dotted box. It can be seen from this figure many modes with different Q factors and wavelength resonances, λ_r, could be supported in this system. Even modes with a very high Q factor of 18,300 (λ_r =796 nm) can be supported. The mode profile of the mode with the highest Q factor is shown in Figure 3-6(a).

Figure 3-6(c) shows the probability of finding Q factors higher than an arbitrarily defined threshold value (Q_t=3,000) with resonance wavelength near the NW bandgap energy (800 nm < λ_r < 850 nm). It can be seen that the system with FF=0.3 and d_{av}=120-130 nm has the highest probability of finding high Q factor cavities. This is also in good agreement with the calculations on transport mean free path above where Anderson localisation happens in NW array with diameters around 140 nm and *FF* of around 0.3 at the wavelength of 850 nm.

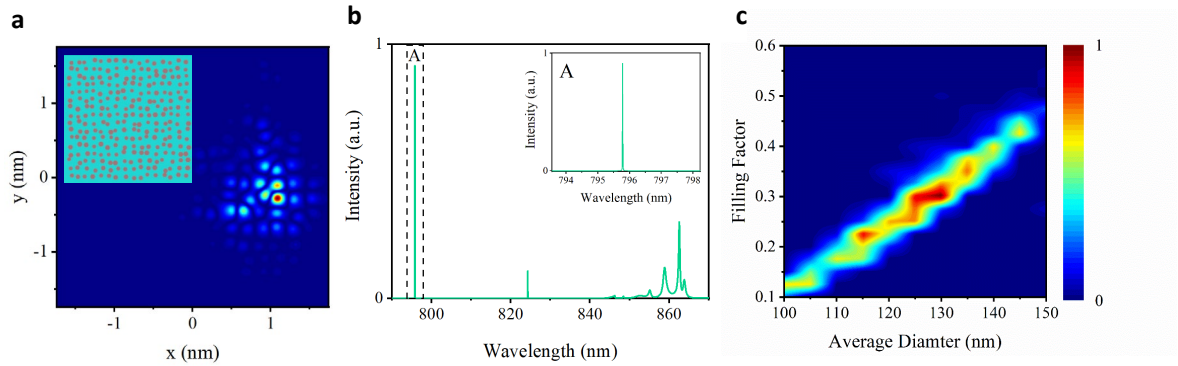

Figure 3-6: (a) Simulated 2D mode profile at the wavelength of 796 nm with a Q factor of 18,300 for a random case of a system with d_{av} =130 nm and FF=0.3. The structure of the random array is shown in the inset. (b) Resonance spectrum of the structure shown in the inset of Figure 3-6(a). The inset is the spectrum's magnified view around the mode's resonance wavelength with the highest Q factor. (c) The probability of finding Q factors higher than a threshold value (Q_t=3,000) in the wavelength region near the NW bandgap energy.

Using Lumerical FDTD Solutions, a 3D simulation is also carried out to investigate the cavities formed by the NW arrays. Based on the results from 2D analyses, the optimum value for *FF*=0.3 and d_{av}=125 are chosen for 3D simulation. The NWs have a length of *L*=3 μm and lateral array size of L_x= L_y=5 μm (*L* is the length of the NWs, L_x and L_y are the lateral sizes of the random system in x and y directions). The NWs are randomly positioned with $\sigma_{c,max}$=50 nm. In the simulation, the refractive index contrast created by the carrier generation and temperature contrast discussed in the next section has also been included.

The resonance spectrum and the lateral profiles of three modes (Mode I: *Q*=1,182, λ_r=829 nm; Mode II: *Q*=949, λ_r=791; and Mode III: *Q*=1,001, λ_r=848 nm) with the highest Q factors are presented in Figure 3-7. In the lateral profiles, the white dashed hexagons are the lateral cross-section of the InP NWs. It can be seen most of the mode is localised inside the NWs. Higher overlap of the modes with the NWs would lead to higher modal gain necessary for low threshold lasing.

It can be seen that even though Mode I and Mode II are spectrally uncoupled, they are spatially coupled. On the other hand, Mode III is both spectrally and spatially uncoupled to Mode I and II.

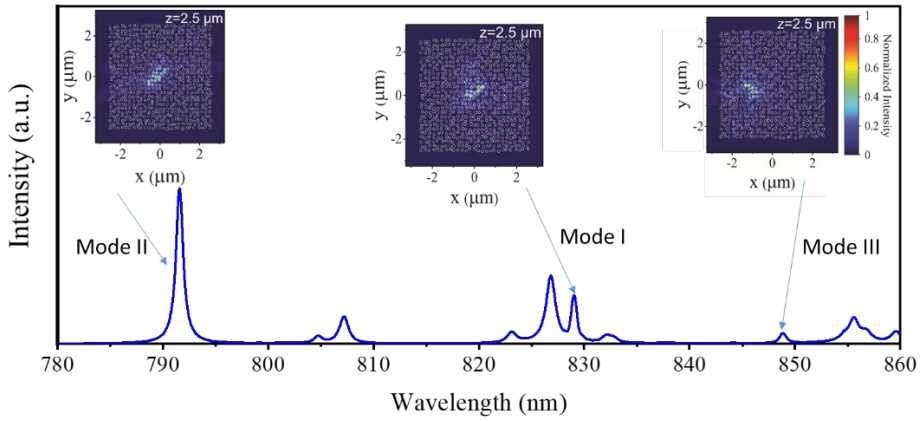

Figure 3-7: The resonance spectrum calculated for a system with *FF*=0.3, d_{av}=125 nm, and *L*=3 μm. The insets show the 2D spatial profiles for the three high Q factor modes (Mode I: λ_r=829 nm, Mode II: λ_r=791 nm, and Mode III: λ_r=848 nm) at a depth of 0.5 μm (i.e. at *z*=2.5 μm) from the tip of the nanowires (Figure 3-10), clearly showing strong localization in the x-y plane.

3.2.2.2 Vertical confinement

When a semiconductor is illuminated by light whose energy is larger than the bandgap energy, carriers are generated in the material. The optical generation rate is defined as the number of carriers created per unit volume per unit time. If each absorbed photon creates one electron-hole pair, the electron and hole generation rates are given by:

$$G_{p,op} = G_{n,op} = \frac{P_{abs}}{\hbar\omega}, \tag{3.1}$$

where P_{abs} is the number of absorbed photons per unit volume and can be calculated through

$$P_{abs} = -\frac{1}{2}\omega|E|^2\,\varepsilon'', \tag{3.2}$$

where ε" is the imaginary part of the permittivity. The carrier density can be calculated from the generation rate by multiplying the generation rate by the carrier lifetime. For example, for electrons, the following equation can be used:

$$N = G_{n,op}\tau_n \tag{3.3}.$$

To calculate the carrier generation, the previously designed random distribution of InP NWs (d_{av}=125 nm and *FF*=0.3) with the refractive index chosen at the excitation source wavelength (*n*=3.72+ 0.44i, λ_{ex}=522 nm) [98] is illuminated by a plane wave whose direction is parallel to the axial direction of the NWs (z-direction).

Figure 3-8 (a) and (b) show the optical generation and carrier density profile of the NW array under a pumping fluence of 1,200 μJ cm^{-2} per pulse, respectively. The array *FF*, d_{av}, length, *L*,

and lateral size (L_x=L_y) are 0.3, 125 nm, 3 μm, and 5 μm, respectively (same as the system used for cavity analysis). It can be seen the carrier generation occurs mainly at the top 300 nm of the NWs. Assuming a carrier lifetime of 1 ns [107], the carrier density profile along the z-direction, $N(z)$, is shown in Figure 3-8(b). The maximum carrier generation occurs at z=2.92 μm with N=1.16×10^{19} cm^{-3}. Considering a diffusion constant of 700 cm^2 V^{-1} s^{-1} [108], the diffusion length of the carriers is determined to be around 1.1 μm. Averaging $N(z)$ over the diffusion length, an average carrier density, N_{av} of ~2.1×10^{18} cm^{-3}, is obtained. Figure 3-8(c) shows the calculated average carrier density across the top 1.1 μm diffusion region for different pump fluences.

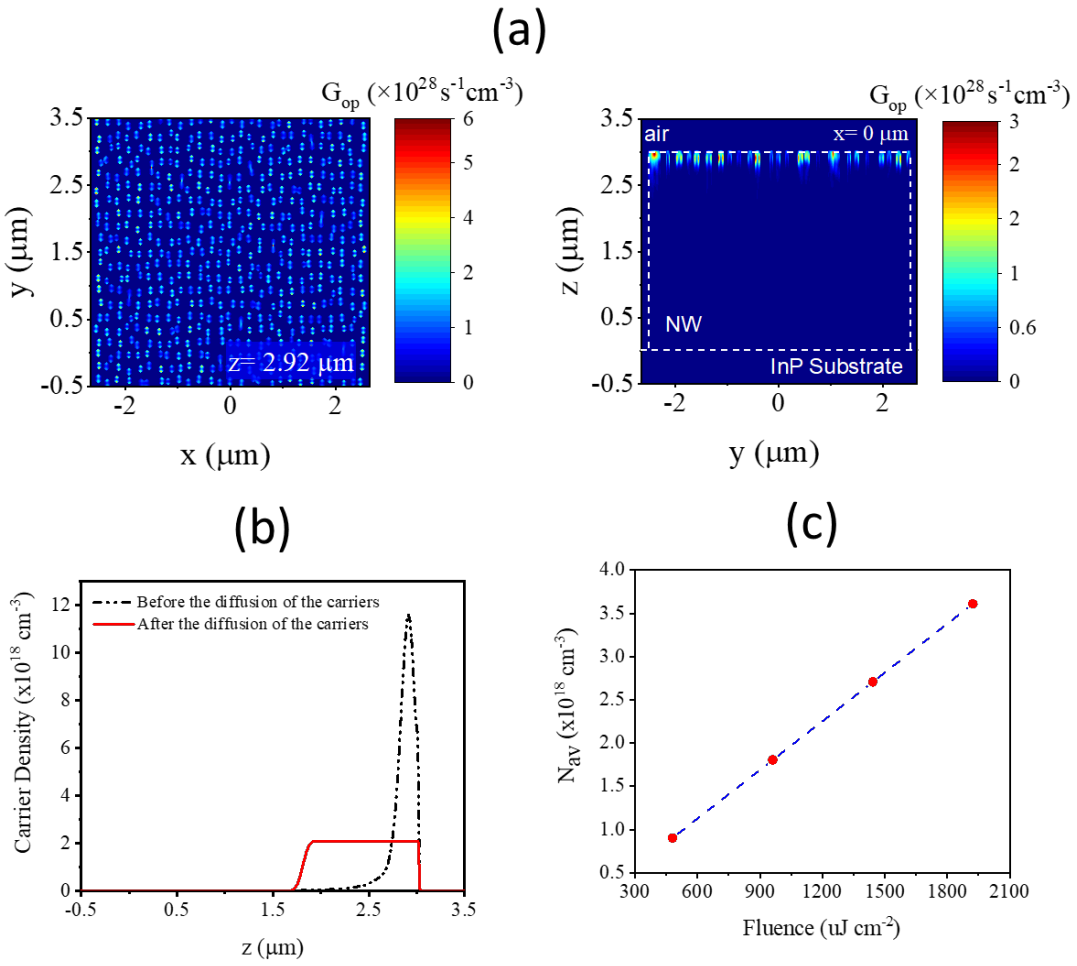

Figure 3-8: Modelling the optical generation and average carrier density of the random system under the pumping fluence of ~1,200 μJ cm^{-2} per pulse. (a) Optical generation from the NW array in x-y (left) and z-y (right) planes at z=2.92 μm and x= 0 μm, respectively. (b) Photo-generated carrier density profile along the NW length with and without the effect of carrier diffusion. (c) Calculated average carrier density in the top 1.1 μm of the NWs for different pump fluences.

Confinement factor and modal gain: After calculating the average carrier density, we calculate the modal gain and confinement factor using equations (1.17) and (1.18). For this purpose, the material gain is calculated using equations (1-10)-(1-15). First, the experimental PL emission is fitted with equation (1-16) to obtain the temperature and γ parameter. For this purpose, the PL spectrum of the NW array taken at a fluence of about 424 μJ cm^{-2} per pulse is fitted with equation (1-16) (Figure 3-9b). The parameters used for InP in equations (1-10)-(1-16) are summarised in Table 3-1.

Table 3-1: Material parameters for InP.

Parameter	**value**
m_e^* / m_0	0.08 [109]
m_{lh}^* / m_0	0.089 [109]
m_{hh}^* / m_0	0.6 [109]
E_P	20.7 [56]
E_g	$E_g = 1.421 - (4.9\times10^{-4})\frac{T^2}{T+327} + 0.08$ [110]
n_r	3.45 [111]

After fitting the PL emission with equation (1-16), T = 210 K and γ = 3 meV are obtained (for further details, see section 1.3.5.2). Then using equations (1.17) and (1.18), the material gain for different carrier densities are calculated and plotted in Figure 3-9(a).

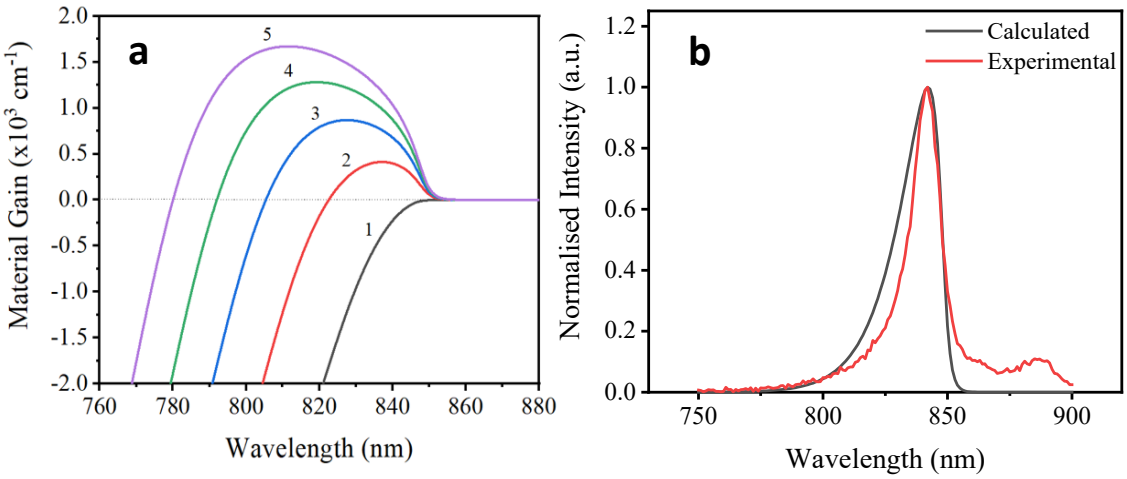

Figure 3-9: Calculated optical gain and normalised spontaneous emission intensity of InP. (a) The calculated optical gain for different carrier densities. The number labels next to the curves are in units of 10^{18} cm^{-3}. (b) Normalised spontaneous emission intensity emitted from the NWs at an excitation fluence of 424 μJ cm^{-2} (red) per pulse and the normalised calculated spontaneous emission intensity (black) for bulk InP with T = 210 K and γ = 3 meV.

After calculating the optical gain for different carrier densities, using the average carrier density at the top 1.1 μm of the NW at a particular pumping intensity (Figure 3-8) and considering the resonance wavelength of the mode of interest, the average gain at the tip of the NW can be obtained. For example, assuming a carrier density of 2.1×10^{18} cm^{-3} calculated previously, it can be seen for this value of carrier density, mode with resonances 820 nm < λ_r < 850 nm would have a positive average gain. Considering this average gain for the top 1.1 μm of the NW and zero gain for the rest of the system, equation (1.17) and equation (1.18) can be used to calculate the confinement factor and modal gain.

Refractive index contrast along the nanowire: The vertical confinement results from the change in the refractive index along the NWs' length as the carriers are generated at the top of the NWs. The NWs are excited by a pulsed laser from the top, with photo-generated carriers mainly within the top 300 nm of the NWs. Considering the effect of carrier diffusion, they will be primarily confined in the top 1.1 μm of the NWs [108] (Figure 3-8b). Furthermore, due to the increase in temperature [112] because of the thermal relaxation of carriers and the high density of photo-excited carriers [113], a change in the refractive index in this segment of the NWs is expected. That is to say, considering the average carrier density of 2.1×10^{18} cm^{-1} at a pump intensity of P_{in} =1,200 μJ cm^{-2} calculated before, and a temperature difference of ~200 K obtained from fitting the PL emission with equation (1.16), this region would experience a refractive index difference of ~0.087 compared to the rest of the NWs, resulting in mode confinement in the z-direction.

The 3D view of Mode I (from Figure 3-7) is shown in Figure 3-10. It can be seen that most of the mode is localised at the top 1.5 μm of the NW array leading to negligible leakage of the mode to the InP substrate (note that the tip of the NW corresponds to z=3 μm).

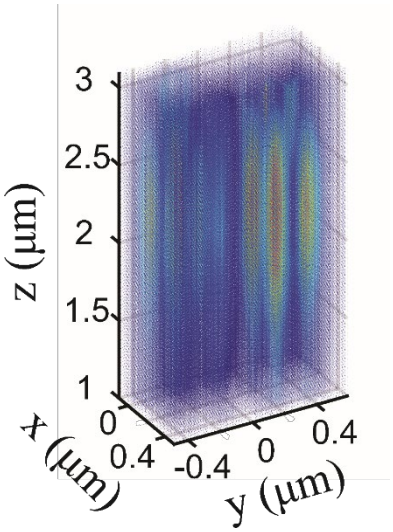

Figure 3-10: The 3D view of the simulated mode profile, where confinement can be observed in the vertical direction and confined predominantly in the NWs. The NW length is 3 μm, and the top of the NW corresponds to z=3 μm. Only the top 2 μm of the NW array is shown.

This refractive index contrast along the z-direction reduces the mode leakage to the substrate and enhances the localisation of the light leading to modes with higher Q factors.

To sum up, the lateral and 3D mode profiles shown in Figure 3-7and Figure 3-10 confirm the 3D localisation of light within the random NW array. It can be seen that the lateral confinement of the mode is due to the Anderson localisation, while the vertical confinement is due to the refractive index contrast along the NWs created by the carrier generation and pumping.

3.3 Samples preparation

To prepare the InP NWs, the SA-MOVPE method was used to grow the NWs. As discussed in detail in chapter 1, randomly positioned holes were patterned on the SiO_x substrate. To create the designed pattern, i.e. FF=0.3 and $d_{av}\simeq$125 nm, taking into account additional lateral growth, a random array of hole openings with a diameter of ~ 90 nm was patterned onto a 30 nm-SiO_x layer deposited on InP substrates as a growth mask. The randomly positioned holes were created as the way defined in the simulation section with $\sigma_{c,max}$=50 nm. After defining the holes on the SiO_x layer, using the MOVPE reactor and the following growth condition, the NWs were grown on the substrates. The details of substrate preparation and growth conditions used are discussed below.

Substrate preparation: Before growth, a standard preparation process [69, 114] for patterned substrates was used. Using plasma-enhanced chemical vapour deposition, ~30 nm-thick SiO_x was deposited on semi-insulating (111)A InP substrates as a mask, followed by electron beam lithography to create the randomly positioned holes on the resist. The pattern was then transferred to the SiO_x mask through dry etching using CHF_3 plasma. After removing the resist, the patterned substrate was trim-etched in 10 % H_3PO_4 to remove any native oxide layer[114] and then immediately loaded into the MOVPE system for nanowire growth.

Growth condition: In this work, a close-coupled showerhead reactor (Aixtron CCS 3 × 2) was used for the epitaxial growth. The reactor was operated at a low pressure of 100 mbar and used ultra-high purity H_2 as the carrier gas with a total flow of 10 $L.min^{-1}$. Trimethylindium (TMIn) and PH_3 were used as precursors for In and P, respectively. All substrates were first annealed in a PH_3 ambient at a surface temperature of 660 °C in the reactor. After a 10 min annealing step, the reactor was ramped up to a (wafer) surface temperature of 680 °C. Epitaxial growth was carried out by introducing TMIn into the chamber for 8 min. To reduce the possibility of NWs merging (i.e. to minimise radial growth), the molar flow of PH_3 and TMIn was 1.25×10^{-3} and 2.1×10^{-6} mol min^{-1}, respectively, leading to a high V/III ratio of ~595.

3.4 Structural characterisation

Figure 3-11(a) shows the SEM image of the grown InP NW array, whilst Figure 3-11(b) shows the statistical distribution of the NWs. It can be seen from the top-view SEM of the grown NWs the xy cross-section of the NWs is hexagonal. The average diameter of the NWs is around 116 nm with a standard deviation of ~13 nm (~12% diameter variation according to the average diameter). The *FF* of the fabricated system is ~ 0.25, which is quite close to the designed value. The size of the fabricated array was around 8 μm (L_x=L_y=8 μm).

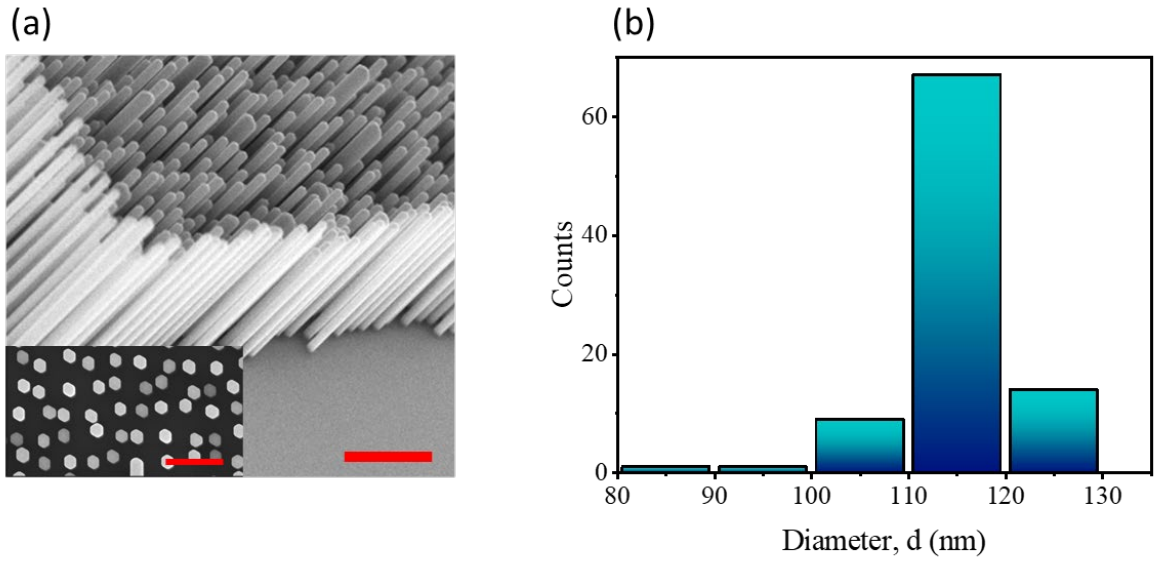

Figure 3-11: (a) SEM image showing a tilted view of the nanowire array (scale bar 1 μm). The inset shows a top view confirming the random nature of the nanowires in the x-y plane (scale bar 500 nm). (b) Diameter distribution of the NWs.

3.5 Optical characterisation

Measurement setup: For the photoluminescence (PL) measurements, a frequency-doubled pulsed laser (femtoTRAIN IC-Yb-2000, λ_{source} = 522 nm, repetition rate 20.8 MHz, pulse width 300 fs) with a Gaussian beam profile (FWHM~5 μm) was used to excite the random NWs through a long working distance objective lens (Nikon CFI Plan Fluor 60x/0.70 NA). The resulting emission was collected through the same lens and passed through a long-pass filter to remove the pump laser. Spectral measurements and near-field profiles were made using a grating spectrometer (Acton SpectraPro 2750) and a CCD camera (Princeton Instruments, PIXIS). As discussed in the section 2.5.1, for the spectral measurements a grating in the spectrometer was used to spread the collected light into a spectrum, which was then collected by the CCD camera. However, for obtaining the emission profile, a mirror was used to direct the collected light to the CCD camera without losing the spatial information of the emitted light from the sample. The schematic diagram of the micro-PL setup used for the optical characterization of the random nanowire systems is shown in Figure 2-7(b). Low-temperature experiments were conducted in a He-cooled cryostat (Janis ST-500).

3.5.1 Single-mode lasing

Figure 3-12 shows the low temperatures (6 K) PL spectra from the random array of the NW as a function of excitation fluence using the measurement setup mentioned above. The spectra are offset vertically for clarity. It can be seen at low pump fluence, a broad emission is

observed, and as the fluence is increased, the emission intensity increases with the broadening of the spectrum because of the band filling effect. At the pump fluence of ~550 μJ cm^{-2} per pulse, a shoulder appears at 843 nm. Increasing the intensity of the excitation fluence further increases the intensity of the shoulder peak, leading to a narrow lasing peak. The inset also shows PL spectral map indicating first a broadening of the spectrum with increasing fluence and a sudden narrowing after a threshold fluence is reached, an indication that the array is lasing.

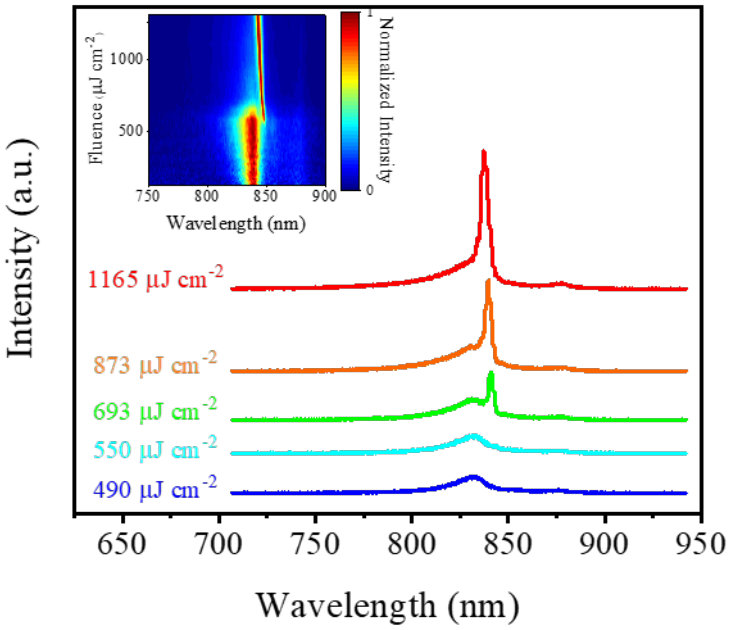

Figure 3-12: Emission spectra at 6 K from the nanowire array at various pump fluences. The normalised spectral map (inset) shows a broadening of the spectrum with increasing fluence up to the transition to the amplified spontaneous emission (550 μJ cm^{-2} per pulse) but then a sudden reduction in the linewidth above P_{in}=550 μJ cm^{-2} per pulse.

The PL spectra could be fitted with 3 Lorentzian functions as equation (3.4) below:

$$I = \frac{A_1}{2\pi}\frac{w_1}{(\lambda-\lambda_1)^2+(\frac{w_1}{2})^2}+\frac{A_2}{2\pi}\frac{w_2}{(\lambda-\lambda_2)^2+(\frac{w_2}{2})^2}+\frac{A_3}{2\pi}\frac{w_3}{(\lambda-\lambda_3)^2+(\frac{w_3}{2})^2}+d \qquad (3.4).$$

The PL spectra were fitted at two pumping intensities of P_{in}=490 μJ cm^{-2} per pulse (below the threshold) and P_{in}=693 μJ cm^{-2} per pulse (above the threshold), with the parameters summarised in Table 3-2: Fitting constants of equation (3.4) for fitting the PL spectra shown in Figure 3-13 for P_{in}=490 and 693 μJ cm^{-2} per pulse. Figure 3-13 shows both the experimental results and the fitted functions for the two spectra. Excellent fittings can be seen in both cases.

For the spectrum at P= 693 μJ cm^{-2} per pulse, the lasing peak and its FWHM are determined to be 841 nm and ~2 nm, respectively, resulting in a Q factor of 420.

Table 3-2: Fitting constants of equation (3.4) for fitting the PL spectra shown in Figure 3-13 for P_{in}=490 and 693 μJ cm^{-2} per pulse

P_{in} (μJ cm^{-2})	A_1	w_1	λ_1	A_2	w_2	λ_2	A_3	w_3	λ_3	d
490	1.21×10^4	21.79	830.2	-	-	-	803.01	13.02	874.7	2.964
693	1.68×10^4	24.72	829.8	3.19×10^3	2.27	841.2	604.13	8.1	876.6	1.597

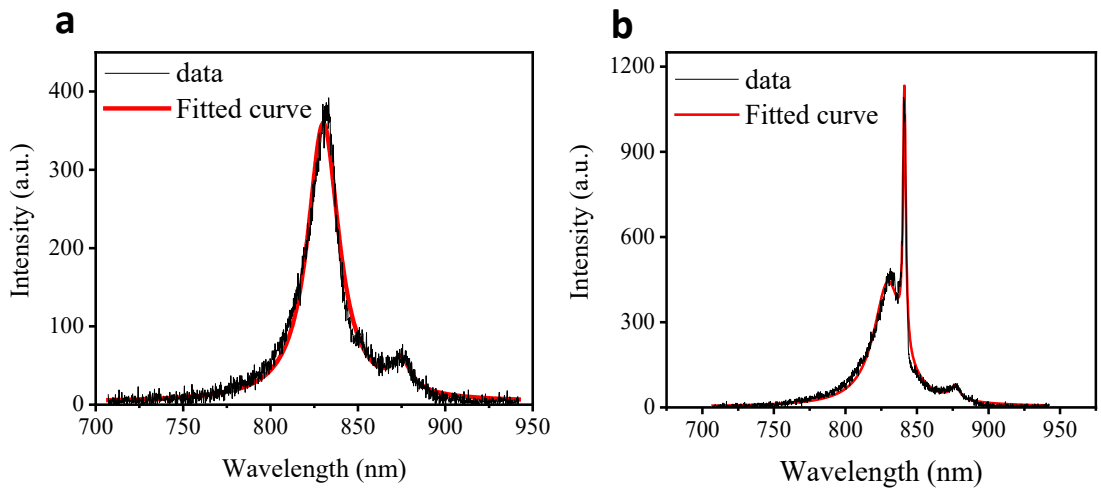

Figure 3-13: Fitting the PL spectra with equation (3.4) for two different pumping powers. (a) P_{in}=490 μJ cm^{-2} per pulse. (b) P_{in}=693 μJ cm^{-2} per pulse.

Figure 3-14: Light output vs. excitation fluence plotted on a log-log scale, showing an 'S-like' whilst the same data plotted on a linear scale (inset) shows a 'kink-like' threshold behaviour - indications of lasing from the nanowire array. The shaded grey area is the region of amplified spontaneous emission. The data points are the experimental results, and the red lines are just a guide to the eye. This figure shows that the power-dependent output intensity of the NW array on a log-log plot follows the typical "S"-curve shape where three emission regimes could be observed clearly. Spontaneous emission dominates at low excitation intensities until the transition to the amplified spontaneous emission at ~550 μJ cm^{-2} per pulse, followed by a super-linear increase indicative of amplified spontaneous emission (shaded grey region), and finally, the emergence of lasing above 733 μJ cm^{-2} per pulse [115-117]. A small emission with

a peak centred at ~879 nm can also be observed in the spectra, which correspond to emission from the underlying InP substrate (zincblende phase) [110].

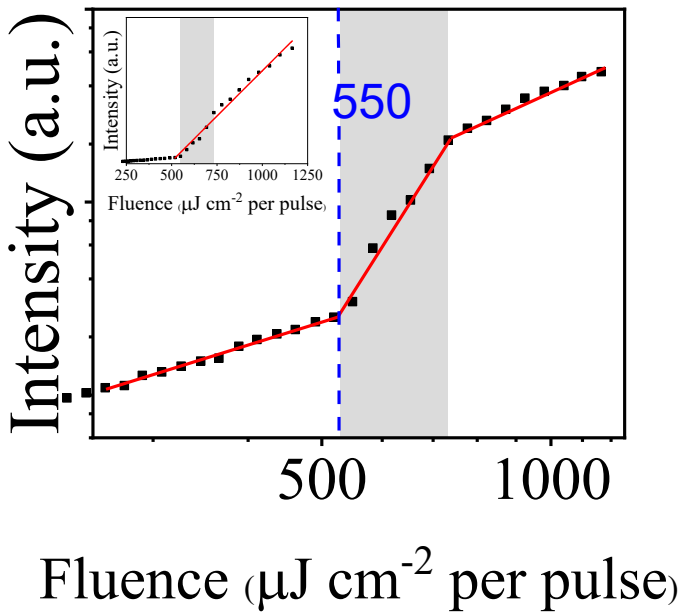

Figure 3-14: Light output vs. excitation fluence plotted on a log-log scale, showing an 'S-like' whilst the same data plotted on a linear scale (inset) shows a 'kink-like' threshold behaviour - indications of lasing from the nanowire array. The shaded grey area is the region of amplified spontaneous emission. The data points are the experimental results measured at T=6 K, and the red lines are just a guide to the eye.

3.5.2 Multi-mode lasing

Figure 3-15(a) shows the spectra of another random NW array with almost the same *FF* and d_{av} as the previously measured array but L_x=L_y=30 μm, at different excitation fluences, where multi-mode lasing is observed. At excitation fluence (P_{in}=386 μJ cm^{-2} per pulse) below the threshold, two broad peaks are observed, corresponding to the substrate (zincblende phase at 879 nm) and NWs (wurtzite phase at 832 nm) peaks, as discussed before. Similar to the array above, which shows single-mode lasing, the long-wavelength peak increases in intensity but remains broad with increasing input fluence, confirming lasing is not from the underlying InP substrate. On the other hand, for the NW emission, sharp peaks can be observed clearly in addition to a broad background above a fluence of 1,720 μJ cm^{-2} per pulse. It can be seen the number and intensity of these sharp peaks increase with excitation fluence. In other words, by increasing the excitation fluence, more modes can reach the threshold and the PL intensity of these modes increases. Figure 3-15(b) shows a log-log plot of three L−L curves corresponding to the wavelength region I (769 < λ < 787 nm), region II (787 < λ < 807 nm), and the total spectrum of the NW region (725 < λ < 850 nm) for comparison. The onset of amplified spontaneous emission for the modes in regions I and II occur at ~1,720 and ~1,937

μJ cm^{-2} per pulse, respectively. The power intensity at which this transition has happened for the entire spectral region of the NWs is almost similar to the value of the mode in region II. This is because emission from region II is much higher than that from region I, and therefore a higher excitation fluence is required for the latter region to achieve lasing.

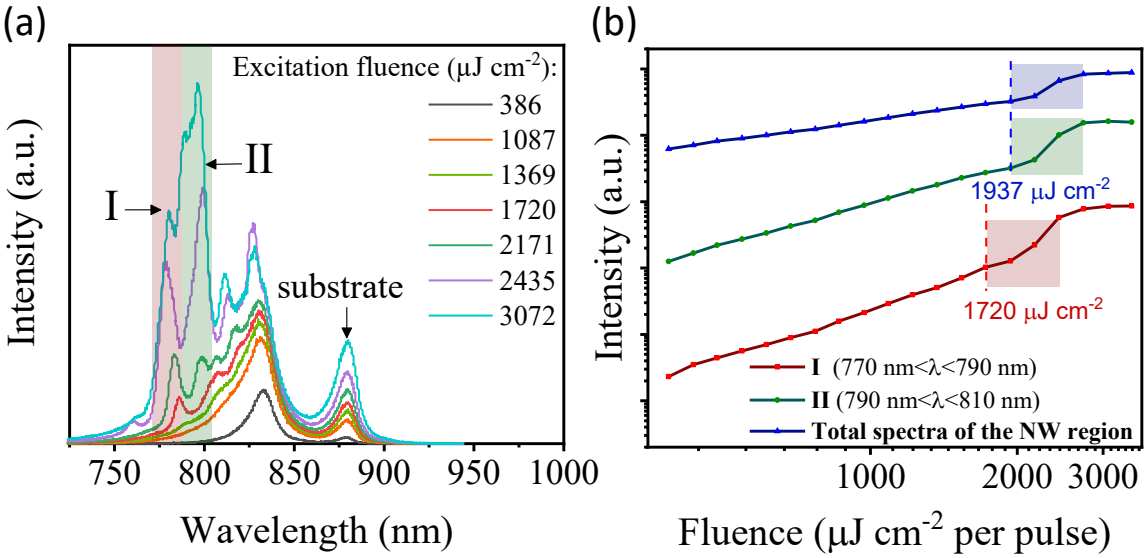

Figure 3-15: Multi-mode lasing from the random nanowire array. (a) Emission spectra from the nanowire array at various pump fluences. Emission from the substrate is indicated, whilst emission from the nanowires occurs below 850 nm. (b) Log-log plot of integrated light output vs fluence from two spectral regions shown in (a): shaded red region I (769 < λ < 787 nm) and green region II (787 < λ <807 nm). The results for total light output from the nanowire array (725 < λ < 850 nm) are also shown for reference. All measurements were done at 6 K.

In Figure 3-16, the near-field emission profiles as viewed from the top of the NWs at different pumping intensities corresponding to the PL spectra in Figure 3-15 are shown. A broad profile is observed at low pump fluence, but as the fluence gradually increases, spatially localised peaks appear above the broad Gaussian-like emission profile. Line scans across the profile in various directions confirm this observation. At P_{in}=2,435 μJ cm^{-2} per pulse, three high-intensity spots appear, which can be correlated to the three predominant modes at λ=788, 799, and 826 nm in Figure 3-15(a). Increasing the pump fluence further to P_{in}=3,072 μJ cm^{-2} per pulse leads to the lasing mode at 799 nm becoming more dominant.

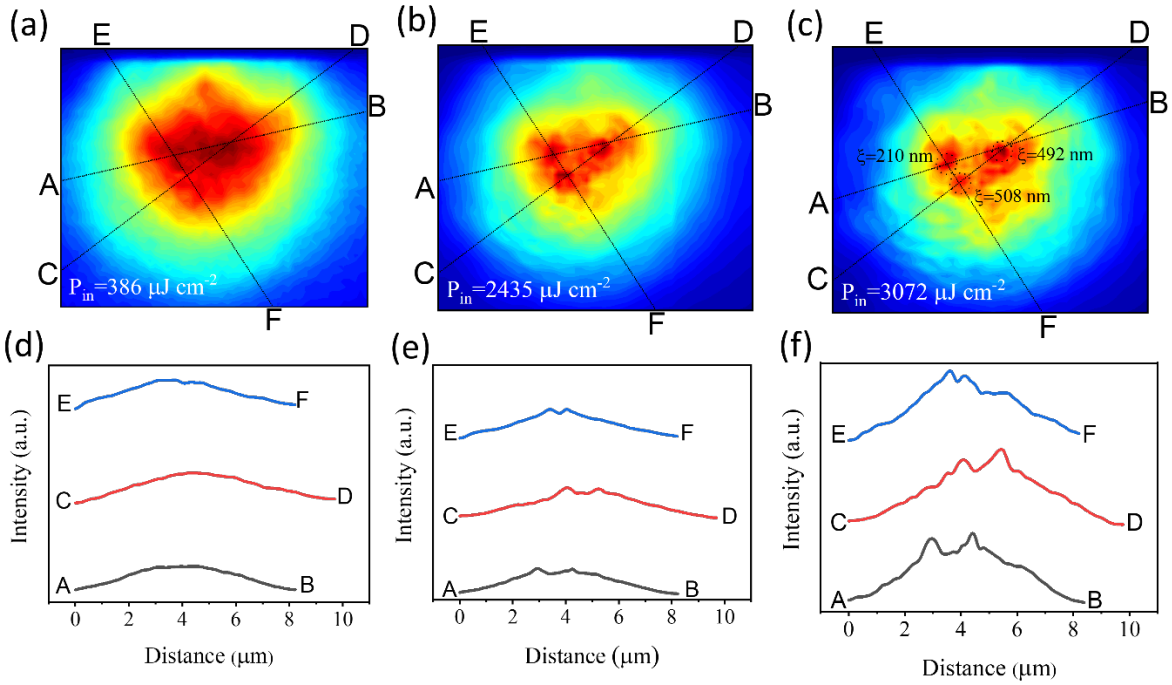

Figure 3-16: Near-field emission profiles from the nanowire array at three different excitation fluences: (a) P_{in}=386 μJ cm^{-2} per pulse, (b) P_{in}=2,435 μJ cm^{-2} per pulse, and (c) P_{in}=3,072 μJ cm^{-2} per pulse. Corresponding line scan across the near field intensity profiles in (a), (b), and (c) along three directions, AB, CD, and EF are shown in (d), (e) and (f). The cross-section mode profiles indicate strong localisation above the lasing threshold as indicated in (e) and (f). The calculated localisation lengths for the mode are indicated in the image (g). All measurements were done at 6 K.

Random cavities decay exponentially [48] with an average characteristic length known as the localisation length, ξ. To calculate the localisation length, each of the three peaks in Figure 3-16 is fitted with an exponential function along the two lines connecting the mode to the other two modes. For example, consider the cross-section mode profile along the AB direction shown in Figure 3-17. The two peaks have been fitted with exponential functions leading to localisation lengths of 248 and 274 nm. Besides, this figure shows the localisation length of these two modes along the AB line is smaller than the distance between these two modes (i.e. 274 nm + 248 nm < 1450 nm). This means that the modes are spatially decoupled.

For each mode, we obtain two localisation lengths along each connecting line. One localisation length is on the left-hand side of the mode, and the other one is on the right-hand side of the mode. Since two lines are connecting each mode to the other two modes, we have four localisation lengths for each mode in different directions. The localisation lengths are shown in Figure 3-16(c) (ξ= 210, 492, and 508 nm) are the average value of these four localization lengths for each mode along different directions.

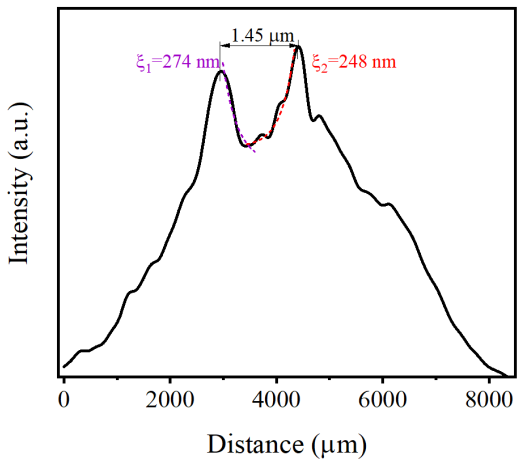

Figure 3-17: Fitting the two peaks on the AB line with an exponential function of $y=A\exp(-x/\xi)+B$ to calculate the localisation length for the two modes.

The number of nanowires in which the mode is localised, N_{NW}, can be calculated through $N_{NW}=\pi\xi^2$. FF/A_{av}, where A_{av} is the average cross-sectional area of the NW. This results in around 4, 20, and 22 NWs interacting with each of the three localised modes, respectively. Since ξ is much smaller in size than the area of the active scattering region (which is approximately the pumped area whose FWHM is around 5 μm), this confirms the Anderson localisation effect in these NW arrays. Besides, as shown in Figure 3-16 and Figure 3-17, the modes are spatially isolated, i.e. the distance between the modes is higher than the sum of the localisation length of the modes along the lines connecting them. These features are consistent with the theoretical prediction for multi-mode random lasing in the Anderson localisation regime [118]. On the other hand, in diffusive RLs, the lasing wavelength is primarily determined by the spectral peak of the gain medium [98], and only weak dispersion is incorporated into the scattering medium, resulting in a significantly broader lasing peak. Here in our case where localisation occurs, lasing modes even at wavelengths in the lower part of the gain spectrum (758 and 778 nm) can also be observed, which agrees with the random lasing in the localisation regime [93].

3.6 Stability of the lasing modes

Unlike RLs operating in the diffusive regime, where the single-shot emission spectrum is unstable and changes from shot to shot [119], in our random NW system, the spectrum is stable under successive pulsed excitation, as shown in Figure 3-18. This figure shows how different modes evolve with increasing excitation fluence over numerous pulses for two different locations on the sample. ΔN_{pulse} at a particular excitation fluence is defined as the difference between the number of pulses at that excitation fluence and the lowest excitation fluence. For example, $\Delta N_{pulse}=375\times10^6$ at P_{in}=2,258 μJ cm^{-2} per pulse in Figure 3-18(a) means

the NW array has been subjected to an additional 375×10^6 pulses after recording the spectrum at P_{in}=386 μJ cm^{-2} per pulse. It can be seen at both locations whose spectra are shown in Figure 3-18(a) and Figure 3-18(b), even though lots of pulses have excited the sample, the modes are stable and well defined even with increasing the excitation fluence with only a small blue shift due to changes in refractive index with increased carrier density and temperature [120, 121].

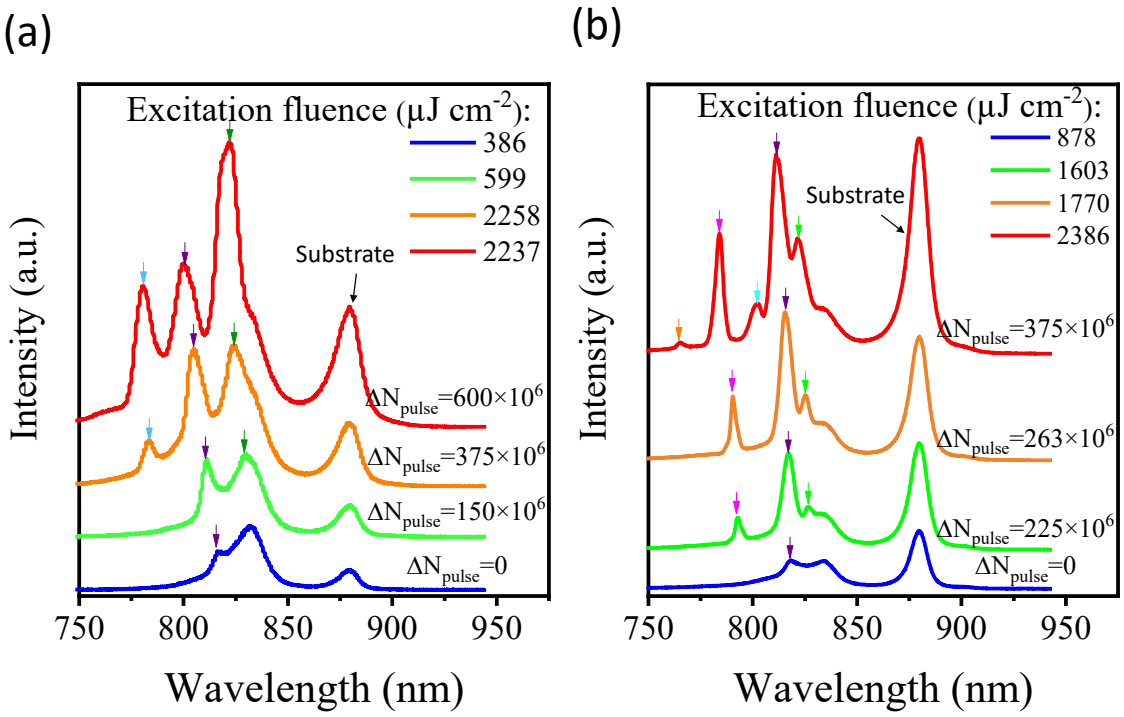

Figure 3-18: Lasing stability. Emission spectra at different excitation fluences from two different regions of the random nanowire array which support 3 (a) and 5 (b) lasing modes. With increasing fluences, the nanowire array has been subjected to more excitation pulses. The difference in the total number of pulses used to collect each spectrum from those used for the lowest fluence is indicated by ΔN_{pulse}. All measurements were done at 6 K.

3.7 Statistical distribution of several lasing parameters

Figure 3-19 shows the statistical distribution of several key parameters of the fabricated NW RL. In Figure 3-19(a), the pump intensities at the onset of amplified spontaneous emission show an almost normal distribution, with most of the modes having pump intensities between 1,500-2,000 μJ cm^{-2} per pulse. As discussed previously, by calculating the optical gain for different carrier densities (Figure 3-9), it is found that at P_{in}=2,000 μJ cm^{-2} per pulse, positive gain is achieved for modes in the wavelength range of 790 - 850 nm. Figure 3-19(b) shows the distribution of the experimental quality factor of the resonant cavities. The distribution of simulated Q factors for different modes and their correlation with the mode confinement factor

and lateral size are presented in Figure 3-20. The highest value for the calculated and measured Q factor are 1,181 and 420, respectively. The median Q factor and wavelength resonance are $Q_{m,exp}$=165, $\lambda_{m,exp}$=790 nm, and $Q_{m,sim}$=380 and $\lambda_{m,sim}$=819 nm for the experimental and simulated results, respectively.

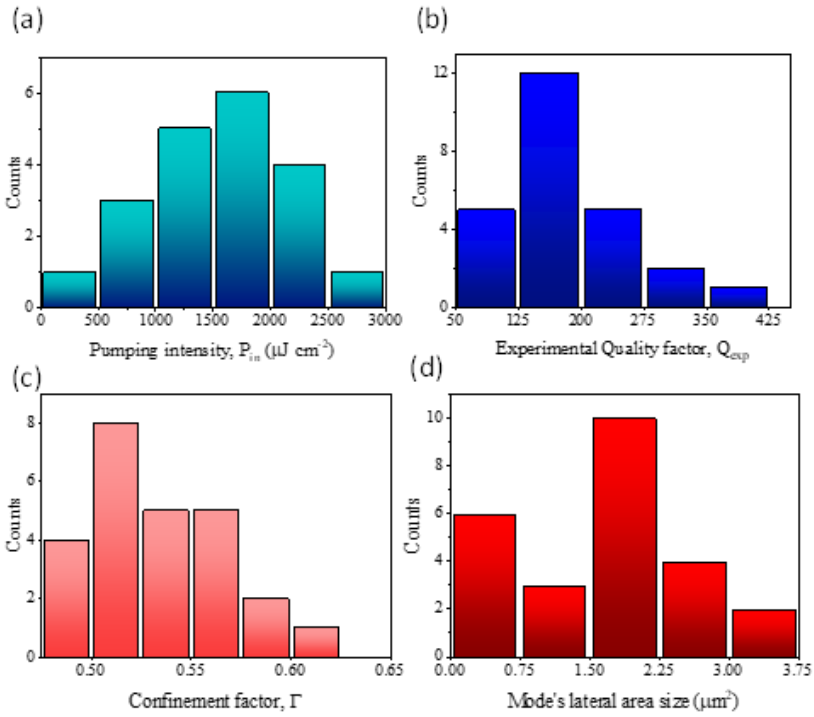

Figure 3-19: Statistical distribution of several key parameters of the random nanowire laser. (a) Measured pumping intensity distribution taken at the commencement of amplified spontaneous emission. (b) Experimentally measured Q factor of the modes. (c) Calculated distribution of the mode confinement factor. (d) Calculated distribution of the spatial lateral mode size.

Figure 3-19(c) shows that our system's calculated mode confinement factor is usually more than 0.5, and some modes even have confinement factor values as high as 0.62. Although these values are lower than in conventional nanowire lasers operating in the Fabry-Pérot mode [122, 123], they are higher than those expected for those operating in the diffusive regime. In the diffusive regime, the lower Q factor leads to more leakage of the field from the NWs and consequently lower confinement factors. The correlation between the Q factor and Γ is quantified by Spearman's rank correlation coefficients, r_s, and is around 0.61, which shows a good correlation between these two parameters, where modes with lower Q factors usually show less localisation (Figure 3-20(c)). For example, in our simulation results, a mode with Q=568 has a Γ=0.62; however, another mode with Q=188 shows only a confinement factor of 0.48.

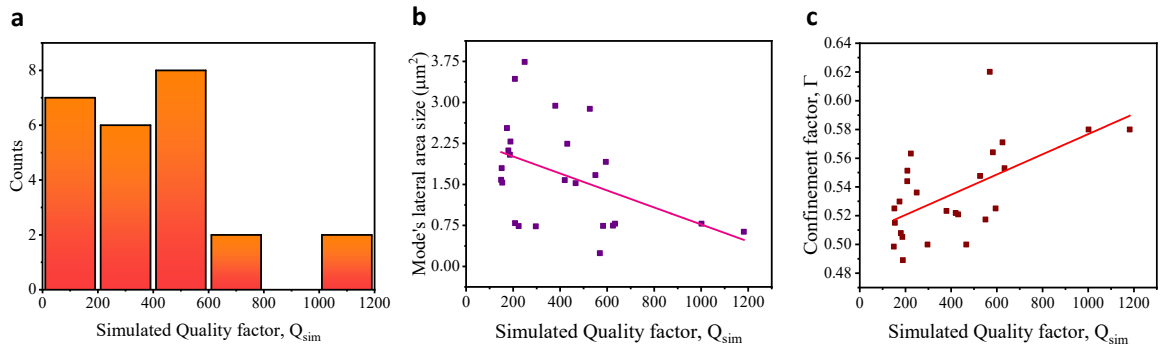

Figure 3-20: Correlation between Q factor and other mode parameters. (a) Statistical distribution of the simulated Q factor. Calculated Q factors versus (b) the lateral sizes and (c) the confinement factors of the modes. The Spearman's rank correlation coefficients is r_s=-0.45 (b) and 0.61 (c). The pink and red lines are fitted to the data.

Figure 3-19(d) shows the calculated size distribution of the lateral mode. The average, minimum and maximum values for the lateral mode area are 1.67 (~29$(n/\lambda_{av})^2$), 0.24 (~4.7$(n/\lambda)^2$), and 3.74 μm^2 (~62$(n/\lambda)^2$), respectively. Considering these values, the smallest and the largest modes encompass 4 and 91 NWs, respectively. Besides, as shown in Figure 3-20(b), the poor correlation of r_s= -0.45 between the Q factor and lateral mode size indicates that a high Q factor does not necessarily lead to smaller modes. Indeed, high Q factor modes could involve scattering between more NWs than a mode with a lower Q factor.

3.8 Conclusion

RLs can occur due to multiple scattering events within a gain medium, which provides the equivalent feedback mechanism. The unique feature of RLs such as angular free emission, tunability of lasing direction, low spatial coherence with high photon degeneracy, large area lasing, lasing from flexible substrates, facile fabrication methods and lower cost, make them of great interest for various applications such as in speckle-free laser imaging and display technologies. However, because of the difficulty of localising and controlling the lasing modes, the devices are spectrally less stable and have hindered applications where stable broadband wavelength-controlled lasers over large areal sizes are required.

In this chapter, we demonstrated that our designed InP random nanowire arrays could provide the gain required for lasing and strongly confine light spatially in 3D. We have designed and experimentally demonstrated that Anderson localisation in RLs could be achieved by using InP random NW arrays due to their high gain and strong scattering properties. Light is confined in a 3D mode, where the lateral confinement is provided by scattering whilst vertical confinement is provided by refractive index contrast. The near-field images of the mode profiles show exponential decay of the localised modes. The strong spatial confinement of the modes results

in the stable multi-mode operation of RLs. Mode control in RLs opens up new opportunities for the facile fabrication of lasers over large areas (10s-100s μm^2) for application in the next generation meta-optical systems.

Chapter 4: Controlling the lasing modes in the localisation regime

4.1 Introduction

As discussed in previous chapters, RLs, due to their mirrorless cavities, could have some unique properties which are not seen in lasers with traditional cavities. For example, RLs do not have the complexities associated with fabricating and designing mirror-based cavities, such as Fabry-Pérot ones. Furthermore, due to the nature of the cavities in RLs, angle-unrestricted emission could be achieved. The mirrorless cavities in RLs could provide large area, tunable, and mechanically flexible lasers. On the other hand, the random scattering of light and the nature of the modes in RLs make them difficult to be controlled. For example, as discussed in chapter 3, in diffusive RLs, the emission spectrum changes from shot-to-shot due to the delocalisation of the modes. There we demonstrated that by designing the RL geometrical parameters, it is possible to make the transport mean free path smaller than the wavelength for the RL to operate in the localisation regime. Therefore, making the RLs perform in the Anderson localisation regime would make it easier to control the lasing mode properties such as wavelength resonances, lasing threshold and number of modes.

To control the lasing behaviour of the RLs, different methods have been proposed. Here, some of these methods are briefly discussed.

Changing the gain material: As discussed before, two main conditions need to be satisfied to achieve random lasing: (i) multiple scattering of the light path, (ii) the presence of gain to amplify the scattered light. The scatterers could also act as the gain medium in RLs, such as the InP NWs discussed in chapter 3. On the other hand, it is also possible to separate the gain and scattering media. This would give more freedom to control the lasing properties because now both scatterers and gain media could be separately engineered. For example, Ziegler et al. demonstrated that using different dyes with different emissions as the gain media (such as rhodamine 6G, rhodamine 800, styryl 14, etc.) with gold nanostars (acting as the scatterers), random lasing throughout the visible up to the infrared range [124], could be achieved.

Using multiple gain media: Wang et al. showed that by using R6G–oxazine mixed binary dye (where the absorption band of oxazine partially overlaps with the emission band of R6G) and the suspension of gold–silver porous nanowires with plenty of nanogaps (with broadband plasmonic resonance) simultaneous multi-coloured coherent random lasing through single

excitation could be achieved. The lasing wavelengths of ~570-580 nm and ~630-640 corresponding to the emissions of R6G and oxazine were achieved, respectively [125].

Changing the pumping properties: It was shown by changing the spatial intensity profile of the light with a spatial light modulator (SLM), single-mode lasing at any particular wavelength within the spectrum of the gain medium can be achieved [126]. The scattering medium used for this study was a one-dimensional (1D) disordered random distribution of rectangular pillars, and a spectral selectivity down to 0.06 nm was achieved.

In another work, Leonetti et al. have shown that changing the pumping shape from a disc shape to a stripe shape makes it possible to move from a system with non-resonant feedback to a resonant one[127].

Using materials sensitive to external sources: If the material of the RL is sensitive to temperature, magnetic field, applied voltage, etc., it may be possible to change these parameters in order to change the properties of the medium and behaviour of the RL. For example, a liquid crystal (LC) diffusion constant could show an abrupt increase around the nematic–isotropic phase-transition temperature. This could enable the operation of the RL above and below its threshold by temperature-tuning of the diffusion constant. Using these properties [128] of LCs, a temperature-tunable RL was demonstrated. Using the temperature dependence of refractive indices of LC, polarization-dependent temperature tuning of the resonance wavelength was also demonstrated [129]. In that work, below 34°C, both lasing modes corresponding to the ordinary (λ_o) and extraordinary light (λ_e) polarisation were observed. However, as the temperature was raised above 34°C, the birefringence property of the LC disappeared, and both λ_o and λ_e converged to a single wavelength.

Applying a voltage could also change the emission properties of the RLs. For example, it was shown that by inducing an external voltage on LC-based RLs, the molecule direction of LCs can be changed, leading to a blueshift in the emission wavelength [130].

These reports show that changing the temperature and external voltage can change the RLs behaviour; however, most reported studies show that the rise in temperature or increase in applied voltage would decrease the emission intensity, which can severely impact practical application [131].

In another study, Naruta et al. have shown that using ferromagnetic nematic liquid crystals (FNLCs), it is possible to change the intensity of the RL by an external magnetic field [132]. FNLC is obtained by dispersing ferromagnetic nanoplatelets (MNPs) in nematic liquid crystals

(NLCs). In MNPs, the spontaneous magnetisation is normal to the plate surface, and due to the interaction between the plate surface and the nematic director, *n*, (The orientation of the long axis of a nematic molecule is called its nematic director.) in the FNLCs, MNPs are oriented in the same direction as the NLCs. Therefore, *n* of FNLCs can be reoriented by extremely weak magnetic fields owing to the coupling between magnetisation and n.

Changing scatterers geometry and structure: Gottardo et al. showed that by exploiting the resonances in scattering coefficients, known as Mie resonances, it is possible to tune the non-resonant lasing wavelength [133]. In this work, the diameter of the monodisperse spheres was modified to tune the lasing wavelength. To create the Mie resonances, the sizes of the scatterers were made comparable to the wavelength of the scattered light. Using a photonic crystal structure with a transport mean free path, l_t, of 2-3 μm almost five times bigger than their lasing wavelength, they managed to operate their lasing at the diffusive regime [93]. By changing the diameter of the scatterers, the lasing wavelengths were tuned from 600 to 640 nm.

In chapter 3, we have shown that by designing the random system made up of InP nanowires, localised multi-mode lasing could be achieved. There we have demonstrated by changing the diameter and density of scatterers, it is possible to increase the probability of achieving high-quality factor (QF) cavities in the desired wavelength region. By changing the diameter and filling factor of the system, it is possible to change the scattering efficiency of the system and make it stronger for particular wavelengths. In this chapter, it has been shown how it is possible to tune the resonant wavelengths by changing the various geometrical parameters. For example, by decreasing the average diameter, *d*, of the NWs, a blueshift of the average wavelength resonance is reported.

Moreover, the effects of other geometrical parameters, including randomness degree, nanowire length, *L*, and lateral system size on the lasing behaviour, are analysed. For example, it is shown that the NW length should be bigger than the diffusion length of the InP NW to reduce mode leakage into the substrate. Besides, by decreasing the lateral size of the system, it is possible to manage the number of lasing modes, and even single-mode lasing could be achieved.

4.2 Managing the lasing parameters of the random lasers

In this chapter, we show how it is possible to manage different lasing parameters such as wavelength resonance of the modes, λ_r, number of the modes and lasing threshold by changing the different geometrical parameters of the InP NW RLs.

4.2.1 Effect of density and size of the scatterers

As discussed in chapter 3, random lasing can occur when the gain is large enough to balance the loss mechanisms and the sample size is larger than the diffusive critical volume, or in other words, the sample size is bigger than l_t [3]. RLs have two main loss mechanisms: (I) out-coupling loss to the surrounding media, (II) internal absorption loss. To quantify the first mechanism, the passive system's quality factor, *Q*, can be used. However, the second mechanism is mainly due to material loss because of lower carrier generation inside the cavity.

Figure 4-1 shows the effect of *FF* and NW average diameter, d_{av} on the carrier generation and Q of the supported cavities in random NW systems. The inset of Figure 4-1a shows the optical carrier generation, G_{op} of a randomly distributed InP NWs (n=3.73+i0.446, where *n* is the refractive index on InP at the excitation wavelength) with *FF* = 0.3, d_{av} = 125 nm, and length, *L* = 3 μm. As for the excitation source, we assume a 522 nm laser similar to that used in the experimental setup discussed in chapter 3. The pumping intensity of the plane wave source was chosen to be 10^4 Wcm^{-2}. Carriers are mainly generated at the top 0.3-1 μm of the NWs, depending on the diameter of the NWs and *FF* of the system, as shown in Figure 4-1a. The average carrier density at different slices along the NW axis (along the xy-plane) is obtained through:

$$N_{av}(z) = \tau_c \iint G_{op}(x,y)dxdy \tag{4.1}$$

where τ_c is the carrier lifetime and is assumed to be 1 ns [107]. It can be seen decreasing the *FF* spreads the carrier generation profile deeper into the NWs. However, decreasing the diameter of the NW decreases the maximum generation and increases the generation depth. Calculating the average carrier density over the top 1 μm of the NWs (which is around the diffusion length of the carriers in InP) for the three systems, we obtain values between 2.3×10^{17}- 2.6×10^{17} cm^{-3} for the three systems, indicating that the average carrier density in the three systems is almost the same over the top ~1 μm. However, the system with higher *FF* has nearly three times higher carrier density inside the gain media (inside the NWs), leading to higher photon generation and a lower lasing threshold. This shows, to obtain gain at a lower pumping threshold, systems with a higher density of NWs are preferred (i.e. higher *FF*).

In Figure 4-1b and 4.1c, the probability of finding Q_s higher than an arbitrary threshold value of Q_t = 3000 with resonance wavelength, λ_r near the NW bandgap energy of 725 nm < λ_r < 775 nm (Figure 4-1b) and 800 nm < λ_r < 850 nm (Figure 4-1c) are plotted as a function of *FF* and d_{av}. For analysing each distribution of nanowires with particular d_{av} and *FF*, a statistical approach, similar to the one discussed in chapter 3, based on a 2D simulation, was used.

Therefore, for each system with a particular *FF* and d_{av}, ten different distributions were analysed. It is further assumed the 2D systems have the same lateral size of 3 μm in x and y directions (L_x = L_y = 3 μm where L_x and L_y are the lateral size of the system in the x- and y-direction, respectively). It will be shown and discussed later these lateral sizes for L_x, and L_y are bigger than the mode size, and therefore the modes are properly supported in the system with low leakage.

The randomness of the NW position distribution was defined similarly to the way it was described in chapter 3 (Figure 3-5), and σ_c was varied between 0 and 50 nm ($\sigma_{c,max}$=50 nm). To consider the non-uniformity of the grown NWs (Figure 3-11b), it was assumed the NWs have a 15% variation in diameter. As for the excitation source, an electrical dipole source with an electric field along the NW axis (z-direction) was used. The system was assumed to be passive, i.e. a system without gain, and the NWs were InP with a refractive index of n = 3.456. It can be seen from Figure 4-1b at the higher wavelength range, arrays with *FF* = 0.2-0.3 and d_{av} = 118-130 nm have the highest probability of finding high Q cavities. However, as shown in Figure 4-1c, arrays with *FF* = 0.2-0.3 and d_{av} = 105-120 nm have the highest probability of finding high Q cavities for the lower wavelength range. The results show that to tune the emission of the random nanowire lasers to a lower wavelength, a smaller d_{av} is generally required.

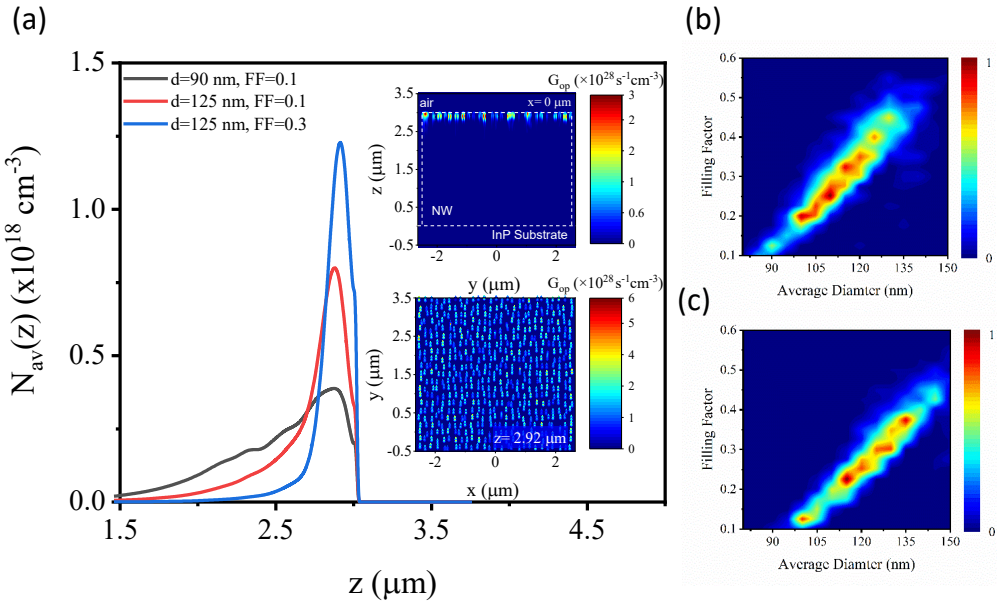

Figure 4-1: The effect of d_{av} and *FF* on the designed random system. (a) Average carrier density along the nanowire length for systems with different average diameters and *FF*s. The inset shows the optical carrier generation at zy (top inset) and xy (bottom inset) planes. (b,c) Probability of finding high *Q* (*Q* > 3000) for systems with different *FF* and average diameters, for 725 nm < λ_r < 775 nm (b) and 800 nm < λ_r < 850 nm (c).

Using the same 2D simulation setup used for Figure 4-1, the effect of increasing d_{av} on Q and λ_r of the cavities is shown in Figure 4-2a and Figure 4-2b, respectively. By increasing d_{av} of the NW, a redshift to the resonance wavelength is observed. Besides, in systems with a smaller NW diameter, the number of modes with $Q > 3000$ is higher, and the number of modes decreases as the diameter increases. As d_{av} of the NW decreases, keeping *FF* constant, the number of scatterers increases, leading to higher scattering events. Therefore the number of cavities also increases.

The effects of increasing *FF* on *Q* and λ_r of the cavities are depicted in Figure 4-2c and Figure 4-2d. It can be seen that increasing *FF* of the arrays would result in a blueshift of the resonance wavelength. Besides, in arrays with lower *FF*, the number of modes is low, and as *FF* increases, the number of the modes and especially the possibility of getting low *Q* modes decreases. Similar to the effect of decreasing d_{av}, increasing *FF* increases the number of scatterers, leading to higher scattering events, and therefore the number of cavities.

Comparing Figure 4-2a and Figure 4-2b with Figure 4-2c and Figure 4-2d, it can be seen that the effect of changing d_{av} is more pronounced than changing *FF* in shifting λ_r. For example, increasing d_{av} by 25% (from 120 to 150 nm) results in a redshift of 229 nm to the average λ_r. However, to obtain a redshift of 185 nm, *FF* needs to change by 100 % (from 0.4 to 0.2). This effect is further exemplified in two different arrays (array A: d_{av} = 120 nm, *FF* = 0.25 and array B: d_{av} = 90 nm, *FF* = 0.15). As shown in Figure 4-2e and Figure 4-2f, even though the FF of array B is slightly lower than that of array A, the effect of decreasing nanowire diameter on λ_r is significantly higher, with a blueshift of the cavity resonance by about 60 nm.

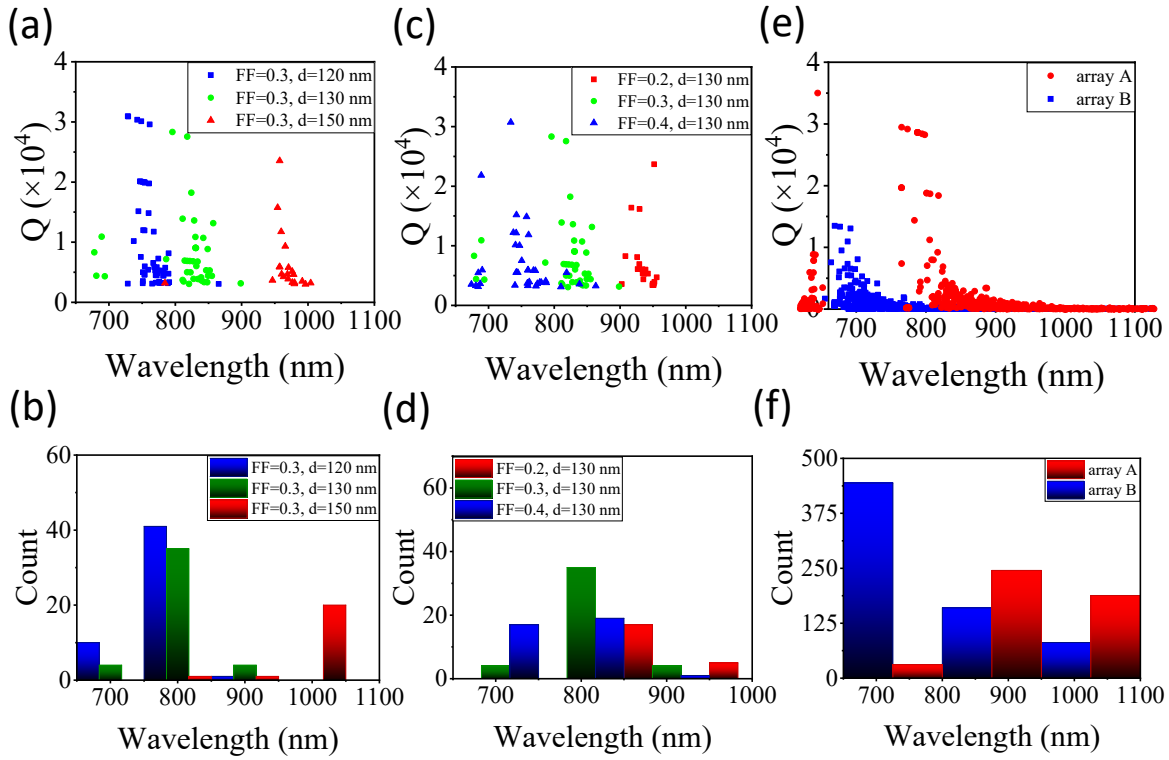

Figure 4-2: Effect of d_{av}, *FF* on the statistical distribution of *Q* and λ_r. (a,b) The effect of d_{av} at *FF* = 0.3 and σ_c = 50 nm on *Q* and λ_r of the cavity mode. (c,d) The effect of *FF* at d_{av} = 130 nm and σ_c = 50 nm on *Q* and λ_r of the cavity mode. (e,f) The effect of *FF* and d_{av} at a fixed σ_c value for two different arrays, A and B (array A: *FF* = 0.25, d_{av} = 125 nm; array B: *FF* = 0.15, d_{av} = 90 nm).

4.2.2 Effect of degree of randomness

Using the same 2D simulation setup, the effect of deviation from the NW centre, σ_c, which also quantifies the degree of randomness, is analysed for an array with d_{av} = 130 and *FF* = 0.3. Ten cases for four random arrays (σ_c = 10, 50, 70 nm, and completely random system) were analysed. Note that in the completely random case, the centres of the nanowire positions were generated by a random number generator without constraining it to a specific σ_c value. The results in Figure 4-3 show that in the 3 'restricted' random cases, the Qs of the cavities are more than four times higher than that of the array where the NWs are completely random, indicating that even for RL, some degree of engineering of the randomness could noticeably improve the device performance. For example, it has been shown that increasing the *Q* of lasing modes could make non-resonant lasing systems into resonant ones [134]. That is to say, engineering the randomness could increase the Qs of the modes and reduce the coupling and overlapping between modes, leading to RLs with highly localised modes [135] with resonant feedback [134]. Indeed, there is only a very small probability of finding cavities with high Qs in the completely random array.

Furthermore, the results show that the amount of disorder can also significantly affect the resonance wavelengths of the modes in addition to Q of the arrays. As the disorder strength increases, the possibility of obtaining modes with lower λ_r increases together with the wavelength resonance bandwidth. This is because as σ_c is increased, the possibility of having NWs closer together (i.e. denser) in localised regions is increased, so the possibility of getting resonances with lower wavelength resonances is increased. In other words, increasing the randomness degree would make the filling factor in localised regions more non-uniform, so according to Figure 4-2c and Figure 4-2d, the bandwidth increases. Considering InP NWs have gain in the wavelength region of 800 to 850 nm at low temperature, the array with σ_c = 50 nm has the best overlap with the gain profile of the NWs.

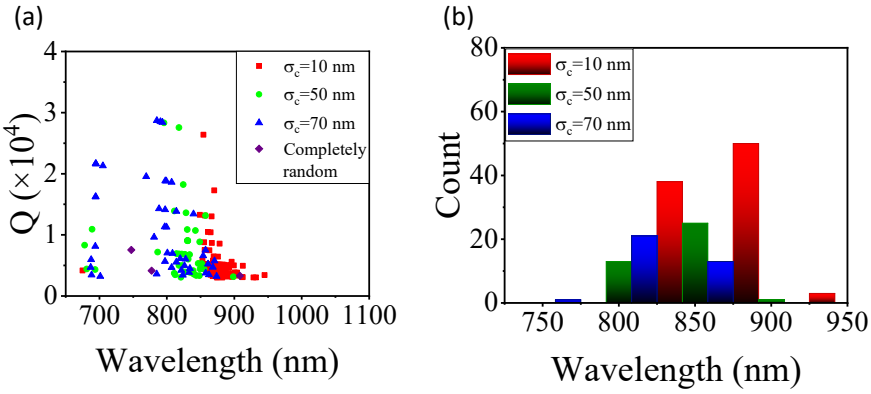

Figure 4-3: Effect of changing $\sigma_{c,max}$ while keeping the d=130 nm and FF=0.3 constant on Q (a) and λ_r (b) of the cavity modes.

4.2.3 Effect of the array size

To better quantify the effect of array size on mode leakage, a 3D setup similar to the one discussed in chapter 3, with d_{av} = 125, FF = 0.3, and $\sigma_{c,max}$ = 50, was used. For each array size, ten different cases were analysed. Unlike the 2D setup, where the mode is completely confined in the z-direction, in the 3D setup, the mode can leave the disordered media through the substrate in 3D, leading to lower Q factors. Using a 3D setup would result in more accurate quantification of real systems. Here, the selected resonance modes have two criteria: (I) Q > 100 and (II) 750 nm < λ_r < 900 nm. A single electric dipole source was placed at the centre of the random array, so only the modes in the middle of the systems were excited. Similar to the setup discussed in chapter 3, the top 1.1 μm of the NWs was assumed to have a higher refractive index than the rest of the NWs because of carrier generation and increased temperature [135]. It can be seen from Figure 4-4 when the size of the array (L_x, L_y) is less than 1 μm, the system cannot support a mode. Mode leakage will not allow the system to support cavities when the mode size is larger than the array size. In other words, the lateral

size of the array should be much bigger than l_t to be in the localisation regime and not the diffusive regime [9]. It can also be seen that at lateral sizes of around L_x, L_y = 2 μm, the system has the highest confinement property. The lateral area of the mode in this system for modes with Q > 100 is between ~0.05-3.75 μm^2. Therefore the lateral size of L_x, L_y = 2 μm (area size of 4 μm^2) is big enough to support a maximum number of the modes. At a larger array size, the number of supported modes begins to decrease. This trend can be understood because the array's surrounding region (air) acts as an optical 'cladding' layer for the modes. At 2 μm array size, the size of the modes is of the order of the array size, and hence the surrounding region provides a good optical contrast to confine the modes. However, with increasing array size, the modes are now further away from the surrounding air region, and because of the presence of other NWs, the effect of optical contrast is now diminished, leading to reduced lateral confinement strength. Figure 4-4a and Figure 4-4b show the statistical distribution of λ_r and Q of the modes in an array of size L_x, L_y =1 μm, where there are only a few modes that are supported. Due to the small size, out of the 10 cases studied, only five of them can support any modes with Q > 100. Furthermore, each system only supports a single-mode, implying that single-mode lasing is possible from small systems.

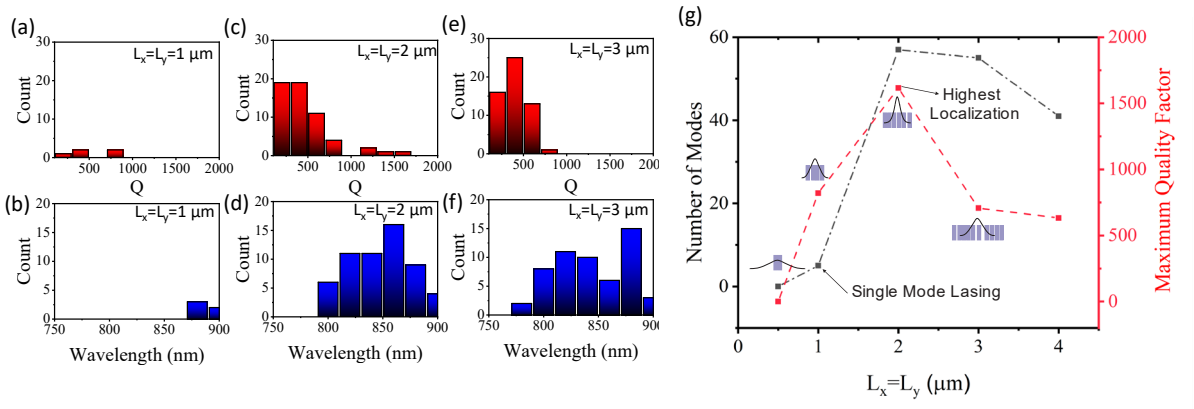

Figure 4-4: Effect of lateral array size on the cavity mode. (a-f) Statistical distributions showing the effect of L_x, L_y with FF = 0.3, d_{av} = 130 nm, and $\sigma_{c,max}$ = 50 nm on Q (top row) and λ_r (bottom row). (g) Effect of L_x, L_y on the number of modes with Q > 100 and Q_{max}.

4.2.4 Effect of the nanowire length

For optimising the length of the NWs, L_{NW}, a similar 3D simulation as the one used for the analysis of the effects of array size was conducted. Figure 4-5a and Figure 4-5b present the statistical distribution of λ_r and Q of the modes in two arrays with L_{NW} = 1.5 and 3 μm, respectively, for a fixed L_x, L_y = 4 μm and FF = 0.3. For both systems, the same random distribution of NWs was used. It can be seen for the system with the shorter NWs, the number of supported modes is very low, and the Q of the modes is about one-fourth of the array with

longer NWs. In Figure 4-5c-f, the electrical field intensity profiles of a mode at λ_r ~799 nm in the two systems are shown. The mode profiles along the length of the NWs (Figure 4-5c and Figure 4-5d) and in the x-y plane (Figure 4-5e and Figure 4-5f) are very similar for both arrays; however, the shorter NW sample shows a higher leakage into the substrate, resulting in lower Qs and number of resonant modes as shown in Figure 4-5a.

Figure 4-5g and Figure 4-5h show the experimental emission spectra at different excitation powers from the random arrays with the shorter (L_{NW} ~1.5 µm) and longer (L_{NW} ~3 µm) NWs, respectively. The insets show the SEM images of the InP nanowires of the two arrays grown using the SA-MOVPE [114] method, similar to the InP discussed in chapter 3. The substrate preparation and growth conditions are as following:

Substrate preparation: Before growth, a standard preparation process [69, 114] for patterned substrates was used. Using plasma-enhanced chemical vapour deposition, ~30 nm-thick SiO_x was deposited on semi-insulating (111)A InP substrates as a mask, followed by electron beam lithography to create the randomly positioned holes on the resist. The pattern was then transferred to the SiO_x mask through dry etching using CHF_3. The patterned substrate was trim-etched in 10 % H_3PO_4 to remove any native oxide layer[114] and then immediately loaded into the MOVPE system for nanowire growth.

Growth condition: A close-coupled showerhead (CCS) reactor (Aixtron 3 × 2 in.) at a low pressure of 100 mbar was utilised for the epitaxial growth. Highly purified H_2 with a total flow of 10 litres/min was used as the carrier gas. Trimethylindium and PH_3 were used as precursors for In and P, respectively. All substrates were first annealed in ambient PH_3 at a wafer surface temperature of 660 °C in the reactor. After a 10 min annealing, epitaxial growth was carried out once the reactor reached the desired conditions. To reduce the possibility of merging the NWs, the molar fraction of PH_3 was 1.25×10^{-3} mol min^{-1}, and for TMIn it was set to 2.1×10^{-6} mol min^{-1} leading to a V/III of ~595. Growth was performed at 680 °C for 8 and 4 min for the longer and shorter systems, respectively.

Optical characterisation was carried out at low temperature (T = 6 K) using a 522 nm pulsed laser using the same optical setup discussed in chapter 3 and shown in Figure 2-7. As shown in Figure 4-5g and Figure 4-5h, the emission spectra of the two systems have two peaks at the same wavelengths. The first peak at ~830 (FWHM ~22 nm) is due to emission from the NWs (wurtzite crystal phase) and the second peak at ~875 nm (FWHM ~13 nm) is mainly from the substrate (zincblende phase). It can be seen in the shorter NWs the intensity of the light emitted from the substrate at the wavelength of 875 nm is much stronger than the one emitted

from the nanowire. This is because the short array could not absorb light properly, and due to the leakage of the light to the substrate, the emission from the substrate is high.

Interestingly in the system with longer NWs, we observe a small peak appearing at 843 nm at the pump fluence of ~550 μJ cm^{-2} per pulse, further amplified with increasing excitation fluence. Beyond a lasing threshold of around 733 μJ cm^{-2}, a sharp lasing peak (FWHM = 2 nm) is observed at 843 nm. The power-dependent output intensity (upper left inset of Figure 4-5h) shows the typical "S"-curve shape and depicts all three PL regimes: spontaneous emission dominates at low excitation intensities until the onset of amplified spontaneous emission at ~550 μJ cm^{-2} (grey colour region) and finally, the emergence of lasing at ~733 μJ cm^{-2} [115-117]. In the short system, since the mode leakage to the substrate is high, the Q factor of the mode is low, leading to higher out-coupling loss and non-lasing behaviour.

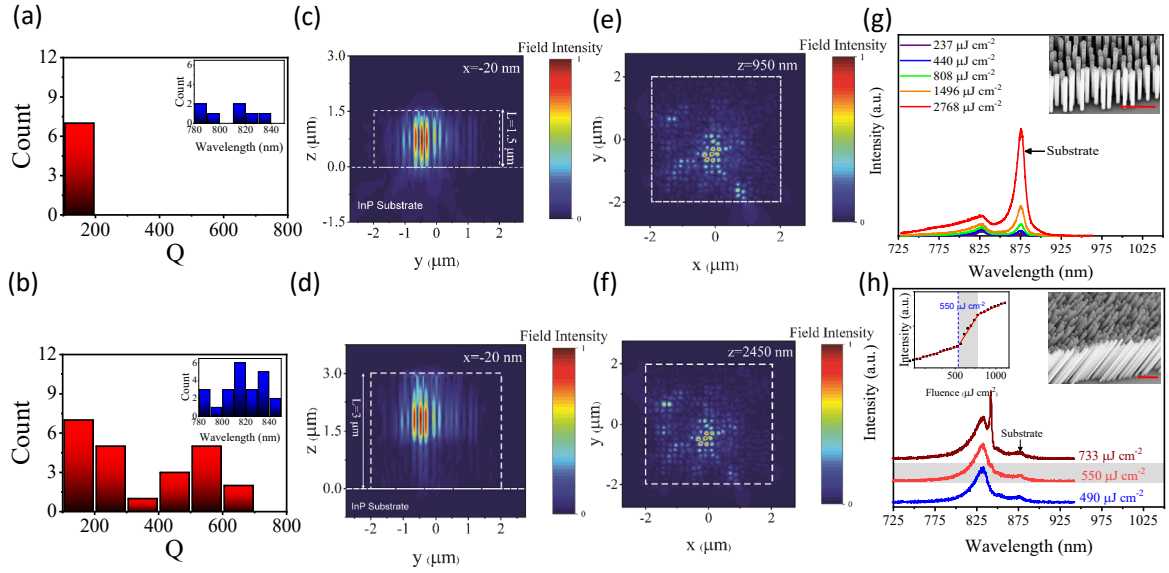

Figure 4-5: Effect of NW length on the cavity modes and optical profile. The top row is for an array with NWs of length L_{NW} = 1.5 μm, whilst the bottom row is for L_{NW}=3 μm. (a,b) Statistical distributions for Q and λ_r (inset) of the two arrays with shorter and longer NWs. (c-f) Electrical field intensity profile of a mode at λ_r ~799 nm on y-z (c,d) and x-y (e,f) planes of the two arrays with shorter and longer NWs. (g,h) Emission spectra of the two arrays with shorter and longer NWs. The inset SEM images show the tilted view of the two NW arrays grown by MOVPE (scale bar: 1 μm). The upper left inset in Figure 4-5h shows the log-log plot of light output from the random NW laser vs excitation power. The grey area is the region of amplified spontaneous emission. All measurements were done at 6 K.

4.3 Shifting the random lasers lasing wavelengths

Figure 4-6 shows the experimental studies on the effect of the average NW diameter on the modes for two different arrays corresponding to array A and array B mentioned before. As shown by our simulation results in Figure 4-1 and Figure 4-2, decreasing d_{av} results in a

blueshift of the resonance wavelength. This is because as the NW gets smaller, the scattering cross-section decreases and also experiences a blueshift [136]. This blueshift leads to the decrease of the λ_r of the modes. For example, it was shown average diameters of ~70–75 nm, and filling factors of ~0.3 are suitable parameters for disordered AlGaN nanowire arrays to lase at the ultraviolet UV-AII band (~320–340 nm) at low temperatures [100]; however, as shown in chapter 3 and Figure 4-1, for the wavelength of ~800 nm (near-infrared region) bigger NWs with diameters of ~130 nm could lead to higher Q factor lasing modes.

In Figure 4-6a, the SEM images of arrays A and B and their diameter distribution (inset) are shown. The emission spectra from an arbitrary area of these two arrays are plotted in Figure 4-6b. In both cases, lasing occurs in the range of around 725-850 nm, corresponding to the gain profile of InP NWs. The resonance wavelengths and threshold at which the amplified spontaneous emission region starts in these two arrays are plotted in Figure 4-6c and Figure 4-6d, respectively. Unlike Fabry-Perot mode lasing [137, 138] and non-resonant RLs[134], where the lasing wavelength is around the maximum of the gain with a narrow bandwidth of around $\Delta\lambda < 50$ nm, in each of these two resonant RLs, the lasing bandwidth is broader ($\Delta\lambda$ = 100 nm) and most of the lasing wavelengths are at wavelengths lower than the gain maximum. In array A, the minimum, maximum, and average lasing wavelengths are 742, 735, and 787 nm, respectively. For array B, where the average diameter is smaller, the corresponding lasing wavelengths are 725, 811, and 775 nm, respectively. So, decreasing the average diameter of the NW results in an overall blueshift of the resonance wavelength, confirming the results shown in Figure 4-2. As shown in Figure 4-6d, the lasing threshold in array B has generally increased, which could be due to two reasons. First, there is a lower probability of finding high *Q* modes in array B than array A (see Figure 4-2e) (higher loss due to out-coupling loss to the surrounding media). Secondly, the emission intensity of the wurtzite NWs in array A is higher than from the zincblende substrate (Figure 4-6b); however, in array B, the emission of the substrate is higher than the emission of the NW array. As discussed in relation to Figure 4-1a, this is because, in array B, the *FF* is lower, so the carrier generation inside the gain medium is lower, leading to lower gain. Additionally, the smaller diameter can lead to a higher surface recombination rate, resulting in lower carrier lifetime and higher optical loss. Higher emission in array A means more photons could be created with lower excitation power so that the lasing threshold would decrease.

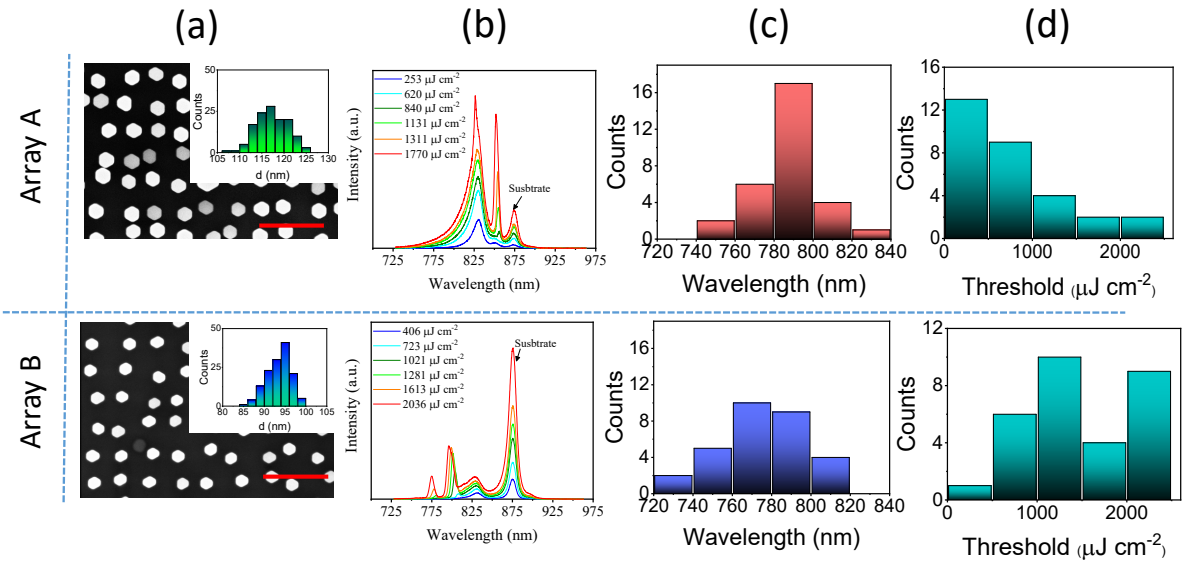

Figure 4-6: Experimental results showing the effect of average NW diameter on the emission and threshold of two different arrays, corresponding to array A (top row) and array B (bottom row). (a) Top-view SEM images. The insets show the diameter distributions of the two arrays. (b) Emission spectra with increasing pump fluence around the threshold. (c,d) Statistical distributions of the emission wavelength (c) and lasing threshold (d). All measurements were done at 6 K.

4.4 Type of the cavities

Lasers could have different types of cavities such as whispering gallery (WGM)-cavity, Fabry–Pérot (FP) cavity, and cavity based on random scattering of light in RLs. WGM is where the light wave is resonantly trapped inside dielectric spheres or disks by total internal reflection [139, 140]. In practice, the radius of a microsphere, *R* (typically, tens or hundreds of μm's), far exceeds the optical wavelength of interest, and the typical value of the polar index, *l*, (approximates the ratio of the optical length of the microsphere diameter to the mode wavelength) is greater than 100. Thus, the radiative leakage of the mode energy outside the cavity is negligible [141]. So, in our system, where the NW diameter is smaller than the resonant wavelength, the possibility of WGM is ruled out. In addition, the possibility of FP modes is also ruled out, and the cavities are based on random scattering of light because of the following reasons:

First, earlier reports have shown that a GaAs nanowire lying on a low-index substrate, such as SiO_2, require diameters larger than ~ 200-250 nm to obtain both a good mode effective index (i.e. to support lowest-order guided mode) and low threshold (for 6 μm long nanowires)[142]. Considering the average diameter of the grown nanowires (less than 150 nm for both system A and system B) and the shorter lengths (i.e. smaller gain volume) in this work, the possibility of FP lasing can be ruled out.

Secondly, the grown SA-MOVPE NWs are still attached to the growth InP substrate with a very thin 30 nm SiO_x in between the NWs. Therefore, due to the mode leakage into the substrate, it is improbable that the cavity of the modes is FP. In other words, the modes reflectivities from the bottom mirror are so low leading to higher loss and very high lasing thresholds for FP modes.

Thirdly, in our experiments, we illuminated the NWs from the top, and considering the carrier diffusion, the carriers are only generated at the top 1 um of the NWs. As this is the only region that provides gain, it is unlikely FP mode lasing can occur.

Finally, considering the effects of the geometrical parameter change discussed in this chapter, such as the blue-shift of the modes when decreasing the sizes of the NWs and the behaviour of the modes by changing the NW length [115, 143], the cavities of these modes are due to disorder-induced scattering.

4.5 Conclusion

In this chapter, we have shown the controllability of the lasing properties of random InP NW laser designed in chapter 3. It was demonstrated by changing the design parameters of this random laser, it is possible to change the lasing threshold, the number of lasing modes, the Q factor, and the wavelength resonances of the modes. For example, changing the lateral size of the array would lead to a change from multi-mode to single-mode lasing. It was also shown by changing the density and diameter of the NWs, and the degree of randomness could change the resonance wavelength of the modes. The ability to engineer the modes in random lasers could expand the application of random lasers where stable broadband wavelength-controlled lasers over large areal sizes are required.

Chapter 5: Types of feedback in random lasers: Resonant vs. Non-resonant

5.1 Introduction

As discussed in the previous chapters, random lasers (RLs) are non-conventional lasers whose feedback mechanism is based on multiple scattering induced by random scatterers rather than defined optical cavities [3]. Due to the nature of the cavities in RLs, these devices could lead to mirror-less lasers with less fabrication complexity than lasers with conventional cavities, such as Fabry–Pérot [144] and whispering gallery modes [140] cavities. Even though, as discussed in chapter 3, it is challenging to obtain stable lasing modes and the Q factor of the lasing modes in these devices is lower than the lasers with conventional type of cavities, RLs could be used in thermal [145] and mechanical [7] tunable lasers and other applications, such as spectrometers [146], speckle-free imaging [6] and display [147, 148] tools.

In conventional lasers, scattering is usually considered a detrimental process where it can uncouple the resonant lasing modes. However, scattering is a necessary mechanism for lasing, in addition to the gain of the system. In these systems, the photon is scattered in the disordered media, increasing the optical path of the photon. If the disordered medium is accompanied by gain medium, then the light gets amplified. In 1968 Letokhov theoretically predicted this kind of diffusive motion of photons could lead to lasing phenomena [14], but it took around 26 years to observe random lasing experimentally [41]. In these RLs, the scattering events only increase the path length without forming closed-loop cavities and showing resonant behaviour, so the lasing behaviour is referred to RLs with non-resonant or incoherent feedback. Later on, using ZnO powders deposited on ITO [43], it was shown that disordered medium not only could increase the optical path of the light, but could also increase the chance for the light to create closed-loop paths which are resonant in nature. In other words, if the scattering is strong enough, light can create a closed-loop path, and allow its return back to its origin, thus forming a scattering-based cavity. Due to the resonant nature of this feedback, the cavity will only support specific wavelengths, and the RLs are referred to as RLs with resonant or coherent feedback. These two kinds of feedbacks in RLs are discussed in more detail below.

Non-resonant feedback random lasers: In the non-resonant type of feedback, spontaneously emitted photons undergo scattering in the disorder media, and if the disordered medium is also active (medium with gain), then additional photons are generated through the

stimulated emission process. In these RLs, the feedback provided by the disordered medium only increases the dwell time of the photon in the medium and only returns parts of the photons to the gain medium but not to the origin position, so any spatial resonance is absent. Therefore, the spectrum from such systems does not contain discrete components at specific resonant frequencies but is determined solely by the gain curve of the active medium. Thus, this process is essentially amplified spontaneous emission (ASE), whereby lasing occurs at the frequency where the gain is maximum, and the emitted light is not coherent.

Here, a large number of low Q factor resonances spectrally overlap and form a continuous spectrum. However, because the modes are coupled, the photon loss rate is lower and usually occurs at lower pumping thresholds. The photon exchange among the modes leads to a much lower photon loss rate for a set of interacting modes than for a single-mode [3, 29]. In other words, in the non-resonant modes, the eigenmodes interact with each other, so the photons can hop between modes leading to a lower rate of photon loss rate and higher photon lifetime in these coupled modes.

In addition, small volume lasing with a low threshold could be achieved in cavity-free non-resonant lasers due to the relationship between optical gain and cavity loss, whereas the volume of the resonator is reduced, the gain volume is also reduced. This may lead to an increase in lasing threshold, and even lasing may not occur in some cases. Besides, localisation of light in small volume in the cavities of resonant-based RLs might increase the local temperature that might decompose materials such as InP (decomposition temperature of InP is around T = 573 K [149]). In non-resonant RLs, however, since there is no cavity there are no such issues.

Non-resonant lasing has been reported in different structures such as laser paints [150] and powder lasers [151]. As shown in Figure 5-1, as the pumping intensity increases, only narrowing of the PL spectrum at the peak of the gain spectrum is observed.

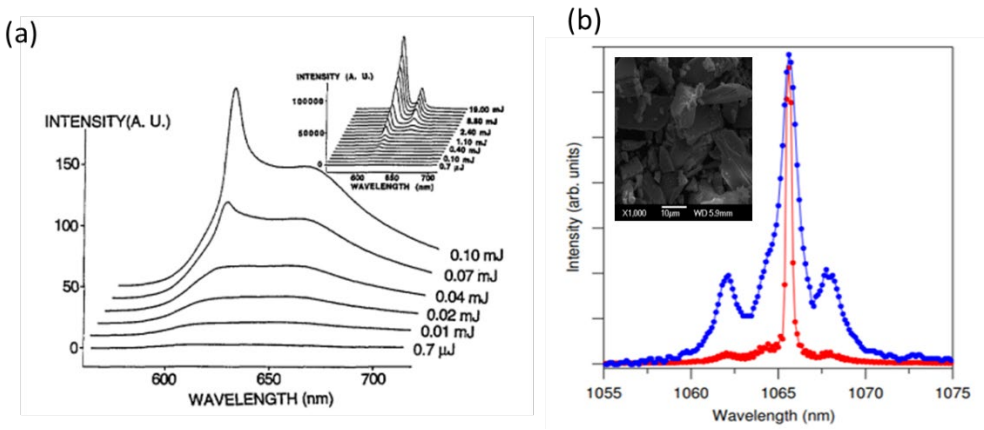

Figure 5-1: RLs with non-resonant feedback mechanism: (a) Emission spectra from a laser paint, a solution of R64 dye in methanol containing TiO_2 nanoparticles, (b) Emission spectra from Nd^{3+}(3%) $LuVO_4$ powder obtained at pumping intensities below (blue) and above (red) the lasing threshold. The figures have been taken from [150, 151].

Resonant feedback random lasers: In resonant feedback RLs, scattered light is trapped in closed-loop paths where interference occurs. Unlike the broad spectrum of non-resonant lasers, resonant lasers are characterised by discrete resonant peaks at different wavelengths with more coherent emissions. The behaviour of RLs with coherent feedback is very similar to the lasers with conventional cavities. The wavelengths of resonant modes are determined by the scattering efficiency of the system, which depends mainly on geometrical parameters, such as size [100], fill factor, [102, 152] density,[29] and also the position [153] of the scatterers. This is advantageous for resonant feedback random lasers since it enables the tuning of the lasing wavelength. For example, by changing the scattering efficiency of RLs with resonant feedback as discussed in chapter 4, it is possible to manage the lasing parameters such as the number of modes [131], resonant wavelength and polarisation. Besides, RLs with resonant feedback could be used in thermal [145] and mechanical [7] tunable lasers. Figure 5-2 shows the emission spectra of different disordered media with resonant feedback behaviour where above the threshold discrete resonant peaks at different wavelengths could be observed.

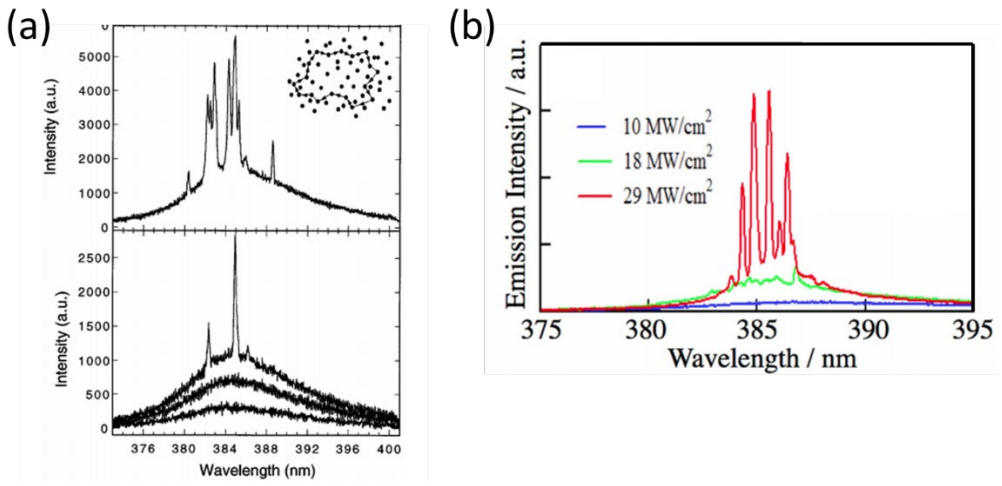

Figure 5-2: RLs with resonant feedback mechanism: (a) Emission spectra from ZnO powder where the excitation intensity is increased for the lower spectra to the upper one. Inset shows the schematic of the formation of a resonant cavity and the return of the light to its origin. (b) Emission spectra of a ZnO nanorod array at different pumping intensities. The figures have been taken from [43] and [154].

In Table 5-1: Resonant feedback vs. Non-resonant feedback in RLs the properties of the resonant and non-resonant RLs are summarised. Considering the advantages and disadvantages of different feedback mechanisms, the ability to control the laser to lase either in resonant or non-resonant mode is interesting. As discussed in chapter 4, different methods have been introduced to control different lasing parameters; however, only a few methods are shown to control the type of feedback mechanisms in RLs. For example, it has been demonstrated that increasing the disordered medium's scattering efficiency would decrease the transport mean free path of light and the coupling among the modes. In other words, this would increase the cavities' Q factor, and the RL's chance to operate with resonant mode feedback increases. In one study, to increase the scattering efficiency, the density of scatterers was increased, and transition from ASE to lasing with coherent feedback was observed [29]. Other than increasing the Q factor of the modes in managing the type of feedback in RLs, changing the number of interacting modes also could change the type of cavity. Increasing the number of the modes would increase the chance of coupling between modes and the photon lifetime, increasing the likelihood of lasing with non-resonant feedback. For example, in one study, changing the conventional circular-shaped (or disc-shaped) pumping light to a directional, stripe-shaped one, where a lower number of modes are excited and coupling among the modes is reduced, the lasing transition from non-resonant to resonant mode was demonstrated [127].

Table 5-1: Resonant feedback vs. Non-resonant feedback in RLs

RLs with resonant feedback	RLs with non-resonant feedback
1- Discrete and narrow peaks are observed in the emission spectrum above the threshold. 2- According to the structure of the pumping area, the peaks could happen at different resonant wavelengths within the gain curve. 4- Modes are less coupled, leading to more localised and stable modes 5- Lasing wavelength could be tuned (chapter 4) and could be used in tunable lasers. 6- Showing behaviour similar to the cavities of conventional lasers.	1- Do not show sharp peaks in the emission spectrum. 2- Narrowing of the emission spectrum around the wavelength where the gain is maximum. 3- The emission spectrum narrows above the threshold but is much broader than the peaks seen in resonant RLs. 4- Usually, the lasing threshold is lower than that of resonant RLs because of coupling between modes. 5- Due to the coupling between modes, the photon lifetime is higher.

In this chapter, we report RLs based on Au-catalysed GaAs nanowires (NWs) and provide several practical methods for controlling the resonant and non-resonant modes in the system. In the first sample, the nanowires were grown on Si substrates leading to randomly oriented NWs. In this sample, both resonant and non-resonant modes were observed. The simulation results show that aligning the NWs would improve the Q factor of the modes and increase the number of high Q factor modes. In the second sample, to make the resonant mode dominant and suppress the non-resonant mode, the NWs were grown on GaAs (111)B substrates, leading to vertically aligned NWs. Here, as expected, the broader non-resonant peak was suppressed.

On the other hand, to suppress the resonant mode in the second sample, the light was defocused by moving the stage of the sample lower and tilting the stage. Defocusing the light increases the size of the pumping area, which could increase the chance of non-resonant modes in the system for two reasons: (1) increased pumping area can lead to a higher number of modes interacting [127], (2) decreased excitation intensity reduces the chances of resonant mode lasing as they usually have a higher threshold. This simple method used to switch between the type of lasing modes provides a pathway for the realisation of nanoscale light sources for the next-generation photonic devices.

5.2 Samples preparation

The GaAs NWs were grown on either Si or GaAs (111)B substrates via the Au-assisted vapour-liquid-solid (VLS) growth mechanism to prepare the samples. To minimise surface recombination velocity [108] and Fermi level pinning [155], the NWs were then passivated with a thin AlGaAs shell and further with a few nanometers thin GaAs cap to prevent oxidation of the AlGaAs layer.

Growth condition: The NWs were grown in a horizontal flow MOCVD system using Au seeded VLS growth. The Au particles were dispersed using nominally 20 nm colloidal solution and poly-L-lysine. The growth was initiated with 10-minute annealing at 600 °C under AsH_3 flow. The NW core was grown at 450 °C using a trimethylgallium (TMGa) flow of 11.6 µmol min^{-1} and V/III ratio of 46. After the core growth, the reactor temperature was increased to 650 °C under AsH_3 flow. Then, by changing the TMGa flow of 23.2 µmol min^{-1} with a V/III ratio of 46, radial growth was promoted to increase the diameter of the GaAs core. Next, the temperature was increased to 750 °C under AsH_3 flow for AlGaAs shell growth using TMGa (11.6 µmol min^{-1}), trimethylaluminum (11.6 µmol min^{-1}), and AsH_3 (1.52 mmol min^{-1}). Finally, a nominally few nm-thick GaAs cap was deposited, and the reactor was cooled down to room temperature under AsH_3 flow.

5.3 Structural characterisation

Figure 5-3 shows the SEM images of the GaAs-AlGaAs core-shell NWs grown on GaAs (111)B (a,b) and Si (c,d).

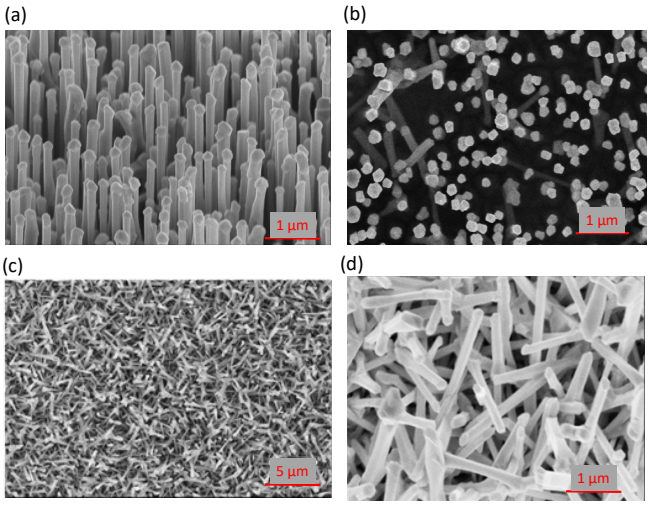

Figure 5-3: SEM images showing (a) tilted and (b) top view of the NWs grown on GaAs (111)B. (c) SEM image showing the top view of the NWs grown on Si. (d) Magnified top-view SEM image of the NWs grown on Si.

As seen from Figure 5-3a, the NWs grown on GaAs (111)B are vertically aligned. The length of these NWs is around 3 μm with the average diameter (d_{av}) and filling factor (*FF*) of d_{av}≈140 nm and *FF*≈0.26. However, from Figure 5-3c,d, the NWs grown on Si are randomly oriented with an average length of ~4.5 μm and diameters in the range of ~150-250 nm.

The STEM image and EDX elemental mapping of the core-shell NWs are shown in Figure 5-4. It can be seen from the STEM image shown in Figure 5-4a the GaAs core region is surrounded by a very thin AlGaAs shell, comprising only ~10% of the total NW diameter. In this structure, GaAs core acts as the gain material, and AlGaAs shell mainly contributes to the passivation. The EDX elemental mappings of the core-shell NW shown in Figure 5-4b confirm the core-shell structure of the NW.

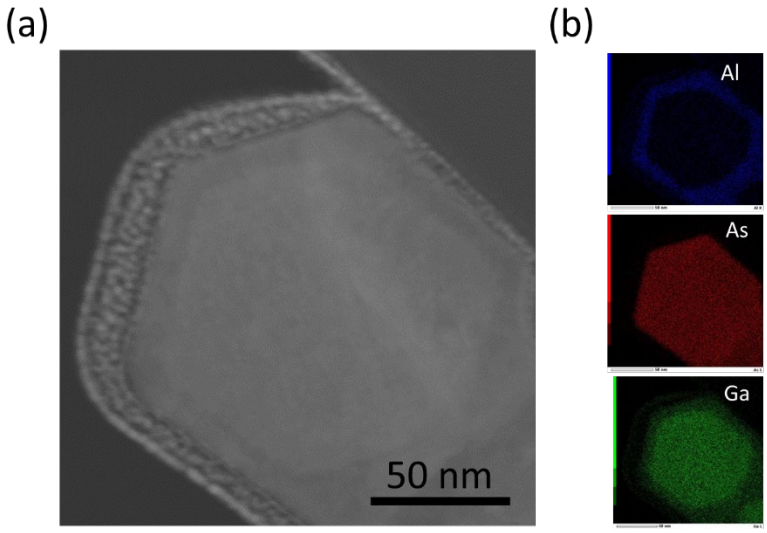

Figure 5-4: (a) STEM image and (b) EDX elemental mapping of the core-shell GaAs-AlGaAs NWs.

5.4 Design and simulation

Here, using numerical simulations, we show that aligning the NWs would increase the Q factor of the cavities and improve the resonant nature of the modes. This could be used to favour the formation of resonant modes in the disordered medium.

To understand better the effect of NW orientation on the resonant modes, we use Lumerical FDTD Solutions to solve Maxwell's curl equations in three dimensions. Figure 5-5a shows the Q factor and resonance wavelength, λ_r, of the various modes for three different systems:

- System (I): randomly oriented NWs (polar angle, φ, of the NW is a uniform random number between -180° and 180°, and the azimuthal angle, θ, is 45°),

- System (II): tilted NWs (φ=0° and θ= 45°),
- System (III): vertical NWs (φ=0° and θ= 0°).

Figure 5-5b shows the zy cross-section of the mode profile with the highest Q factor.

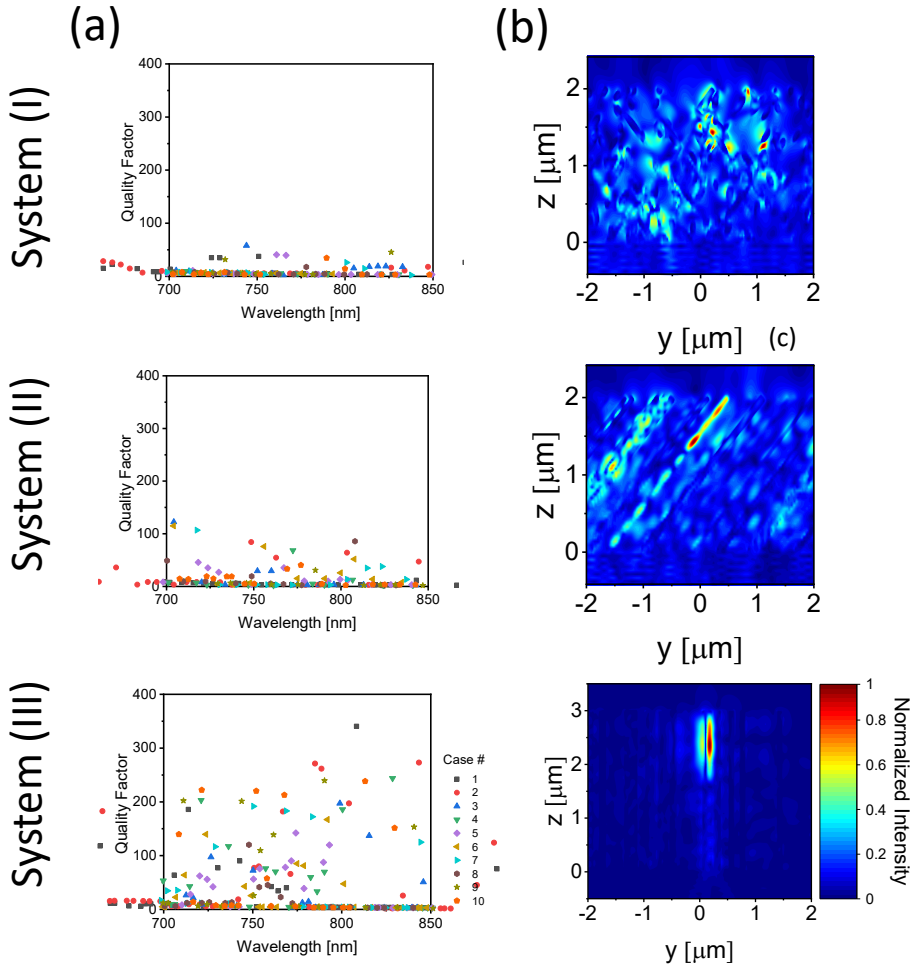

Figure 5-5: (a) Q factor and λ_r plot of three systems: (I) randomly oriented NWs, (II) tilted NWs (θ= 45°), and (III) vertically aligned NWs. (b) The zy cross-section mode profiles of the case with the highest Q factors for each system. The modes have Q factor=58, 122, and 341 at λ_r=744, 704, and 808 nm, for system (I), system (II), and system (III), respectively.

In the simulations, the NW length, L, was 3 μm, and the lateral sizes of the random array along the x and y axes (L_x and L_y) were both 4 μm, bigger than 3 μm, so that the disordered media could support even leaky modes. The optimum filling factor, *FF*, and NW diameter, d, to support high Q factor cavities for the system with the vertical NWs were *FF*=0.3 and d=140 nm. For the two other systems, because the NWs were tilted, the projected cross-sections of the NWs were larger than in the case of vertical NWs, and this had been taken into account. Because of the random nature of the systems, ten different cases (case 1 to case 10) were used for each system. In each system, the cases had the same *FF* and d values, and only the

NW positions (for all the three systems) and orientations (for the system (I)) were different. Since the refractive index of Si (n= 3.69 at 800 nm) and GaAs (n= 3.68 at 800 nm) are almost the same, we do not expect the type of substrate in the simulation setup to make any difference.

Similarly, the refractive indices of AlGaAs and GaAs are very similar, and therefore we do not expect a significant difference in the simulation results between bare and core-shell NWs. Also shown by the STEM and EDX images in Figure 5-4, the thickness of the AlGaAs shell is very small (10% of the diameter) and should have minimal effect on the simulation results. So considering the mentioned points, it was assumed that the GaAs NWs (n=3.68 at λ=800 nm [156]) were positioned on GaAs substrate. As discussed in detail in chapter 3, considering the temperature [112] and carrier generation [113], the top 1 µm of the NWs [108] (1 µm corresponds to the diffusion length) were assumed to have a higher refractive index of 0.12 than the rest of the NWs.

Comparing system (I) and system (II) in Figure 5-5a, it can be seen that aligned NWs can support cavities with higher Q factors. The constant *FF* in the z-direction for the aligned NWs facilitates the localisation of light in the lateral (xy) plane. Comparing system (II) and system (III) in Figure 5-5a, it can be seen that vertically aligned NWs can support cavities with even higher Q factor values. This is because, in vertically aligned NWs, the effective length of the higher refractive index part becomes longer than that in tilted NWs, leading to lower leakage into the substrate and better confinement of light. Considering the better confinement nature of the vertically oriented NWs, the possibility to form high Q factor cavities increases leading to a significantly higher chance for resonant lasing.

5.5 Optical Characterisation

Measurement setup: For the photoluminescence (PL) measurements, a frequency-doubled pulsed laser (femtoTRAIN IC-Yb-2000, λ_{source} = 522 nm, repetition rate 20.8 MHz, pulse width 300 fs) with a Gaussian beam profile (FWHM~5 um) was used to excite the random NWs through a long working distance objective lens (Nikon CFI Plan Fluor 60x/0.70 NA). The resulting emission was collected through the same lens and passed through a long-pass filter to remove the pump laser. Spectral measurements and near-field profiles were made using a grating spectrometer (Acton SpectraPro 2750) and a CCD camera (Princeton Instruments, PIXIS). Low-temperature experiments were conducted in a He-cooled cryostat (Janis ST-500).

Figure 5-6a presents the emission spectra under different excitation intensities of the randomly oriented NWs grown on Si substrate (system (I)). It can be seen the spectrum narrows in two

different ways as the pumping intensity increases. Initially, with increasing pumping intensities, the peak narrows at the wavelength corresponding to gain maximum. This peak is fixed in wavelength at the gain curve peak of GaAs and is therefore attributed to lasing with non-resonant feedback. With a further increase in the excitation intensity, additional peaks appear with significantly narrower linewidth. These peaks are observed at various wavelengths, i.e. they are not bound to gain maximum and are attributed to resonant modes. [93]

To further study the observed peaks' nature, near-field profiles of the emission spectra were measured at the pump fluence, P_{in}, of 1051, 1400, and 1746 μJ cm^{-2} per pulse (Figure 5-6b). At P_{in}=1051 μJ cm^{-2} per pulse, only weak scattering occurs and results in many coupled cavities. As shown in the simulation results (Figure 5-5a, system (I)), the modes in these randomly oriented arrays typically have low Q factors. These low Q factor cavities interact with each other, leading to photon exchange among the cavities, which prevents the stabilisation of the photon to a single-mode and therefore results in non-resonant lasing[127]. As demonstrated in Figure 5-6b, by increasing the pump fluence to P_{in}=1400 μJ cm^{-2} per pulse, two localised regions become isolated from the coupled modes. The higher intensity region corresponds to the sharp 801 nm peak in Figure 5-6a. The other lower intensity region corresponds to the resonant mode at 813 nm, which emerges in the spectrum at 1746 μJ cm^{-2} per pulse. The localised nature of these modes and their emission wavelengths outside the gain maximum region indicate their resonant nature [96].

Comparing the thresholds of the non-resonant and resonant modes, the onset of the former is much lower. As discussed before, this is attributed to photon exchange among the modes resulting in a much lower photon loss rate for a set of interacting modes than for a single mode. [3, 29] In other words, in the non-resonant modes, the eigenmodes interact with each other so that the photons can hop between modes leading to a lower rate of photon loss. When the optical gain increases, it first reaches the threshold for lasing for the modes coupled at the frequency of gain maximum (the non-resonant mode) owing to the higher photon lifetime in these coupled modes. As the optical gain increases further, it can coincide with a particular single-mode with the longest lifetime among the resonant modes. Then, lasing occurs in this mode in addition to the non-resonant mode.

When the pump fluence increases further from 1400 to 1746 μJ cm^{-2} per pulse, the optical gain increases and another localised mode appears at the wavelength of ~813 nm in the emission spectrum (as shown in Figure 5-6a). Because of gain competition between lasing modes, the increase in pump fluence results in a decrease in the intensity of the 801 nm peak.

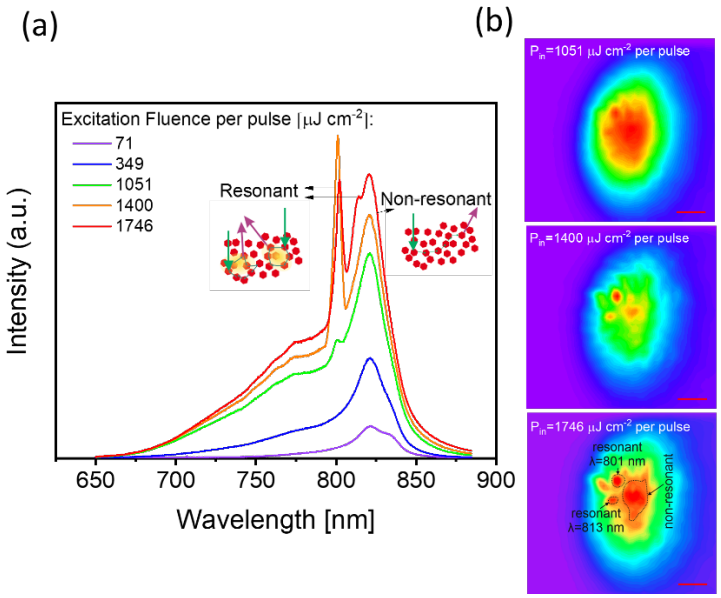

Figure 5-6: (a) Emission spectra of the GaAs-AlGaAs core−shell random NWs grown on silicon (system (I)) at T=6 K. The resonant and non-resonant lasing behaviours are schematically shown, and their corresponding lasing peaks are indicated by the arrows. (b) Near-field optical profiles of the laser at the excitation fluence of 1051, 1400, and 1746 μJ cm^{-2} per pulse. The scale bars are 1 μm.

5.5.1 Suppressing the non-resonant mode

To suppress the non-resonant mode and to make the resonant lasing modes more dominant, as discussed before, the NWs were grown vertically aligned so that the disordered media could have the highest probability for high Q factor cavities. For this purpose, vertically aligned NWs were grown on GaAs (111)B substrates with almost a similar average diameter and filling factor (d_{av}≈140 nm, FF≈0.26) as described in the simulation.

Figure 5-7 shows the emission spectra and near-field profiles from the GaAs NWs grown on GaAs(111)B (vertically aligned and randomly positioned NWs). Comparison of Figure 5-7a and Figure 5-6a shows clearly that the non-resonant peak has been suppressed. Comparing the near-field emission of the two systems (Figure 5-6b and Figure 5-7b), the vertically aligned NWs exhibit a more localised emission profile, and the PL background emission from the non-lasing regions is suppressed. The emission spectra and near-field images of the random system with the vertically aligned NWs show that as the excitation fluence increases from 175 to 349 μJ cm^{-2} per pulse, the region with the highest intensity emission corresponds to the localised mode at λ=760 nm, and the mode profile results from the suppression of mode coupling. As the excitation fluence increases further to 698 μJ cm^{-2} per pulse, the intensity of another mode at λ=755 nm becomes dominant.

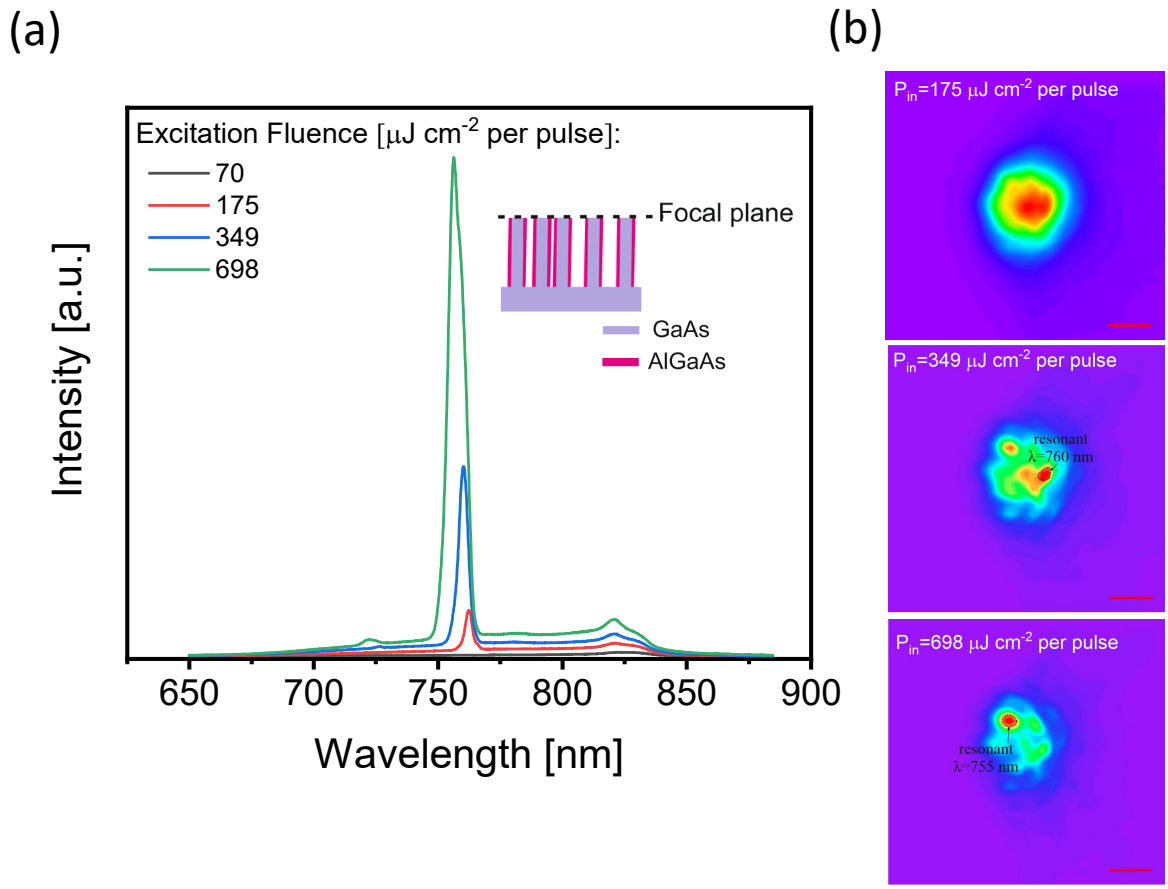

Figure 5-7: (a) Emission spectra of the vertically aligned GaAs-AlGaAs core-shell NWs grown on GaAs (111)B at *T*=6 K. Inset: Schematic of the vertical NWs and the focal plane of the excitation source positioned on the tip of the NWs. (b) near field profiles of the NWs under the excitation fluence of 175, 349, and 698 μJ cm^{-2} per pulse. The scale bars are 1 μm.

5.5.2 Suppressing the resonant mode

In the previous section, it was shown that resonant modes could be favoured by the design of the nanowire system. Here, we show another method of tuning between resonant and non-resonant modes within the same NW system and ways to suppress the resonant mode. As discussed before, due to the coupling between modes, typically, the non-resonant modes have lower thresholds than the resonant modes (see also Figure 5-6a)[29], which could be utilised to select the type of modes. However, as shown in Figure 5-7a, generally reducing the excitation fluence alone is not effective in suppressing the resonant modes. On the other hand, it has been reported that mode coupling or overlapping could suppress resonances.[127] Here, these two aspects are combined by defocusing the light, which both decreases the excitation fluence and illuminates a larger area. As such, a larger number of modes are illuminated, which increases the chances of non-resonant modes occurring. In other words, defocusing the excitation source increases the possibility of the involvement of a higher number of low-Q

modes with lower thresholds. Therefore, in this scenario, resonant modes are suppressed and non-resonant modes become dominant.

To defocus the light, two methods for defocusing the light were studied using the vertically aligned NWs, where the resonant modes are naturally dominant. First, by moving the sample stage lower, instead of focusing the excitation source on the tip of the NWs, the beam was focused several micrometres above the NWs. Second, the stage was tilted by 45° to extend the focal plane across different positions along the NW length. Figure 5-8 shows these scenarios and the corresponding spectrum and near-field emission images.

In Figure 5-8a, b, the NWs tips were moved away from the focal plane, and in Figure 5-8c, d, the stage was tilted 45°. It can be seen from the emission spectra that the resonant modes are suppressed, and only the non-resonant modes have become dominant. It can be seen from the near field images (Figure 5-8b and Figure 5-8d) that the pumping area has increased in comparison to the area presented in Figure 5-7b, so a higher number of NWs are illuminated (note the same 1 μm scale bars in near-field emission images in the two figures). Besides, the near field images show the spatial mode profile is much less localised, and all the modes are coupled, so no localised mode can be observed. As a result, the resonant modes are suppressed, and the non-resonant mode is favoured.

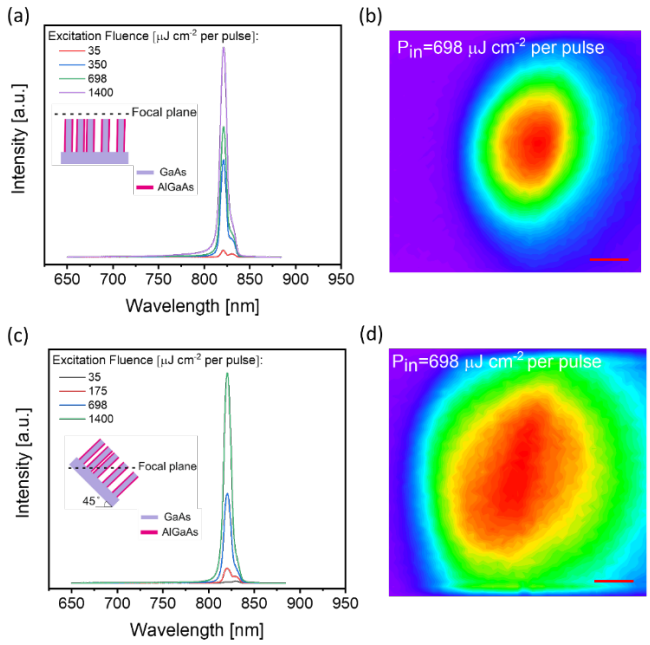

Figure 5-8: Emission spectra of vertically aligned NWs using defocused light by (a) moving the sample vertically away from the focal plane of the excitation source and (c) tilting the sample stage at T=6 K. Insets show the schematics of the NWs where the two different methods for defocusing the light are used. (d) Near-field mode profiles of the system by (b) moving the stage vertically and (d) tilting the stage at P_{in} =698 μJ cm^{-2} per pulse. The scale bars are 1 μm.

5.6 Resonant vs. non-resonant lasing

We measured the integral spectral intensity as a function of pump fluence for both resonant and non-resonant lasing modes (Figure 5-9a and Figure 5-9d) to compare their behaviour. Figure 5-9a demonstrates the threshold knee behaviour in the L–L data plotted on a linear scale for the NWs grown on GaAs(111)B (vertically aligned NWs) when the light is focused on the tip of the NWs (i.e. in the resonant mode). The black squares represent the experimental data, and the red lines are the lines fitted to the points below and above the lasing threshold. Figure 5-9b shows that above the lasing threshold of ~617 μJ cm^{-2} per pulse, a sharp peak emerges at the wavelength of 811 nm, corresponding to the resonant mode. The inset in Figure 5-9a shows the power-dependent output intensity on a log-log scale which follows the typical "S"-curve shape [157], where three emission regimes could be observed. At low excitation intensities, spontaneous emission dominates until the transition to ASE at ~617 μJ cm^{-2} per pulse, followed by a super-linear increase corresponding to the ASE (shaded blue region), and finally, the emergence of lasing above 1194 μJ cm^{-2} per pulse. A plot of the FWHM of the lasing peak at λ=811 nm as a function of pump fluence is shown in Figure 5-9 (c). Below the lasing threshold, the FWHM is bigger than 50 nm, while above the lasing threshold, it becomes as low as ~3.8 nm.

The L–L data plotted on a linear scale is shown in Figure 5-9d for the vertically oriented NWs where the light is defocused from the tip of the NWs when the stage is tilted at 45°. It can be seen that the non-resonant lasing behaviour is similar to an ASE source or a thresholdless laser. Figure 5-9e shows the PL spectra of this non-resonant laser, where the lasing intensity increases much faster at λ=819 nm than background emission and also gets narrower. The FWHM of the non-resonant lasing peak is presented in Figure 5-9f, where it narrows by nearly a factor of 4 to as low as ~7 nm above the lasing threshold, which is still much higher than that of the laser operating in resonant mode.

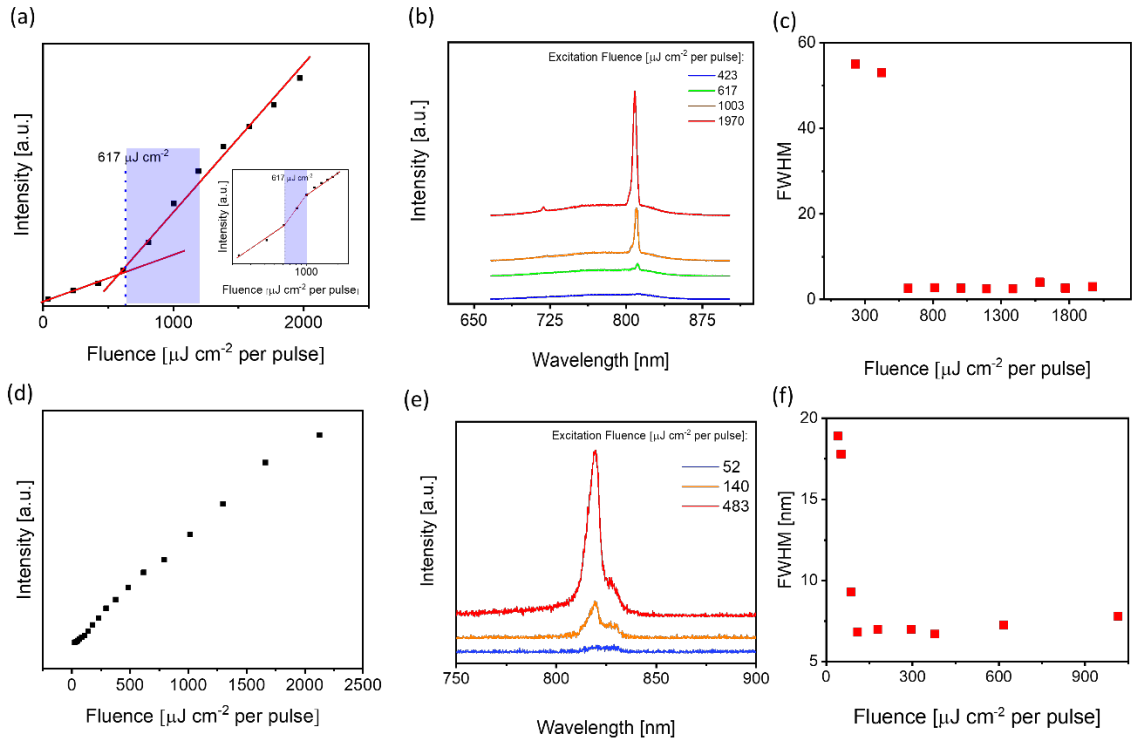

Figure 5-9: Integrated spectral intensity as a function of pump fluence for (a) the resonant (the excitation source was focussed onto the tip of the NWs) and (d) non-resonant (the NWs were tilted 45° from the focal plane of the excitation source) lasers. The PL spectra as a function of pump fluence for the (b) resonant and (e) non-resonant lasers. The FWHM of the lasing peaks as a function of pump fluence for the (c) resonant and (f) non-resonant lasers. All measurements were done at 6 K.

5.7 Conclusions

The unique features of random lasers such as angular free emission, tunability of lasing direction, low spatial coherence with high photon degeneracy, large area lasing, lasing from flexible substrates, facile fabrication methods and lower cost, make them of great interest for various applications such as in speckle-free laser imaging and display technologies. In random lasers, light experiences multiple scattering, as a result, the optical path increases, leading to the amplification of light in the gain medium. If the gain balances the loss, non-resonant lasing based on amplified spontaneous emission could happen in these disordered media. However, the light passing through this scattering medium also can return to its origin and create resonant cavities. If this lasing condition is fulfilled, resonant based random lasing could happen. Both non-resonant and resonant lasing modes have some unique properties. For example, in non-resonant mode, lasing could happen at lower lasing thresholds, and the lasing frequency coincides with the gain maximum.

On the other hand, in the case of resonant mode lasing, the emission frequency could happen at any frequency within the gain spectrum. So, in the resonant mode random lasers, there is a possibility of controlling the wavelength emission of random lasers. Furthermore, unlike non-resonant mode lasing, the emitted light is coherent and similar to conventional mirror-based lasers.

Here, we have shown both resonant and non-resonant lasing modes in the randomly oriented GaAs-AlGaAs core-shell NWs. By making the NWs aligned, the chance of resonant mode lasing can be increased whilst suppressing non-resonant mode lasing. Furthermore, we show that changing the focal plane position relative to the NW array makes it possible to increase the coupling among low Q factor lasing modes while decreasing the fluence of excitation light can lead to the suppression of resonant modes. Interestingly, the non-resonant lasing modes have extremely low threshold, near thresholdless lasing behaviour. Resonant mode lasing shows stable sharp peaks in the spectrum with high spatial localisation. The practical methods introduced to engineer the type of lasing modes provide a pathway for the realisation of nanoscale light sources for the next-generation photonic devices, with the advantages of using both resonant and non-resonant lasing behaviours.

Chapter 6: Conclusions and outlook

Even though RLs have unique properties and are more cost-effective to fabricate, their broader application is hindered because of challenges faced in stabilising the lasing modes and controlling the lasing parameters. The chaotic fluctuations and instability of the lasing modes in RLs result in rapid changes of the emission spectra where the intensity and emission wavelengths fluctuate with time. These fluctuations in random lasers make tuning and controlling the lasing parameters difficult. Furthermore, in many cases, light scattered in disordered media does not form a closed loop (i.e. cavities), and the emitted light becomes incoherent similar to that of amplified spontaneous emission observed in light-emitting diodes. These issues have impeded the application of these sources where broadband wavelength-controlled sources or single-mode sources emitting at particular wavelengths are required, limiting the application of RLs in optoelectronic devices.

In this thesis, some of the issues mentioned above are investigated and addressed. In **chapter 3**, highly localised modes have been demonstrated in the InP random NW array, leading to stable multi-mode lasing. We have designed and experimentally demonstrated that Anderson localisation in RLs could be achieved using InP NW arrays due to the NWs' high gain and strong scattering properties. In **chapter 4**, novel methods to control the laser properties of these stable lasers has been demonstrated. Unlike conventional methods such as changing the materials and alloys which is used in III-V semiconductor lasers to change the gain curve and tune the emission wavelengths, here it was shown by changing the design parameters of the NW array, it is possible to change the lasing threshold, the number of lasing modes, the Q, and the wavelength resonances of the modes. In **chapter 5**, both resonant and non-resonant lasing modes in the randomly oriented GaAs-AlGaAs core-shell NWs were demonstrated. In addition, different practical methods for managing the type of mode were also presented. It was shown that by aligning the NW orientation, non-resonant feedback could be suppressed, thereby making the system behaved similarly to lasers with conventional cavities with resonant lasing modes.

While substantial advancements have been made in the development of RLs in various structures and material systems, there is still much more that is required to be done before RLs can be commercially realised. Here, we have mentioned some ideas and suggestions for opening up the application of RLs in next-generation devices.

Electrically driven lasing: In this project, the NWs were optically pumped, but, ultimately, RLs have to be electrically driven to be used practically. To date, there have been several successful demonstrations of electrically-driven NW based RLs in different structures such as Schottky diode [158], p–n junction [159], metal-insulator-semiconductor (MIS) [160, 161], and quantum wells [162]. ZnO with large exciton binding energy was used in all these devices with the emission wavelength in the UV region. However, electrically-driven infrared RL has not been achieved yet. Generally, to achieve electrically driven lasing, there are challenges associated with forming ohmic contacts on the small end facets of the nanowire and with uniformly doping the nanowires with p-type and n-type dopants during the nanowire growth.

Moreover, there is a bigger issue with increased losses due to absorption in the metal contact. To reduce absorption loss, the nanowire cavity with metal contacts has to be appropriately designed, and the metal coverage on the nanowire has to be minimised. Transparent conducting metal oxide can also be investigated as the contact material.

Single-mode lasing: Controlling the number of the lasing modes in RLs is very challenging. In chapter 4, we have shown that decreasing the lateral size of the array could reduce the number of supported modes in RLs. However, as the size gets smaller, the mode leakage increases, leading to lower *Q* and higher thresholds. To solve these issues, using mirrors surrounding the array could substantially decrease the mode's leakage, leading to higher Qs. For example, Heo et al. have shown that using a two-dimensional 2D photonic crystal resonant cavity makes it possible to obtain room-temperature lasing even using short NWs. So, photonic crystals could be incorporated as mirrors in our designed RLs to increase the *Q* of the lasing cavities in small arrays leading to single-mode lasing.

Flexible random lasers: Tunable lasers fabricated on flexible substrates are needed for flexible optoelectronic devices. The cavities of RLs are based on multiple scattering of light offering new functionalities inaccessible with conventional lasers, such as an alterable shape and an easy integration with flexible optoelectronic devices. Different platforms for flexible RLs have been reported. Lau et al. have reported flexible UV RLs using ZnO thin films and nanoparticles on plastic substrates [163]. In another work, Lee et al. have experimentally demonstrated a flexible random laser fabricated on a polyethylene terephthalate (PET) substrate with a high degree of tunability in lasing emissions using Rhodamine 6G and silver nanoprisms. It was shown by bending the device, the lasing wavelengths could be shifted to lower values. Sun et al. showed tunable coherent loops from transferring unique ZnO nanobrushes on top of polydimethylsiloxane (PDMS) elastomer substrate. It was demonstrated by extending the substrate, the density of ZnO nanobrushes can be reduced,

leading to more coherent loops for random lasing and gradually increase of the number of coherent closed loops and lasing modes [131]. In our III-V NW arrays, an epitaxial lift-off (ELO) [164, 165] can be incorporated prior to NW growth. The NWs can then be embedded in a polymer and lifted off from the substrate to make flexible RLs.

3D Anderson localisation: In our project, we have designed random arrays of InP NWs to localise the modes and achieve stable multi-mode lasing. Since the disorder is only in the x-y plane, perpendicular to the NWs, our systems show only 2D Anderson localisation (in the x-y plane). Since we do not have any disorder in the refractive index profile in the z-direction, the confinement of the optical field here is not related to Anderson localisation, but to refractive index, contrast resulted from the carrier generation profile and increase in temperature. Here, even though the mode is localised in three dimensions, 3D Anderson localisation is not achieved in our results. 3D Anderson localisation of light is an exciting subject that can lead to many fundamental and practical applications; however, up to now, it is still elusive. Using high refractive index materials such as InP and applying disorder in 3D could lead to 3D localisation of the light.

In conclusion, RLs have shown great potential for cost-effective, large area and flexible lasers. Although further progress is still required to commercialise RLs, significant achievements have been made in developing RLs in various platforms, material systems and structures. In this dissertation, we have shown state-of-the-art stable multi-mode lasers based on III-V NWs. Different parameters of the random lasers were controlled using various methods and techniques. Our work in RLs can help solve some of the problems in these devices and open up the application of such lasers in future photonic devices.

References

[1] W. M. Steen, K. G. Watkins, and J. Mazumder, *Laser Material Processing*. Springer London, 2010.

[2] W. Demtröder and M. Roach, *Laser Spectroscopy: Basic Concepts and Instrumentation*. Springer Berlin Heidelberg, 2013.

[3] H. Cao, "Lasing in random media," *Waves in random media,* vol. 13, no. 3, pp. R1-R39, 2003.

[4] G. Haider *et al.*, "A Highly-Efficient Single Segment White Random Laser," *ACS Nano,* vol. 12, no. 12, pp. 11847-11859, 2018/12/26 2018.

[5] S.-W. Chang *et al.*, "A White Random Laser," *Scientific Reports,* vol. 8, no. 1, p. 2720, 2018/02/09 2018.

[6] B. Redding, M. A. Choma, and H. Cao, "Speckle-free laser imaging using random laser illumination," *Nature Photonics,* vol. 6, p. 355, 04/29/online 2012.

[7] T. Zhai *et al.*, "A plasmonic random laser tunable through stretching silver nanowires embedded in a flexible substrate," *Nanoscale,* vol. 7, no. 6, pp. 2235-2240, 2015.

[8] M. L. da Silva-Neto *et al.*, "UV random laser emission from flexible ZnO-Ag-enriched electrospun cellulose acetate fiber matrix," *Scientific Reports,* vol. 9, no. 1, p. 11765, 2019/08/13 2019.

[9] H. Cao, "Review on latest developments in random lasers with coherent feedback," *Journal of Physics A: Mathematical and General,* vol. 38, no. 49, p. 10497, 2005.

[10] Q. Song, S. Xiao, Z. Xu, V. M. Shalaev, and Y. L. Kim, "Random laser spectroscopy for nanoscale perturbation sensing," *Optics letters,* vol. 35, no. 15, pp. 2624-2626, 2010.

[11] Q. Song *et al.*, "Detection of nanoscale structural changes in bone using random lasers," *Biomedical optics express,* vol. 1, no. 5, pp. 1401-1407, 2010.

[12] H. Cao, "Random lasers: development, features and applications," *Optics and photonics news,* vol. 16, no. 1, pp. 24-29, 2005.

[13] R. Ambartsumyan, N. Basov, P. Kryukov, and V. Letokhov, "A laser with a nonresonant feedback," *IEEE J. Quantum Electron,* vol. 2, no. 9, pp. 442-446, 1966.

[14] V. Letokhov, "Quantum statistics of multiple-mode emission of an atomic ensemble," *Sov. Phys. JETP,* vol. 26, pp. 1246-1251, 1968.

[15] V. M. Markushev, V. Zolin, and C. M. Briskina, "Luminescence and stimulated emission of neodymium in sodium lanthanum molybdate powders," *Quantum Electronics,* vol. 16, no. 2, pp. 281-283, 1986.

[16] V. M. Markushev, N. É. Ter-Gabriélyan, C. M. Briskina, V. Belan, and V. Zolin, "Stimulated emission kinetics of neodymium powder lasers," *Soviet Journal of Quantum Electronics,* vol. 20, no. 7, p. 773, 1990.

[17] C. Gouedard, D. Husson, C. Sauteret, F. Auzel, and A. Migus, "Generation of spatially incoherent short pulses in laser-pumped neodymium stoichiometric crystals and powders," *JOSA B,* vol. 10, no. 12, pp. 2358-2363, 1993.

[18] C. M. Briskina, V. M. Markushev, and N. Ter-Gabrielyan, "Use of a model of coupled microcavities in the interpretation of experiments on powder lasers," *Quantum Electronics,* vol. 26, no. 10, p. 923, 1996.

[19] A. Y. Zyuzin, "Superfluorescence of photonic paint," *Journal of Experimental and Theoretical Physics,* vol. 86, no. 3, pp. 445-449, 1998.

[20] F. Auzel and P. Goldner, "Coherent light sources with powder: Stimulated amplification versus super-radiance," *Journal of alloys and compounds,* vol. 300, pp. 11-17, 2000.

[21] N. M. Lawandy, "'Paint-On Lasers' Light the Way for New Technologies," *Photonics Spectra,* vol. 28, no. 7, pp. 119-124, 1994.

[22] M. A. Noginov, H. J. Caulfield, N. E. Noginova, and P. Venkateswarlu, "Line narrowing in the dye solution with scattering centers," *Optics Communications,* vol. 118, no. 3, pp. 430-437, 1995/07/15/ 1995.

[23] W. Zhang, N. Cue, and K. M. Yoo, "Effect of random multiple light scattering on the laser action in a binary-dye mixture," *Optics Letters,* vol. 20, no. 9, pp. 1023-1025, 1995/05/01 1995.

[24] G. Zacharakis, G. Heliotis, G. Filippidis, D. Anglos, and T. G. Papazoglou, "Investigation of the laserlike behavior of polymeric scattering gain media under subpicosecond laser excitation," *Applied Optics,* vol. 38, no. 28, pp. 6087-6092, 1999/10/01 1999.

[25] G. van Soest and A. Lagendijk, "$\ensuremath{\beta}$ factor in a random laser," *Physical Review E,* vol. 65, no. 4, p. 047601, 03/18/ 2002.

[26] G. Berger, M. Kempe, and A. Genack, "Dynamics of stimulated emission from random media," *Physical Review E,* vol. 56, no. 5, p. 6118, 1997.

[27] G. van Soest, F. J. Poelwijk, R. Sprik, and A. Lagendijk, "Dynamics of a random laser above threshold," *Physical review letters,* vol. 86, no. 8, p. 1522, 2001.

[28] H. Cao *et al.*, "Ultraviolet lasing in resonators formed by scattering in semiconductor polycrystalline films," *Applied Physics Letters,* vol. 73, no. 25, pp. 3656-3658, 1998.

[29] H. Cao, J. Y. Xu, S. H. Chang, and S. T. Ho, "Transition from amplified spontaneous emission to laser action in strongly scattering media," *Physical Review E,* vol. 61, no. 2, pp. 1985-1989, 02/01/ 2000.

[30] Y. Ling, H. Cao, A. Burin, M. Ratner, X. Liu, and R. Chang, "Investigation of random lasers with resonant feedback," *Physical Review A,* vol. 64, no. 6, p. 063808, 2001.

[31] H. Cao, Y. Ling, J. Y. Xu, and A. L. Burin, "Probing localized states with spectrally resolved speckle techniques," *Physical Review E,* vol. 66, no. 2, p. 025601, 08/23/ 2002.

[32] H. Cao, J. Xu, E. Seelig, and R. Chang, "Microlaser made of disordered media," *Applied Physics Letters,* vol. 76, no. 21, pp. 2997-2999, 2000.

[33] R. C. Polson, A. Chipouline, and Z. V. Vardeny, "Random Lasing in π-Conjugated Films and Infiltrated Opals," *Advanced Materials,* vol. 13, no. 10, pp. 760-764, 2001.

[34] R. Polson and Z. Vardeny, "Organic random lasers in the weak-scattering regime," *Physical Review B,* vol. 71, no. 4, p. 045205, 2005.

[35] A. Tulek, R. Polson, and Z. Vardeny, "Naturally occurring resonators in random lasing of π-conjugated polymer films," *Nature Physics,* vol. 6, no. 4, p. 303, 2010.

[36] F. Mayinger, *Optical Measurements: Techniques and Applications*. Springer Berlin Heidelberg, 2013.

[37] S. Biasco *et al.*, "Frequency-tunable continuous-wave random lasers at terahertz frequencies," *Light: Science & Applications,* vol. 8, no. 1, p. 43, 2019/05/01 2019.

[38] H. R. Gordon, "Light scattering and absorption by randomly-oriented cylinders: dependence on aspect ratio for refractive indices applicable for marine particles," *Optics Express,* vol. 19, no. 5, pp. 4673-4691, 2011/02/28 2011.

[39] G. Mie, "Beiträge zur Optik trüber Medien, speziell kolloidaler Metallösungen," *Annalen der Physik,* https://doi.org/10.1002/andp.19083300302 vol. 330, no. 3, pp. 377-445, 1908/01/01 1908.

[40] V. Letokhov, "Generation of light by a scattering medium with negative resonance absorption," *Sov. Phys. JETP,* vol. 26, pp. 835-840, 1968.

[41] N. M. Lawandy, R. Balachandran, A. Gomes, and E. Sauvain, "Laser action in strongly scattering media," *Nature,* vol. 368, no. 6470, p. 436, 1994.

[42] K. J. Vahala, "Optical microcavities," *Nature,* vol. 424, no. 6950, pp. 839-846, 2003/08/01 2003.

[43] H. Cao, Y. Zhao, S.-T. Ho, E. Seelig, Q. Wang, and R. P. Chang, "Random laser action in semiconductor powder," *Physical Review Letters,* vol. 82, no. 11, p. 2278, 1999.

[44] L. Shi and R. R. Alfano, *Deep imaging in tissue and biomedical materials: using linear and nonlinear optical methods*. Jenny Stanford Publishing, 2017.

[45] A. Yaroshevsky, Z. Glasser, E. e. Granot, and S. Sternklar, "Transition from the ballistic to the diffusive regime in a turbid medium," *Optics Letters,* vol. 36, no. 8, pp. 1395-1397, 2011/04/15 2011.

[46] P. W. Anderson, "Absence of Diffusion in Certain Random Lattices," *Physical Review,* vol. 109, no. 5, pp. 1492-1505, 03/01/ 1958.

[47] H. De Raedt, A. Lagendijk, and P. de Vries, "Transverse Localization of Light," *Physical Review Letters,* vol. 62, no. 1, pp. 47-50, 01/02/ 1989.

[48] T. Schwartz, G. Bartal, S. Fishman, and M. Segev, "Transport and Anderson localization in disordered two-dimensional photonic lattices," *Nature,* 10.1038/nature05623 vol. 446, no. 7131, pp. 52-55, 03/01/print 2007.

[49] J. Andreasen *et al.*, "Modes of random lasers," *Advances in Optics and Photonics,* vol. 3, no. 1, pp. 88-127, 2011/03/31 2011.

[50] P. Lalanne, W. Yan, K. Vynck, C. Sauvan, and J.-P. Hugonin, "Light Interaction with Photonic and Plasmonic Resonances," *Laser & Photonics Reviews,* https://doi.org/10.1002/lpor.201700113 vol. 12, no. 5, p. 1700113, 2018/05/01 2018.

[51] B. E. A. Saleh and M. C. Teich, *Fundamentals of Photonics*. Wiley, 2007.

[52] L. A. Coldren, S. W. Corzine, and M. L. Mashanovitch, *Diode Lasers and Photonic Integrated Circuits*. Wiley, 2012.

[53] P. T. Kristensen and S. Hughes, "Modes and Mode Volumes of Leaky Optical Cavities and Plasmonic Nanoresonators," *ACS Photonics,* vol. 1, no. 1, pp. 2-10, 2014/01/15 2014.

[54] P. T. Kristensen, C. Van Vlack, and S. Hughes, "Generalized effective mode volume for leaky optical cavities," *Optics Letters,* vol. 37, no. 10, pp. 1649-1651, 2012/05/15 2012.

[55] K. Srinivasan, P. E. Barclay, M. Borselli, and O. Painter, "Optical-fiber-based measurement of an ultrasmall volume high-Q photonic crystal microcavity," *Physical Review B,* vol. 70, no. 8, p. 081306, 08/25/ 2004.

[56] S. L. Chuang, *Physics of Photonic Devices*. Wiley, 2009.

[57] S. M. Sze and K. K. Ng, *Physics of Semiconductor Devices*. Wiley, 2006.

[58] X. Aymerich-Humet, F. Serra-Mestres, and J. Millán, "An analytical approximation for the Fermi-Dirac integral F32(η)," *Solid-State Electronics,* vol. 24, no. 10, pp. 981-982, 1981/10/01/ 1981.

[59] W. W. Chow and S. W. Koch, *Semiconductor-Laser Fundamentals: Physics of the Gain Materials*. Springer Berlin Heidelberg, 2013.

[60] P. Sebbah and C. Vanneste, "Random laser in the localized regime," *Physical Review B,* vol. 66, no. 14, p. 144202, 10/23/ 2002.

[61] D. M. Sullivan, *Electromagnetic Simulation Using the FDTD Method*. Wiley, 2013.

[62] A. Taflove and S. C. Hagness, *Computational Electrodynamics: The Finite-difference Time-domain Method*. Artech House, 2005.

[63] Y. Kane, "Numerical solution of initial boundary value problems involving maxwell's equations in isotropic media," *IEEE Transactions on Antennas and Propagation,* vol. 14, no. 3, pp. 302-307, 1966.

[64] D. G. Swanson and W. J. R. Hoefer, *Microwave Circuit Modeling Using Electromagnetic Field Simulation*. Artech House, 2003.

[65] Ž. Gačević, D. Gómez Sánchez, and E. Calleja, "Formation Mechanisms of GaN Nanowires Grown by Selective Area Growth Homoepitaxy," *Nano Letters,* vol. 15, no. 2, pp. 1117-1121, 2015/02/11 2015.

[66] X.-Y. Bao *et al.*, "Heteroepitaxial Growth of Vertical GaAs Nanowires on Si (111) Substrates by Metal−Organic Chemical Vapor Deposition," *Nano Letters,* vol. 8, no. 11, pp. 3755-3760, 2008/11/12 2008.

[67] L. Chen, W. Lu, and C. M. Lieber, "Chapter 1 Semiconductor Nanowire Growth and Integration," in *Semiconductor Nanowires: From Next-Generation Electronics to Sustainable Energy*: The Royal Society of Chemistry, 2015, pp. 1-53.

[68] A. A. Koryakin, S. A. Kukushkin, and N. V. Sibirev, "On the Mechanism of the Vapor–Solid–Solid Growth of Au-Catalyzed GaAs Nanowires," *Semiconductors,* vol. 53, no. 3, pp. 350-360, 2019/03/01 2019.

[69] N. Wang *et al.*, "Shape Engineering of InP Nanostructures by Selective Area Epitaxy," *ACS Nano,* vol. 13, no. 6, pp. 7261-7269, 2019/06/25 2019.

[70] R. Q. Zhang, Y. Lifshitz, and S. T. Lee, "Oxide-Assisted Growth of Semiconducting Nanowires," *Advanced Materials,* https://doi.org/10.1002/adma.200301641 vol. 15, no. 7-8, pp. 635-640, 2003/04/17 2003.

[71] B. Mandl *et al.*, "Growth Mechanism of Self-Catalyzed Group III−V Nanowires," *Nano Letters,* vol. 10, no. 11, pp. 4443-4449, 2010/11/10 2010.

[72] L. Dupré, D. Buttard, C. Leclere, H. Renevier, and P. Gentile, "Gold Contamination in VLS-Grown Si Nanowires: Multiwavelength Anomalous Diffraction Investigations," *Chemistry of Materials,* vol. 24, no. 23, pp. 4511-4516, 2012/12/11 2012.

[73] K. Nagashima, T. Yanagida, K. Oka, H. Tanaka, and T. Kawai, "Mechanism and control of sidewall growth and catalyst diffusion on oxide nanowire vapor-liquid-solid growth," *Applied Physics Letters,* vol. 93, no. 15, p. 153103, 2008/10/13 2008.

[74] G. Priante, G. Patriarche, F. Oehler, F. Glas, and J.-C. Harmand, "Abrupt GaP/GaAs Interfaces in Self-Catalyzed Nanowires," *Nano Letters,* vol. 15, no. 9, pp. 6036-6041, 2015/09/09 2015.

[75] A. Martina, S. Tom, V. Paul, P. A. M. B. Erik, and L. M. Otto, "Ultrafast active control of optical transmission pseudomodes in a multiple scattering nanowire layer," in *Proc.SPIE*, 2011, vol. 8095.

[76] B. J. Inkson, "2 - Scanning electron microscopy (SEM) and transmission electron microscopy (TEM) for materials characterization," in *Materials Characterization Using Nondestructive Evaluation (NDE) Methods*, G. Hübschen, I. Altpeter, R. Tschuncky, and H.-G. Herrmann, Eds.: Woodhead Publishing, 2016, pp. 17-43.

[77] L. E. Franken, K. Grünewald, E. J. Boekema, and M. C. A. Stuart, "A Technical Introduction to Transmission Electron Microscopy for Soft-Matter: Imaging, Possibilities, Choices, and Technical Developments," *Small,* https://doi.org/10.1002/smll.201906198 vol. 16, no. 14, p. 1906198, 2020/04/01 2020.

[78] D. K. Schroder, *Semiconductor Material and Device Characterization*. Wiley, 2015.

[79] "Semiconductor Characterization Techniques," in *Fundamentals of Solid State Engineering*, M. Razeghi, Ed. Boston, MA: Springer US, 2006, pp. 521-549.

[80] G. P. Agrawal and N. K. Dutta, "Recombination Mechanisms in Semiconductors," in *Semiconductor Lasers*, G. P. Agrawal and N. K. Dutta, Eds. Boston, MA: Springer US, 1993, pp. 74-146.

[81] M. A. Reshchikov, "Temperature dependence of defect-related photoluminescence in III-V and II-VI semiconductors," *Journal of Applied Physics,* vol. 115, no. 1, p. 012010, 2014/01/07 2014.

[82] S. Arab, M. Yao, C. Zhou, P. Daniel Dapkus, and S. B. Cronin, "Doping concentration dependence of the photoluminescence spectra of n-type GaAs nanowires," *Applied Physics Letters,* vol. 108, no. 18, p. 182106, 2016/05/02 2016.

[83] H. A. Atwater and A. Polman, "Plasmonics for improved photovoltaic devices," *Nature Materials,* Review Article vol. 9, p. 205, 02/19/online 2010.

[84] B. P. Rand, P. Peumans, and S. R. Forrest, "Long-range absorption enhancement in organic tandem thin-film solar cells containing silver nanoclusters," *Journal of Applied Physics,* vol. 96, no. 12, pp. 7519-7526, 2004.

[85] H. Raether, *Surface Plasmons on Smooth and Rough Surfaces and on Gratings*. Springer Berlin Heidelberg, 2006.

[86] H. Hu, A. Strybulevych, J. Page, S. E. Skipetrov, and B. A. van Tiggelen, "Localization of ultrasound in a three-dimensional elastic network," *Nature Physics,* vol. 4, no. 12, p. 945, 2008.

[87] F. Jendrzejewski *et al.*, "Three-dimensional localization of ultracold atoms in an optical disordered potential," *Nature Physics,* vol. 8, no. 5, p. 398, 2012.

[88] M. Segev, Y. Silberberg, and D. N. Christodoulides, "Anderson localization of light," *Nat Photon,* 10.1038/nphoton.2013.30 vol. 7, no. 3, pp. 197-204, 03//print 2013.

[89] S. Karbasi, C. R. Mirr, P. G. Yarandi, R. J. Frazier, K. W. Koch, and A. Mafi, "Observation of transverse Anderson localization in an optical fiber," *Optics Letters,* vol. 37, no. 12, pp. 2304-2306, 2012/06/15 2012.

[90] S. Karbasi, C. R. Mirr, R. J. Frazier, P. G. Yarandi, K. W. Koch, and A. Mafi, "Detailed investigation of the impact of the fiber design parameters on the transverse Anderson localization of light in disordered optical fibers," *Optics Express,* vol. 20, no. 17, pp. 18692-18706, 2012/08/13 2012.

[91] H. Sheinfux Hanan, Y. Lumer, G. Ankonina, Z. Genack Azriel, G. Bartal, and M. Segev, "Observation of Anderson localization in disordered nanophotonic structures," *Science,* vol. 356, no. 6341, pp. 953-956, 2017/06/02 2017.

[92] M. Aeschlimann *et al.*, "Perfect absorption in nanotextured thin films via Anderson-localized photon modes," *Nature Photonics,* vol. 9, no. 10, pp. 663-668, 2015/10/01 2015.

[93] R. Sapienza, "Determining random lasing action," *Nature Reviews Physics,* vol. 1, no. 11, pp. 690-695, 2019/11/01 2019.

[94] K. L. van der Molen, A. P. Mosk, and A. Lagendijk, "Quantitative analysis of several random lasers," *Optics Communications,* vol. 278, no. 1, pp. 110-113, 2007/10/01/ 2007.

[95] S. Mujumdar, M. Ricci, R. Torre, and D. S. Wiersma, "Amplified Extended Modes in Random Lasers," *Physical Review Letters,* vol. 93, no. 5, p. 053903, 07/30/ 2004.

[96] Y. Ling, H. Cao, A. L. Burin, M. A. Ratner, X. Liu, and R. P. H. Chang, "Investigation of random lasers with resonant feedback," *Physical Review A,* vol. 64, no. 6, p. 063808, 11/14/ 2001.

[97] H. E. Türeci, L. Ge, S. Rotter, and A. D. Stone, "Strong Interactions in Multimode Random Lasers," *Science,* vol. 320, no. 5876, p. 643, 2008.

[98] H. Cao, Y. G. Zhao, S. T. Ho, E. W. Seelig, Q. H. Wang, and R. P. H. Chang, "Random Laser Action in Semiconductor Powder," *Physical Review Letters,* vol. 82, no. 11, pp. 2278-2281, 03/15/ 1999.

[99] C. H. Liu *et al.*, "High-Density, Ordered Ultraviolet Light-Emitting ZnO Nanowire Arrays," *Advanced Materials,* https://doi.org/10.1002/adma.200304430 vol. 15, no. 10, pp. 838-841, 2003/05/16 2003.

[100] K. H. Li, X. Liu, Q. Wang, S. Zhao, and Z. Mi, "Ultralow-threshold electrically injected AlGaN nanowire ultraviolet lasers on Si operating at low temperature," *Nature Nanotechnology,* vol. 10, no. 2, pp. 140-144, 2015/02/01 2015.

[101] H. Y. Yang, S. F. Yu, S. P. Lau, S. H. Tsang, G. Z. Xing, and T. Wu, "Ultraviolet coherent random lasing in randomly assembled SnO2 nanowires," *Applied Physics Letters,* vol. 94, no. 24, p. 241121, 2009/06/15 2009.

[102] M. Sakai *et al.*, "Random laser action in GaN nanocolumns," *Applied Physics Letters,* vol. 97, no. 15, p. 151109, 2010.

[103] J. Bingi, A. R. Warrier, and C. Vijayan, "Raman mode random lasing in ZnS-β-carotene random gain media," *Applied Physics Letters* vol. 102, no. 22, p. 221105, 2013.

[104] B. Fazio *et al.*, "Strongly enhanced light trapping in a two-dimensional silicon nanowire random fractal array," *Light: Science & Applications,* vol. 5, no. 4, pp. e16062-e16062, 2016/04/01 2016.

[105] M. Sakai *et al.*, "Random laser action in GaN nanocolumns," vol. 97, no. 15, p. 151109, 2010.

[106] M. D. Kelzenberg *et al.*, "Enhanced absorption and carrier collection in Si wire arrays for photovoltaic applications," *Nature Materials,* vol. 9, no. 3, pp. 239-244, 2010/03/01 2010.

[107] H. J. Joyce *et al.*, "Ultralow Surface Recombination Velocity in InP Nanowires Probed by Terahertz Spectroscopy," *Nano Letters,* vol. 12, no. 10, pp. 5325-5330, 2012/10/10 2012.

[108] H. J. Joyce *et al.*, "Electronic properties of GaAs, InAs and InP nanowires studied by terahertz spectroscopy," *Nanotechnology,* vol. 24, no. 21, p. 214006, 2013/04/25 2013.

[109] O. Madelung, *Semiconductors: Group IV Elements and III-V Compounds*. Springer-Verlag, 1991.

[110] A. Mishra *et al.*, "Polarization and temperature dependence of photoluminescence from zincblende and wurtzite InP nanowires," *Applied Physics Letters,* vol. 91, no. 26, p. 263104, 2007.

[111] D. E. Aspnes and A. A. Studna, "Dielectric functions and optical parameters of Si, Ge, GaP, GaAs, GaSb, InP, InAs, and InSb from 1.5 to 6.0 eV," *Physical Review B,* vol. 27, no. 2, pp. 985-1009, 01/15/ 1983.

[112] K. A. Meradi, F. Tayeboun, S. Ghezali, R. Naoum, and H. T. Hattori, "Design of a thermal tunable photonic-crystal coupler," *Journal of Russian Laser Research,* vol. 32, no. 6, pp. 572-578, 2011/11/01 2011.

[113] B. R. Bennett, R. A. Soref, and J. A. D. Alamo, "Carrier-induced change in refractive index of InP, GaAs and InGaAsP," *IEEE Journal of Quantum Electronics,* vol. 26, no. 1, pp. 113-122, 1990.

[114] Q. Gao *et al.*, "Selective-Area Epitaxy of Pure Wurtzite InP Nanowires: High Quantum Efficiency and Room-Temperature Lasing," *Nano Letters,* vol. 14, no. 9, pp. 5206-5211, 2014/09/10 2014.

[115] D. Saxena *et al.*, "Optically pumped room-temperature GaAs nanowire lasers," *Nature Photonics,* vol. 7, p. 963, 11/17/online 2013.

[116] S. W. Eaton *et al.*, "Lasing in robust cesium lead halide perovskite nanowires," *Proceedings of the National Academy of Sciences,* vol. 113, no. 8, pp. 1993-1998, 2016.

[117] M. A. Zimmler, J. Bao, F. Capasso, S. Müller, and C. Ronning, "Laser action in nanowires: Observation of the transition from amplified spontaneous emission to laser oscillation," *Applied Physics Letters,* vol. 93, no. 5, p. 051101, 2008/08/04 2008.

[118] P. Stano and P. Jacquod, "Suppression of interactions in multimode random lasers in the Anderson localized regime," *Nature Photonics,* vol. 7, no. 1, pp. 66-71, 2013/01/01 2013.

[119] S. Mujumdar, V. Türck, R. Torre, and D. S. Wiersma, "Chaotic behavior of a random laser with static disorder," *Physical Review A,* vol. 76, no. 3, p. 033807, 09/07/ 2007.

[120] Z. Pengchao, Z. G. Feng, Q. Fan, Q. Aiyi, W. Yufei, and W. H. Zheng, "Blue shift of laser mode in photonic crystal microcavity," in *Proc.SPIE*, 2014, vol. 9267.

[121] C. Tessarek, R. Goldhahn, G. Sarau, M. Heilmann, and S. Christiansen, "Carrier-induced refractive index change observed by a whispering gallery mode shift in GaN microrods," *New Journal of Physics,* vol. 17, no. 8, p. 083047, 2015/08/25 2015.

[122] D. Saxena, F. Wang, Q. Gao, S. Mokkapati, H. H. Tan, and C. Jagadish, "Mode Profiling of Semiconductor Nanowire Lasers," *Nano Letters,* vol. 15, no. 8, pp. 5342-5348, 2015/08/12 2015.

[123] M. A. Zimmler, F. Capasso, S. Müller, and C. Ronning, "Optically pumped nanowire lasers: invited review," *Semiconductor Science and Technology,* vol. 25, no. 2, p. 024001, 2010/01/22 2010.

[124] J. Ziegler, C. Wörister, C. Vidal, C. Hrelescu, and T. A. Klar, "Plasmonic Nanostars as Efficient Broadband Scatterers for Random Lasing," *ACS Photonics,* vol. 3, no. 6, pp. 919-923, 2016/06/15 2016.

[125] Z. Wang *et al.*, "Single-excitation dual-color coherent lasing by tuning resonance energy transfer processes in porous structured nanowires," *Nanoscale,* 10.1039/C5NR03349G vol. 7, no. 37, pp. 15091-15098, 2015.

[126] N. Bachelard, S. Gigan, X. Noblin, and P. Sebbah, "Adaptive pumping for spectral control of random lasers," *Nature Physics,* vol. 10, no. 6, pp. 426-431, 2014/06/01 2014.

[127] M. Leonetti, C. Conti, and C. Lopez, "The mode-locking transition of random lasers," *Nature Photonics,* vol. 5, no. 10, p. 615, 2011.

[128] D. S. Wiersma and S. Cavalieri, "A temperature-tunable random laser," *Nature,* vol. 414, no. 6865, pp. 708-709, 2001/12/01 2001.

[129] S. Qinghai *et al.*, "Liquid crystals based tunable high-Q directional random laser from a planar random microcavity," in *2007 Quantum Electronics and Laser Science Conference*, 2007, pp. 1-2.

[130] Q. Song, L. Liu, L. Xu, Y. Wu, and Z. Wang, "Electrical tunable random laser emission from a liquid-crystal infiltrated disordered planar microcavity," *Optics Letters,* vol. 34, no. 3, pp. 298-300, 2009/02/01 2009.

[131] T.-M. Sun *et al.*, "Stretchable Random Lasers with Tunable Coherent Loops," *ACS Nano,* vol. 9, no. 12, pp. 12436-12441, 2015/12/22 2015.

[132] T. Naruta, T. Akita, Y. Uchida, D. Lisjak, A. Mertelj, and N. Nishiyama, "Magnetically controllable random laser in ferromagnetic nematic liquid crystals," *Optics Express,* vol. 27, no. 17, pp. 24426-24433, 2019/08/19 2019.

[133] S. Gottardo, R. Sapienza, P. D. García, A. Blanco, D. S. Wiersma, and C. López, "Resonance-driven random lasing," *Nature Photonics,* vol. 2, no. 7, pp. 429-432, 2008/07/01 2008.

[134] M. Rashidi, T. Haggren, Z. Su, C. Jagadish, S. Mokkapati, and H. H. Tan, "Managing Resonant and Nonresonant Lasing Modes in GaAs Nanowire Random Lasers," *Nano Letters,* vol. 21, no. 9, pp. 3901-3907, 2021/05/12 2021.

[135] M. Rashidi, H. H. Tan, and S. Mokkapati, "Stable, multi-mode lasing in the strong localization regime from InP random nanowire arrays at low temperature," *Optica,* vol. 8, no. 9, pp. 1160-1166, 2021/09/20 2021.

[136] V. Myroshnychenko *et al.*, "Modelling the optical response of gold nanoparticles," *Chemical Society Reviews,* 10.1039/B711486A vol. 37, no. 9, pp. 1792-1805, 2008.

[137] Q. Li *et al.*, "Single-mode GaN nanowire lasers," *Optics Express,* vol. 20, no. 16, pp. 17873-17879, 2012/07/30 2012.

[138] Y. Ma, X. Guo, X. Wu, L. Dai, and L. Tong, "Semiconductor nanowire lasers," *Advances in Optics and Photonics,* vol. 5, no. 3, pp. 216-273, 2013/09/30 2013.

[139] M. Kuwata-Gonokami and K. Takeda, "Polymer whispering gallery mode lasers," *Optical Materials,* vol. 9, no. 1, pp. 12-17, 1998/01/01/ 1998.

[140] G. Zhu *et al.*, "Whispering-Gallery Mode Lasing in a Floating GaN Microdisk with a Vertical Slit," *Scientific Reports,* vol. 10, no. 1, p. 253, 2020/01/14 2020.

[141] F. Vollmer and D. Yu, *Optical Whispering Gallery Modes for Biosensing: From Physical Principles to Applications*. Springer International Publishing, 2020.

[142] D. Saxena *et al.*, "Optically pumped room-temperature GaAs nanowire lasers," *Nature Photonics,* vol. 7, no. 12, pp. 963-968, 2013/12/01 2013.

[143] V. V. Ursaki, A. Burlacu, E. V. Rusu, V. Postolake, and I. M. Tiginyanu, "Whispering gallery modes and random lasing in ZnO microstructures," *Journal of Optics A: Pure and Applied Optics,* vol. 11, no. 7, p. 075001, 2009/04/15 2009.

[144] H. Gao, A. Fu, S. C. Andrews, and P. Yang, "Cleaved-coupled nanowire lasers," *Proceedings of the National Academy of Sciences,* vol. 110, no. 3, p. 865, 2013.

[145] L. Ye *et al.*, "Thermally tunable random laser in dye-doped liquid crystals," *Journal of Modern Optics,* vol. 60, no. 19, pp. 1607-1611, 2013/11/01 2013.

[146] A. Boschetti *et al.*, "Spectral super-resolution spectroscopy using a random laser," *Nature Photonics,* vol. 14, no. 3, pp. 177-182, 2020/03/01 2020.

[147] S.-W. Chang *et al.*, "A white random laser," vol. 8, no. 1, p. 2720, 2018.

[148] G. Haider *et al.*, "A highly-efficient single segment white random laser," vol. 12, no. 12, pp. 11847-11859, 2018.

[149] M. Petit *et al.*, "Passivation of InP(100) substrates: first stages of nitridation by thin InN surface overlayers studied by electron spectroscopies," *Surface and Interface Analysis,* https://doi.org/10.1002/sia.2045 vol. 37, no. 7, pp. 615-620, 2005/07/01 2005.

[150] W. L. Sha, C. H. Liu, and R. R. Alfano, "Spectral and temporal measurements of laser action of Rhodamine 640 dye in strongly scattering media," *Optics Letters,* vol. 19, no. 23, pp. 1922-1924, 1994/12/01 1994.

[151] J. Azkargorta, M. Bettinelli, I. Iparraguirre, S. Garcia-Revilla, R. Balda, and J. Fernández, "Random lasing in Nd:LuVO4 crystal powder," *Optics Express,* vol. 19, no. 20, pp. 19591-19599, 2011/09/26 2011.

[152] B. Fazio *et al.*, "Strongly enhanced light trapping in a two-dimensional silicon nanowire random fractal array," *Light: Science & Applications,* vol. 5, no. 4, p. e16062, 2016.

[153] M. D. Kelzenberg *et al.*, "Enhanced absorption and carrier collection in Si wire arrays for photovoltaic applications," *Nature Materials,* vol. 9, p. 239, 02/14/online 2010.

[154] R. Niyuki *et al.*, "Double threshold behavior in a resonance-controlled ZnO random laser," *APL Photonics,* vol. 2, no. 3, p. 036101, 2017/03/01 2017.

[155] O. Demichel, M. Heiss, J. Bleuse, H. Mariette, and A. Fontcuberta i Morral, "Impact of surfaces on the optical properties of GaAs nanowires," *Applied Physics Letters,* vol. 97, no. 20, p. 201907, 2010/11/15 2010.

[156] G. Jiao, C. Hu, J. Liu, and Y. Qian, "Comparative study of AlxGa1−xAs/GaAs photocathodes with different aluminum concentrations by surface photovoltage spectroscopy," *Applied Optics,* vol. 54, no. 28, pp. 8473-8478, 2015/10/01 2015.

[157] Y.-H. Ra and C.-R. Lee, "Ultracompact display pixels: Tunnel junction nanowire photonic crystal laser," *Nano Energy,* vol. 84, p. 105870, 2021/06/01/ 2021.

[158] F. Gao, M. M. Morshed, S. B. Bashar, Y. Zheng, Y. Shi, and J. Liu, "Electrically pumped random lasing based on an Au–ZnO nanowire Schottky junction," *Nanoscale,* vol. 7, no. 21, pp. 9505-9509, 2015.

[159] J. Huang *et al.*, "ZnO p–n Homojunction Random Laser Diode Based on Nitrogen-Doped p-type Nanowires," *Advanced Optical Materials,* https://doi.org/10.1002/adom.201200062 vol. 1, no. 2, pp. 179-185, 2013/02/01 2013.

[160] X. Ma *et al.*, "Room temperature electrically pumped ultraviolet random lasing from ZnO nanorod arrays on Si," *Optics express,* vol. 17, no. 16, pp. 14426-14433, 2009.

[161] X.-Y. Liu, C.-X. Shan, S.-P. Wang, Z.-Z. Zhang, and D.-Z. Shen, "Electrically pumped random lasers fabricated from ZnO nanowire arrays," *Nanoscale,* vol. 4, no. 9, pp. 2843-2846, 2012.

[162] Y. R. Ryu *et al.*, "Excitonic ultraviolet lasing in ZnO-based light emitting devices," *Applied Physics Letters,* vol. 90, no. 13, p. 131115, 2007/03/26 2007.

[163] S. P. Lau *et al.*, "Flexible Ultraviolet Random Lasers Based on Nanoparticles," *Small,* https://doi.org/10.1002/smll.200500098 vol. 1, no. 10, pp. 956-959, 2005/10/01 2005.

[164] K. Mahenderkar Naveen *et al.*, "Epitaxial lift-off of electrodeposited single-crystal gold foils for flexible electronics," *Science,* vol. 355, no. 6330, pp. 1203-1206, 2017/03/17 2017.

[165] J. Dong *et al.*, "Centimeter-long III-Nitride nanowires and continuous-wave pumped lasing enabled by graphically epitaxial lift-off," *Nano Energy,* vol. 78, p. 105404, 2020/12/01/ 2020.